

Aus dem Institut für Molekular- und Zellbiologie
der Hochschule Mannheim
Direktor: Prof. Dr. rer. nat. Mathias Hafner

Stem cell-induced regeneration of skeletal muscle tissue: characterization
of a glycerol-induced muscle damage model

Inauguraldissertation
zur Erlangung des akademischen Grades
Doctor scientiarum humanarum (Dr. sc. hum.)
der
Medizinischen Fakultät Mannheim
der Ruprecht-Karls-Universität
zu
Heidelberg

vorgelegt von
Matteo Rigon

aus
Padova, Italy
2020

Dekan: Prof. Dr med. Sergij Goerd
Referent: Prof. Dr. rer. nat. Rüdiger Rudolf

Table of Contents

| | |
|---|-----|
| 1. Introduction | 1 |
| 1.1 Satellite stem cells and skeletal muscle development | 1 |
| 1.2 Skeletal muscle regeneration | 3 |
| 1.3 Skeletal muscle damage models | 9 |
| 1.4 The neuromuscular junction structure and function | 11 |
| 1.5 Neuromuscular junction development | 14 |
| 1.6 Neuromuscular junction damage models | 16 |
| 1.7 Tissue clearing methods | 18 |
| 1.8 Adipose-derived mesenchymal stem cells (ASCs) and their therapeutic applications 22 | |
| 2. Aims of the study | 24 |
| 3. Animals, materials and methods | 26 |
| 3.1 Animal experiments..... | 26 |
| 3.2 Adipose-derived mesenchymal stem cells (ASCs)..... | 28 |
| 3.3 Immunofluorescence analysis..... | 29 |
| 3.4 Tissue clearing and whole mount immunofluorescence..... | 31 |
| 3.5 Image analysis and semi-automated quantification..... | 32 |
| 3.6 Statistical analysis and figures..... | 33 |
| 4. Results | 34 |
| 4.1 Glycerol injection leads to early necrosis and robust regeneration | 34 |
| 4.2 Glycerol injection leads to transient loss of presynapses | 40 |
| 4.3 Glycerol-induced muscle degeneration and recovery are altered by adipose-derived stem cells (ASCs)..... | 43 |
| 4.4 Adipose-derived mesenchymal stem cells (ASCs) treatment reduces the loss of presynapses in the glycerol damage model | 47 |
| 4.5 Tissue clearing for postsynapse structure and embryonic myosin heavy chain (eMHC) expression | 51 |
| 5. Discussion | 55 |
| 5.1 Low glycerol dose leads successfully to muscle damage and subsequent recovery . | 55 |
| 5.2 Presynapses and postsynapses show a different sensitivity and recovery rate after glycerol-induced muscle damage | 56 |
| 5.3 Adipose-derived mesenchymal stem cell systemic application as beneficial, although transient, effect on skeletal muscle and NMJ recovery | 57 |
| 5.4 MYOCLEAR tissue clearing protocol proved to be promising for the three- dimensional investigation of neuromuscular junction structure and regeneration of glycerol- treated muscles. | 59 |
| 6. Summary | 63 |
| 7. References | 64 |
| 8. Appendix | 75 |
| List of the figures | 75 |
| List of publications..... | 81 |
| Acknowledgements | 106 |
| 9. Curriculum vitae | 107 |
| Abbreviations | 111 |

1. Introduction

1.1 Satellite stem cells and skeletal muscle development

Skeletal muscle is a complex and heterogeneous tissue serving several functions in the organism, including locomotion and thermoregulation. Its maintenance is critical to provide a good quality of life in healthy individuals. Skeletal muscle regeneration after an injury is provided mainly by a specific stem cell population residing underneath the basal lamina, the satellite stem cells. The term “satellite” refers to their location adjacent to the muscle fiber (Mauro 1961), as shown in Figure 1. Upon sensing damage, those cells exit from their quiescent state and start to proliferate and subsequently migrate in the injury site. In this stage, their differentiation towards a myogenic cell type will start. Once they reach the area of the muscle that was damaged, they will align and further differentiate in order to form new functional myofibers (Mauro 1961; Morgan and Partridge 2003; Tedesco, F. S., Dellavalle, A., Diaz-Manera, J., Messina, G., & Cossu 2010; Dumont et al. 2015). Satellite cell activation, proliferation and differentiation are summarized and schematized in Figure 1. The production of new muscle fibers after an insult recapitulates for the most part the process regulating skeletal muscle formation during embryogenesis, termed as myogenesis.

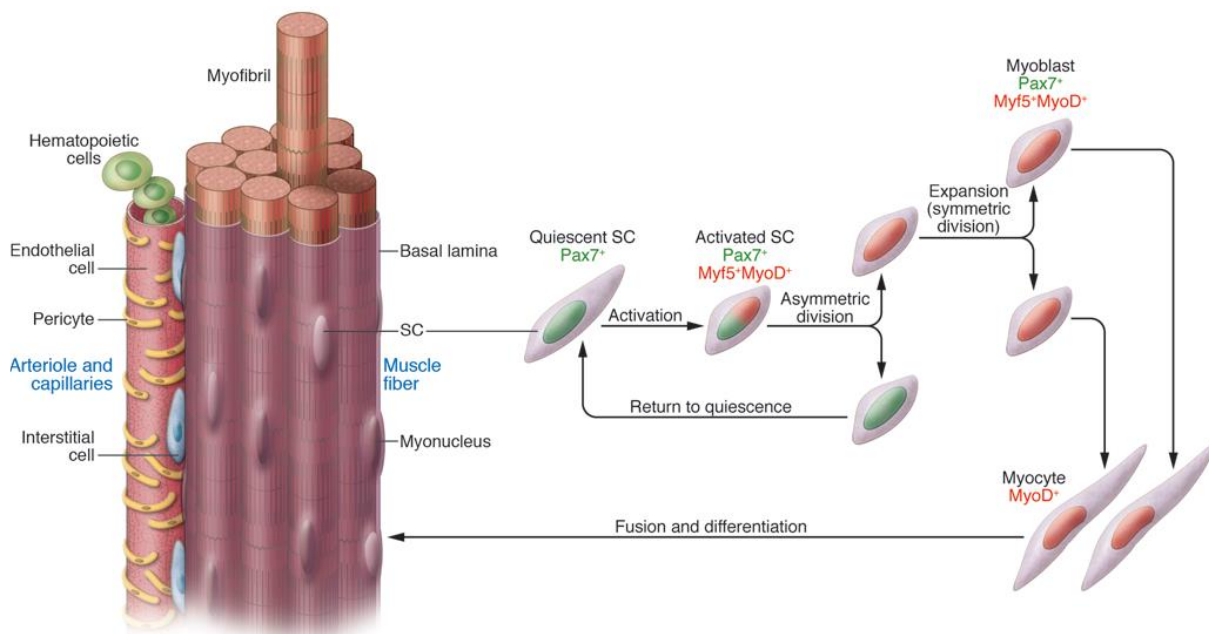


Figure 1- Satellite cells activation upon injury. Satellite cells are subjected to asymmetric cell division, differentiation towards myocytes and subsequent fusion and further differentiation. They are responsible to muscle fiber turnover and recovery. At different stages different transcription factors regulate the differentiation towards new mature myofibers (from Tedesco et al., 2010). For a more detailed description of the transcription factors involved in myogenic differentiation, refer to Figure 2.

As depicted in Figure 2, myogenesis is a complex process, requiring the tightly regulated expression of many genes to coordinate the different developmental phases that will guarantee the correct formation of the tissue (Chargé and Rudnicki 2004; Bentzinger, Wang, and

Rudnicki 2012). Among these genes, the most important are *Pax3* and *Pax7*, paired box transcription factors that exert their function at a myogenic precursor level, and the myogenic regulatory factors (MRFs) *MyoD*, *Myf5*, *myogenin* (*MyoG*), and *Mrf4* (sometimes referred to as *Myf6*). *Pax3/7* are early lineage specification regulators, *Myf5* and *MyoD* commit cells to the myogenic program and *myogenin* and *Mrf4* are marker for terminal differentiation and required for myocytes fusion into myotubes (Tajbakhsh 2009; Bentzinger, Wang, and Rudnicki 2012). In mice, myogenesis takes place from embryonic stage 8.5/9 (E8.5/9) to E 18.5 (Tajbakhsh 2009). At E8.5/9 paraxial mesoderm is segmented in somites from which the dermomyotome will originate (Aulehla and Pourquié 2010). Dermomyotome cells express *Pax3* and *Pax7*, as well as low levels of *Myf5*. As the organism develops, those cells (identified as muscle progenitors) from dermomyotome ventrolateral and dorsomedial sections give rise to the myotome, a primitive muscle structure containing cells expressing high levels of *MyoD* and *Myf5* (Kiefer and Hauschka 2001). Muscle of the limbs originate from migrating cells of the hypaxial domain of the dermomyotome and the myotome. After they reach the limb buds those cells become myoblasts, then myocytes and after fusion will form multi-nucleated myotubes (Bentzinger, Wang, and Rudnicki 2012). In this phase, the functional but still immature muscle cells express a fetal form of myosin heavy chain, referred to as embryonic myosin heavy chain (eMHC) or myosin 3 (MYO3). A part of uncommitted skeletal muscle stem cells that took part in tissue development does not progress along with the rest, entering in a quiescent state and forming the satellite stem cell niche. Those cells maintain the expression of *Pax7* (Buckingham et al. 2003; Tajbakhsh 2009; Bentzinger, Wang, and Rudnicki 2012).

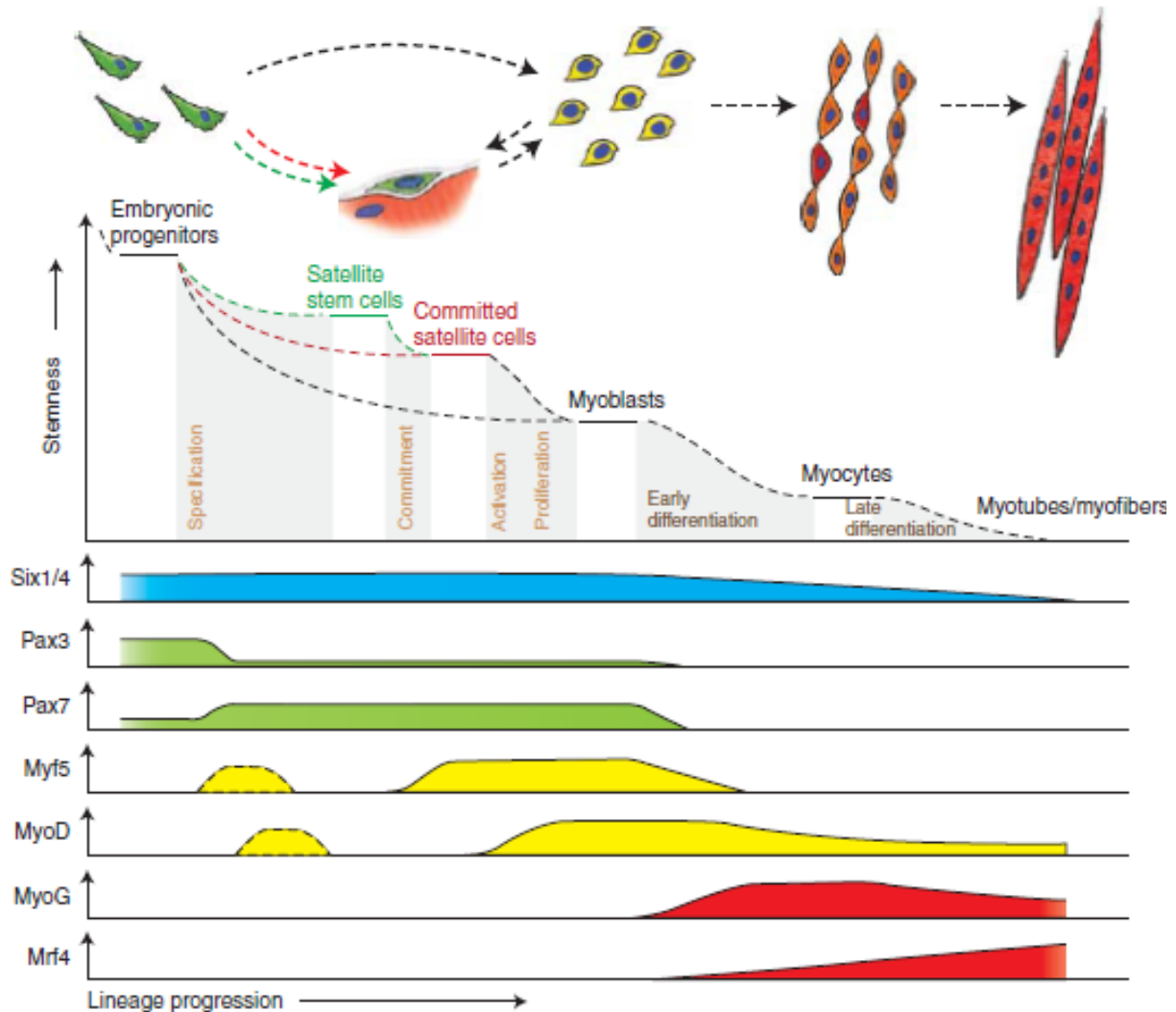


Figure 2- Transcription factor hierarchy in myogenesis. A strict regulation of the expression of specific transcription factors guarantees the successful formation of myofibers. This process is partially recapitulated during muscle regeneration. Figure from Bentzinger, 2012 (Bentzinger, Wang, and Rudnicki 2012).

1.2 Skeletal muscle regeneration

The same transcription factors whose expression is observed during myogenesis are present also during muscle recovery (Tedesco, F. S., Dellavalle, A., Diaz-Manera, J., Messina, G., & Cossu 2010). Moreover, muscle stem cells in adult muscles retain their migratory capability and the ability to sense the environment (Webster et al. 2015).

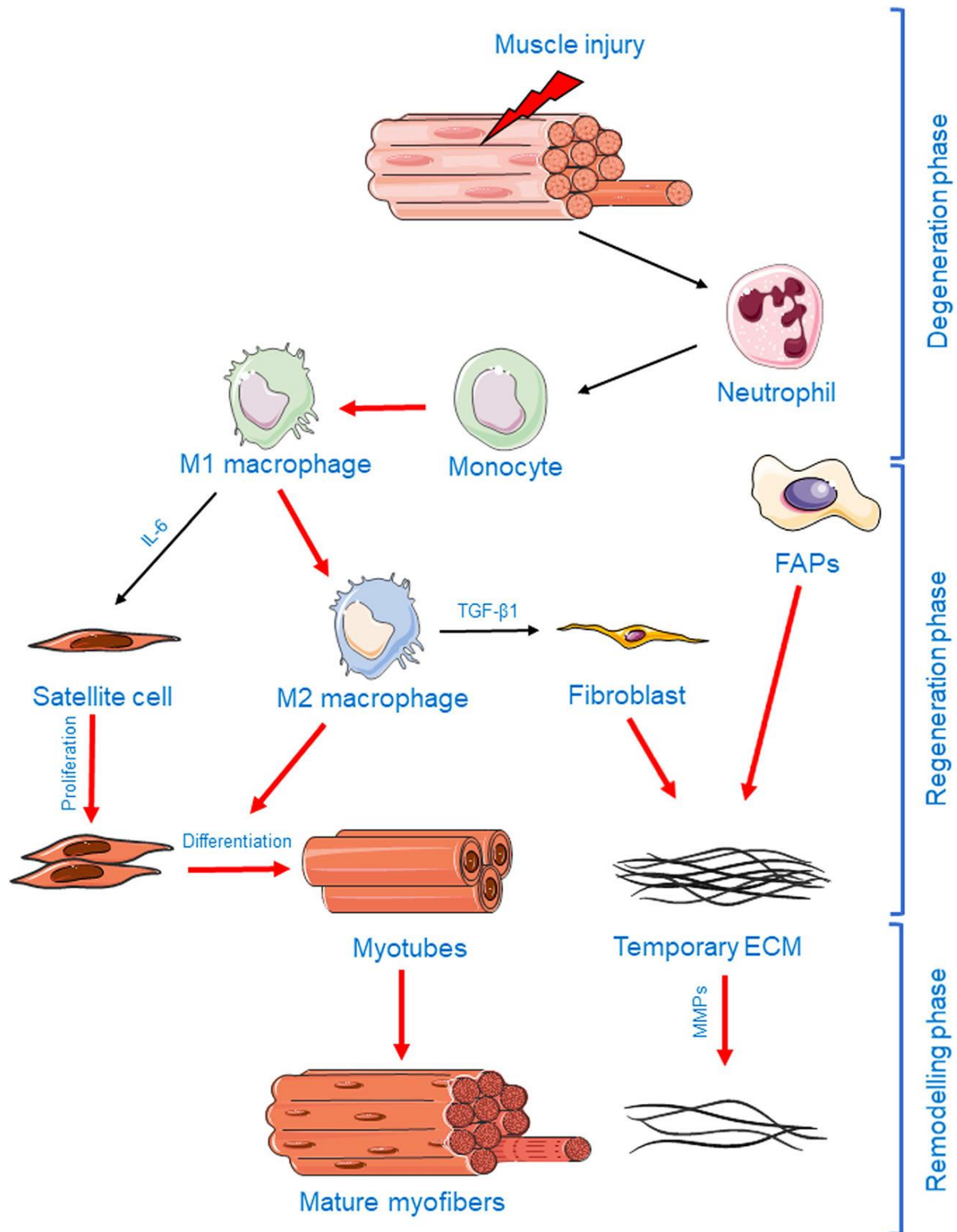


Figure 3- Schematic representation of the different phases of skeletal muscle regeneration. Following injury, inflammatory cells will be recruited to the damaged region. This first phase is characterized by myofiber necrosis and tissue inflammation, as well as initial fibrosis. Satellite cells will start to proliferate at the beginning of the regeneration phase, while M2 (anti-inflammatory) macrophages will promote their differentiation. Other cell types as fibroblasts and fibro-adipogenic progenitors (FAPs) will start to remodel a temporary extra-cellular matrix (ECM) that will be subjected to further refinement during the remodelling phase by the action of metalloproteinases (MMPs) (Figure from Mahdy 2018) (Mahdy 2018).

Skeletal muscle recovery, while being similar in respect to expression of the genes involved, presents some key differences from the embryonic myogenesis. Indeed, skeletal muscle regeneration after an injury can be divided into three stages: a degenerative phase, a regeneration phase and a final remodelling phase, as shown in Figure 3. Almost immediately after the injury, the damaged area will be subjected to myofiber degeneration with cell necrosis and inflammatory cells infiltration (Tidball and Villalta 2010) (Figure 4). Neutrophils are the first inflammatory cells recruited to the damaged sites, followed by monocytes that will convert into macrophages. Macrophages found in the skeletal muscle are usually divided in two types: M1 and M2 (Saclier, Cuvellier, et al. 2013; Ogle et al. 2016; Wynn and Vannella 2016). M1 macrophages are the first to appear. They are referred to as classically activated or pro-inflammatory since they release inflammatory cytokines as IL-1, IL-6 and TNF- α . These cells will start a first response to damage by phagocytosis of necrotic tissue and activation of others immune cell populations (Massimino et al. 1997; Cantini et al. 2002). In addition to these effects, they are capable to promote satellite cells proliferation through different molecular signaling pathways, secreting IL-6 (Saclier, Yacoub-Youssef, et al. 2013) or NF- κ B (Bakkar et al. 2008). M2 macrophages, known as alternatively activated or anti-inflammatory macrophages, are activated after M1 macrophages and exert an anti-inflammatory effect on the recovering muscle. These cells terminate the inflammation and contribute to tissue remodelling and satellite-cell differentiation (Saclier, Yacoub-Youssef, et al. 2013). They produce TGF- β 1, that promotes the synthesis of ECM components, such as fibronectin and collagen (Zanotti et al. 2007). TGF- β also inhibits myoblast differentiation by suppressing the expression of MyoD and myogenin (Brennan et al. 1991; D. Liu, Black, and Derynck 2001).

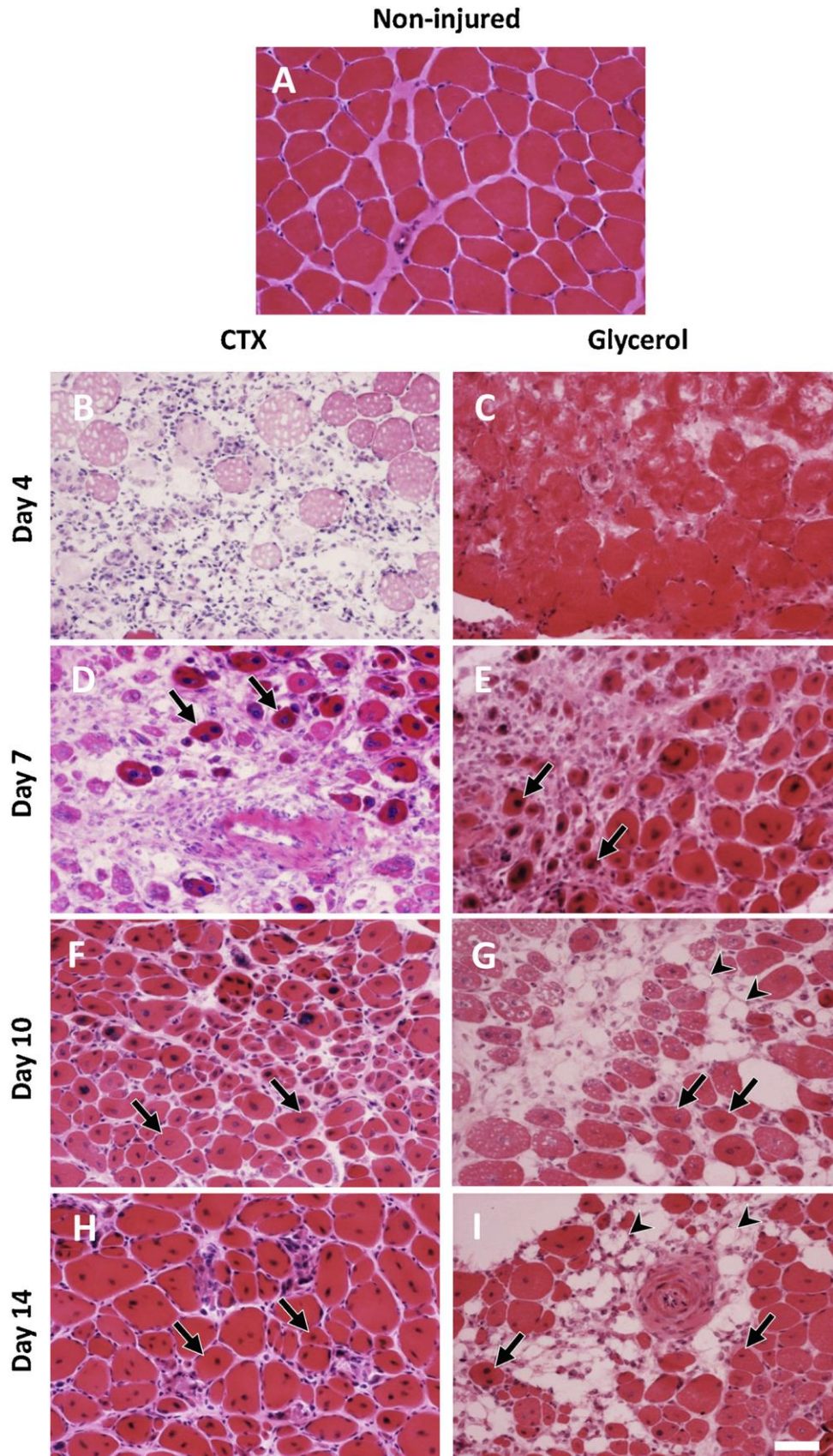


Figure 4- Hematoxylin-eosin (HE) staining of uninjured, cardiotoxin or glycerol-damaged tibialis anterior (TA) muscle cross-sections. In this figure the structural changes between an uninjured, a cardiotoxin (CTX, B, D, F, H) and glycerol-treated (C, E, G, H) muscle are shown. To note the infiltration of monocytes at day 4 (evident in the CTX model, B) and the presence of center-nucleated fibers (arrows) in both models at day seven, ten and fourteen after the damage procedure was administered. Scale bar: 50 μ m (figure from Mahdy, 2014).

During the regeneration phase, satellite cells undergo activation, proliferation and differentiation towards myotubes as schematized in Figure 5. After having aligned along the direction of the future muscle fiber, myocytes fuse to form a new muscle cell (Morgan and Partridge 2003; Tedesco, F. S., Dellavalle, A., Diaz-Manera, J., Messina, G., & Cossu 2010). Those newly formed myofibers express an embryonic isoform of myosin heavy chain, the embryonic myosin heavy chain (eMHC) (Schiaffino et al. 1986; Murphy et al. 2011; Judson et al. 2013; McDonald et al. 2015; Kastenschmidt et al. 2019) and present their nuclei in a central position (Judson et al. 2013; McDonald et al. 2015; Arecco et al. 2016; Kastenschmidt et al. 2019). Although Satellite cells are frequently considered to be the principal cell type involved in muscle regeneration, recently also other cell populations showed to be involved in the recovery, such as fibroadipogenic progenitors (FAPs). The FAPs proliferate during the regeneration phase and participate in the formation of the temporary ECM (Mahdy 2018), that will serve as scaffold for the correct formation of new muscle tissue. It was shown that the presence of a scaffold composed of newly deposited ECM and residual ECM can heavily influence the muscle regeneration, as the scaffold can affect the orientation of newly formed muscle fibers (Webster et al. 2015). Moreover, the temporary ECM provides some sort of structural stability to the muscle and diminishes the stress that could affect the remaining functioning part of the organ (Webster et al. 2015). On the other side, the fibrotic tissue forming this way does not generate new muscle fibers, and an excessive scarification can hinder the recovery (Mann et al. 2011; Garg, Corona, and Walters 2015; Delaney et al. 2017).

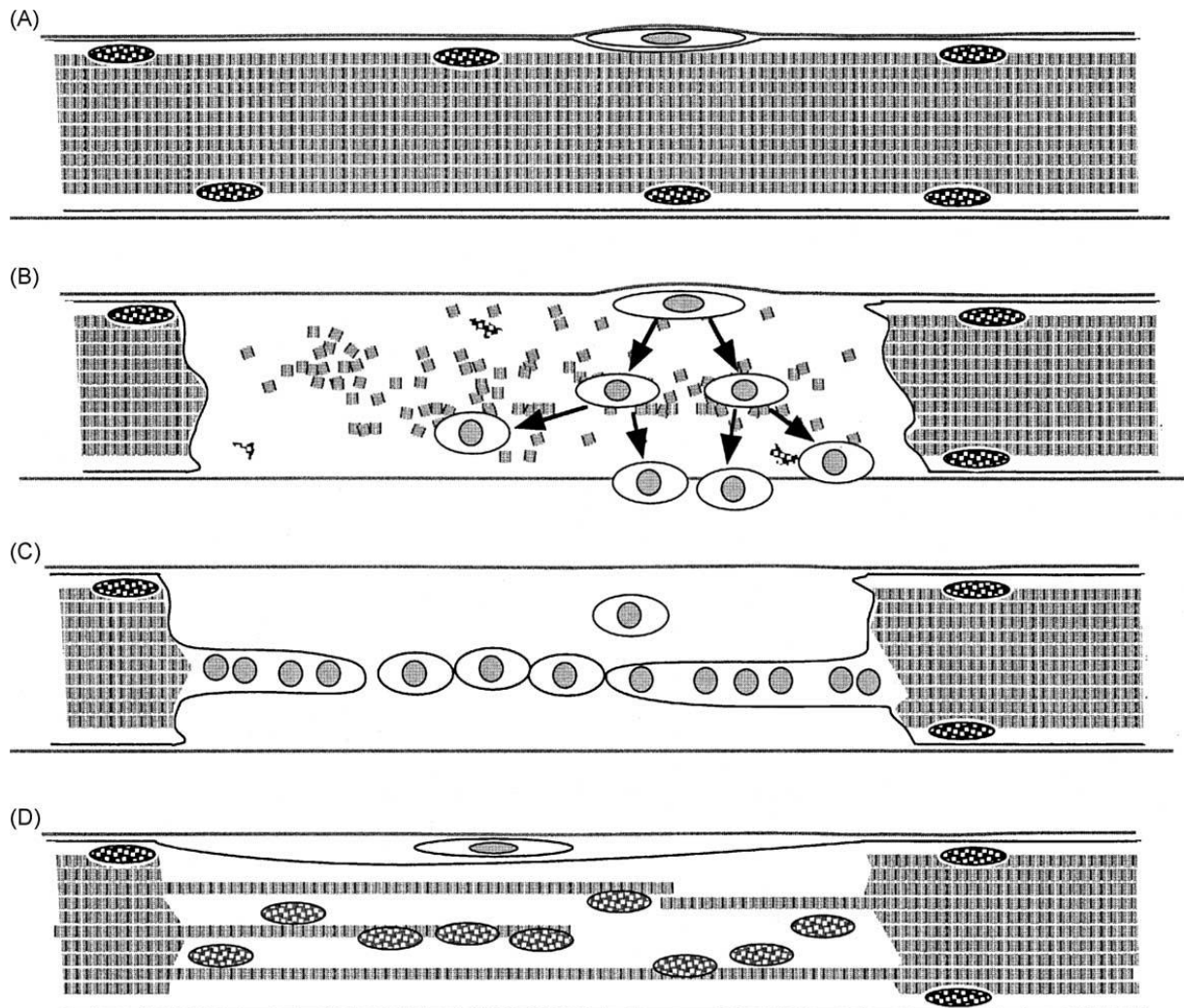


Figure 5- Schematic representation of a regenerating skeletal muscle fiber. (A) Normal muscle fiber with myonuclei (dark) and satellite stem cells (grey nuclei, white cytosol). Upon sensing damage to the muscle fiber (B), satellite cells proliferate and migrate in the interested area. At this stage they will start their differentiation. After they align along the direction of the future muscle fiber (C) they will further differentiate into myotubes, who will present transiently center-positioned nuclei (D) (figure from Morgan and Partridge, 2003) (Morgan and Partridge 2003).

The final stage of muscle recovery is the remodeling phase, in which newly formed myotubes mature into myofibers and the ECM is remodeled by metalloproteinases (Laumonier and Menetrey 2016). In this phase, depending on the severity of the initial damage and overall the grade of success of the tissue regeneration, fibrosis and scar tissue formation can be observed (Laumonier and Menetrey 2016). Depending on the objective of the study, fibrosis, i.e. as excessive production of ECM proteins, might be either desired or considered as an obstacle. When studying muscle regeneration, its reduction or prevention is preferred, because scar tissue hinders the complete recovery of the skeletal muscle (Mann et al. 2011; Garg, Corona, and Walters 2015; Delaney et al. 2017).

Although presented here as sequential, degeneration, regeneration and remodelling stages are not so clearly separated during skeletal muscle degeneration and recovery: they overlap and interplay, creating a complex environment from several points of view, like the number of cell populations involved, chemical signaling, mechanic stimuli and gene expression. Such

complexity, although being more and more understood, is still not resolved and needs further investigation. To do so, different *in vivo* models have been developed, and the selection of the most appropriate one is critical for the resolve of the biological questions posed.

1.3 Skeletal muscle damage models

In order to study muscle degeneration and recovery, several animal models have been developed (Arnold et al. 2007; McCarthy et al. 2011; Czerwinska et al. 2012; Iwata, Suzuki, and Wakabayashi 2013; Tiryakioglu et al. 2015; Hardy et al. 2016; Mahdy 2018). Their outcome can change greatly, and every model must be chosen carefully depending on which aspects are of interest for the researchers. Skeletal muscle damage models differ in the injury mechanism they exploit and in the type of damage caused, that can affect greatly the degeneration/regeneration kinetics of the tissue. A recent classification was presented by Mahdy (Mahdy 2018), as shown in Table 1. Mahdy organizes the different muscle damage models in three main categories, according to the nature of the method used to induce the damage: physical, chemicals induced, and ischemic injuries.

| Category | Injury model | | Mechanism of myofiber damage | Basal lamina | Regeneration outcome | Disadvantage |
|--------------------------|---------------------------------|-----------------|---|-------------------|---|---|
| Chemical injuries | Local anesthetic (Bupivacaine) | | -Sarcoplasmic reticulum dilatation -Subsarcolemmal accumulation of swollen mitochondria | No effect | -Early inflammatory cellular invasion -Rapid onset of regeneration | -Large volumes of anesthetic can induce systemic effects -Different species-related susceptibility |
| | Biological toxins (Cardiotoxin) | | -Calcium influx into myofiber's cytoplasm -Mitochondrial swelling, lysis of mitochondrial matrix | No effect | -Efficient regeneration -Mild transient fibrosis | -Interfere with neuromuscular transmission -Mild fibrosis |
| | Other chemicals | Barium chloride | -Alters resisting membrane potential | No effect | -Uniform and rapid regeneration onset | -Has mild effect with patches of uninjured myofibers |
| | | Glycerol | -Alters myofiber permeability | Disruption | -Impaired regeneration with ectopic adipocytes and fibrosis | -Fibrosis develops at late regeneration stage |

| | | | | | |
|--------------------------|----------------------|--|---------|---|---|
| Physical injuries | Freezing | -Death of all types of cells in the affected region | Rupture | -Regeneration with considerable scar tissue formation | -Limited muscle area damaged |
| | Crushing | -Myofiber rupture and hematoma | | | -Destruction of vessels, neurons and nearby tissues |
| | Contusion | | | | -Limited muscle area damaged |
| Ischemic injuries | Ischemia-reperfusion | -Ischemic lesions with extensive myofiber death and acute inflammation | Damage | -Impaired regeneration with increased fibrosis | -Failure to restore functional characteristics |

Table 1- Summary of the most used experimental models for skeletal muscle damage. The glycerol-induced muscle damage model, as the one chosen in this study, is highlighted among the methods based on chemical injuries (modified from Mahdy (Mahdy 2018)).

Physical injuries can affect several muscle compartments and result in severe damage, but their reproducibility is low as they heavily rely on the operator ability. Also, physical methods promote a heavily fibrotic environment with scar tissue formation, that hinder a complete muscle recovery (Garg, Corona, and Walters 2015; Laumonier and Menetrey 2016).

Ischemic injuries are performed by blocking and then subsequently reperusing a major artery in the chosen muscle. This leads to myofiber death and severe inflammation, ultimately resulting in an impaired regeneration together with an enhanced fibrosis (Vignaud et al. 2010). Its reproducibility is impaired by the time and the severity of blood flow restriction, that can directly affect the amount of tissue interested by the damage. Those are considered the major disadvantages of this practice in ethical and reproducibility terms (B. Carlson 2008).

Injection of myotoxins is the most diffused method (Chazaud 2016), due to its simplicity and reproducibility. Myotoxins can be divided in three categories: local anesthetics, biological toxins and chemicals. Of the first two categories, the most used compounds are bupivacaine and cardiotoxin (CTX), respectively. Bupivacaine injection causes the sarcoplasmic reticulum to dilate together with an accumulation of swollen mitochondria in the subsarcolemmal region (Politi et al. 2006), leading to the destruction of a large number of myofibers but without affecting the basal lamina nor the satellite cells (Akiyama, Kobayashi, and Nonaka 1992; Politi et al. 2006) and avoiding any ischemic damage. While this method is effectively triggering a degeneration/regeneration mechanism (B. Carlson 2008), the large volumes

needed for the injection (up to the 50% of the volume of the muscle treated) can induce accidental systemic effects. Cardiotoxin is isolated from snake venoms, and is one of the most common methods to cause muscle damage (Czerwinska et al. 2012; Webster et al. 2015). Is able to induce a severe injury to the muscle fibers without affecting the basal lamina (Czerwinska et al. 2012), to the point to leave a space previously occupied by the muscle fibers, used as a supporting structures for muscle regeneration, the so called “hollow fibers” (Webster et al. 2015). Cardiotoxin exerts its effect by causing a calcium influx in the myoplasm leading to mitochondrial swelling and disruption, resulting in fiber necrosis (Mahdy, Warita, and Hosaka 2016). Among the chemical-induced muscle damage models, only the glycerol injection has the ability to disrupt the basal lamina, and so to deprive the muscle of an extracellular structural component that can help its recovery (Webster et al. 2016). Glycerol effects are linked to the ability of this substance to cause, in virtue of being highly hydrophilic, an osmotic shock to the myofiber. Its action has an effect also on other muscle elements, including the basal lamina (Kawai et al. 1990; Pisani et al. 2010; Mahdy et al. 2015). Muscles injured by glycerol injection are characterized by an ectopic infiltration of adipocytes and localized fibrosis (Lluís et al. 2001; Mahdy et al. 2015; Mahdy, Warita, and Hosaka 2016; Hardy et al. 2016). Moreover, muscles lacking membrane-associated proteins, like dysferlin and myoferlin, are more sensitive to glycerol damage (Demonbreun et al. 2014). This feature, along with the muscle cells deprivation of the interaction with extracellular-matrix associated elements that can enhance tissue recovery (Murphy et al. 2011; Iwata, Suzuki, and Wakabayashi 2013; Webster et al. 2016), is typical of this model. Although the damage drawn onto the muscle tissue is extremely severe in the early phases, the organ is able to recover anyway (Arsic et al. 2004; Mahdy et al. 2015; Mahdy, Warita, and Hosaka 2016). For these reasons, glycerol-induced muscle damage can prove an interesting injury model for the study of muscle regeneration.

1.4 The neuromuscular junction structure and function

The neuromuscular junction (NMJ) is a highly specialized major subclass of chemical synapses of the mammalian nervous system, which function is critical for the efficient transfer of information between the lower motor neuron and skeletal muscle. The NMJ structure is tripartite, consisting in the presynaptic motor neuron, the postsynaptic muscle and the glial cells associated to the synapse, the Schwann cells (referred also as terminal Schwann cells, TSCs) (Campanari et al. 2016). The pre- and postsynapse are separated by a narrow space (50 to 80 nm wide), the synaptic cleft (Figure 6A). In the postsynaptic region, the sarcolemma is folded, and on the crest of each of these folds nicotinic acetylcholine receptors (AChRs) are densely clustered. At the bottom of each fold, a region enriched in voltage-gated sodium channels is found (Flucher and Daniels 1989).

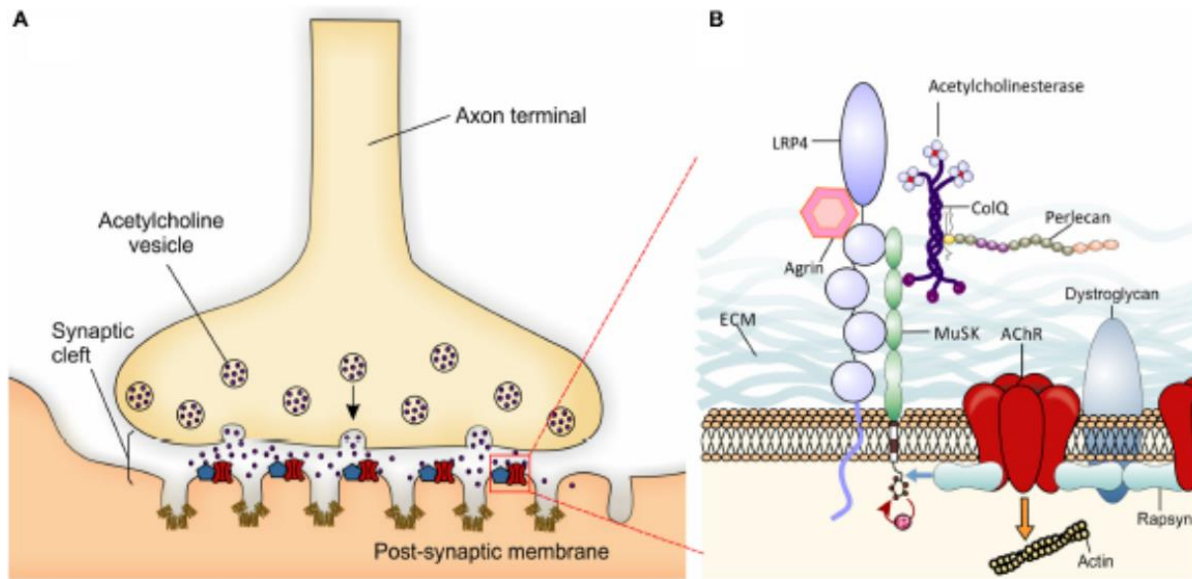


Figure 6- NMJ tripartite structure and the proteins involved in its development and maintenance. In (A) a scheme depicting the NMJ structure is shown, in (B) the different proteins leading to NMJ maturation, organization and maintenance are listed and show in respect to their association to each other. Figure from Campanari et al. (Campanari et al. 2016).

The neuromuscular junction is localized at the end of the motoneuron, and it transmits the nerve signal to the muscle fiber. Every mature muscle fiber is innervated by a single NMJ (Krause 1863).

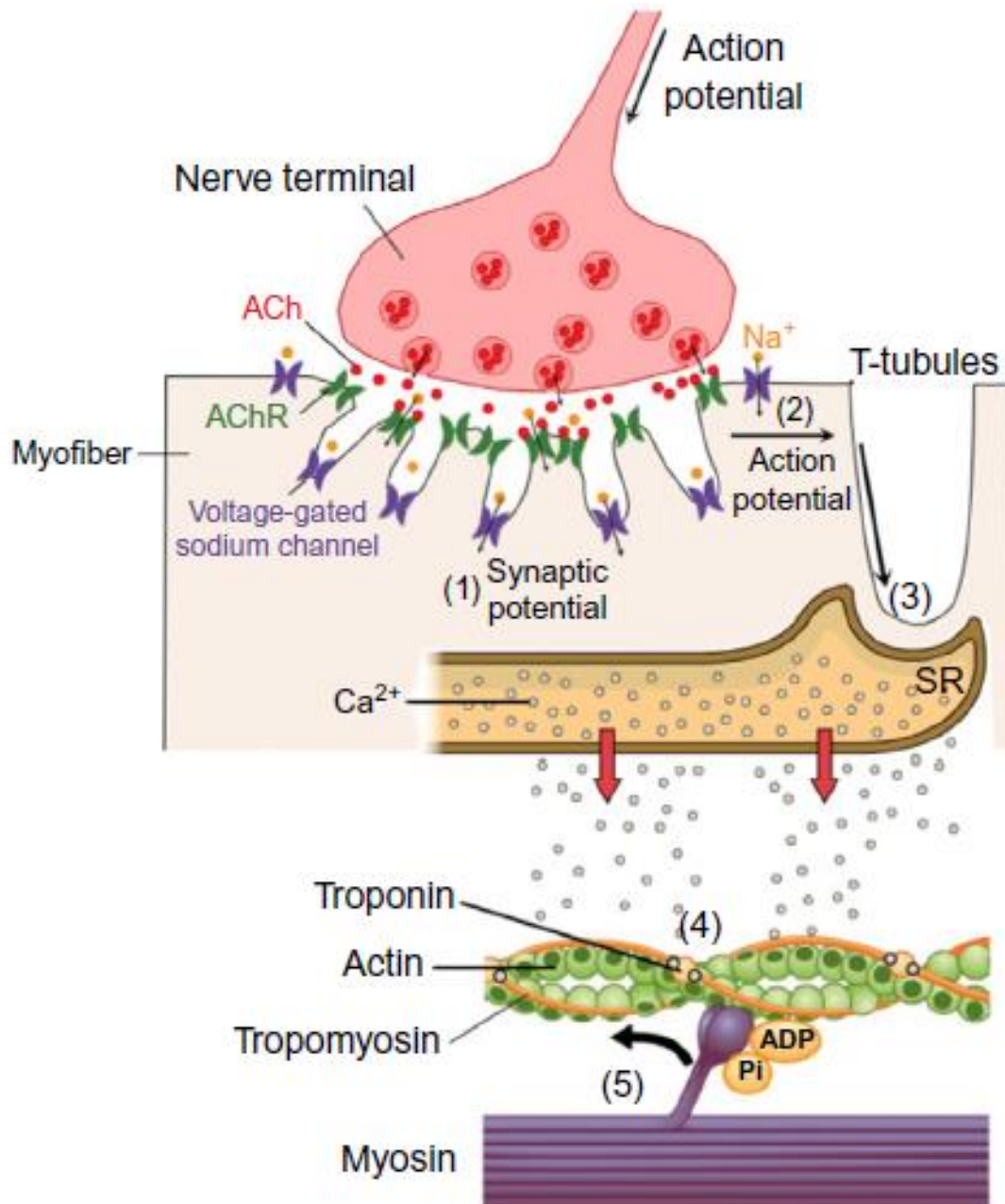


Figure 7- Transmission of the neural stimuli ending in muscle contraction. Acetylcholine (ACh) released into the synaptic cleft from the nerve terminal binds to its receptor (AChR), triggering the transient opening of the cation channel of the receptor (1) and the influx of small cations, that gives rise to a synaptic potential. This localized change in membrane potential leads to the activation of voltage-gated sodium channels, eliciting an action potential (2) that propagates along the myofiber. Once this stimulus reaches the T-tubules (transverse tubules, extensions of the muscle fiber membrane containing a large number of ion channels that reach into the center of the myofiber), voltage-dependent calcium channels open and trigger ryanodine receptors in the sarcoplasmic reticulum (SR) to release calcium ions (3). Calcium then binds to troponin (4), leading to the exposition of binding sites for myosin on the actin filament. Myosin is bound by adenosine diphosphate (ADP) and phosphate (Pi) and forms cross-bridges with actin. The subsequent release of ADP and Pi will generate the stroke that causes the sliding of the thin filament past the thick filament, resulting in muscle contraction (5).

The neuromuscular transmission process is schematized in Figure 7. Its function mediates voluntary muscle contraction. For the neuromuscular impulse transmission, calcium influx upon with motor neuron action potential promotes the fusion of synaptic vesicles at the terminal of the motoneuron at specialized sites, called active zones. This mechanism leads to

secretion of acetylcholine (ACh) in the synaptic cleft, where it diffuses and binds to its receptors, localized in the postsynaptic region. This causes the opening of the AChRs ion channels, generating a current of several hundred nA and then a local depolarization of the myofiber around 40 mV, defined as the endplate potential (EPP) (Tintignac, Brenner, and Rüegg 2015). This induces the opening of voltage-gated sodium channels at the bottom of the synaptic folds, that will give rise to an ulterior muscle action potential. Once this action potential reaches the T tubule, a part of the sarcolemma that reaches into the center of the fiber and triggers the release of calcium ions from the sarcoplasmic reticulum. Calcium ions will bind to troponin, causing a conformational change filament and the tropomyosin to move and exposing the active sites on G actin filaments. Heads of myosin filaments will then bind to those sites, ultimately resulting in muscle contraction. ACh is subsequently degraded by acetylcholinesterase (AChE), an enzyme linked to the basal lamina in the synaptic cleft (as schematized in Figure 6).

1.5 Neuromuscular junction development

In order for the neuromuscular junction to form successfully, pre- and postsynaptic components have to interact during embryogenesis. The motor neuron reaches an already present AChR cluster on the muscle fiber, thus leading to NMJ maturation. Such specialization involves several molecular mechanisms, and although there is no clear consensus on the precise molecular pathway that organizes and leads neuromuscular junction formation and muscle innervation, some key factors have been identified (their organization and the NMJ site is schematized in Figure 6).

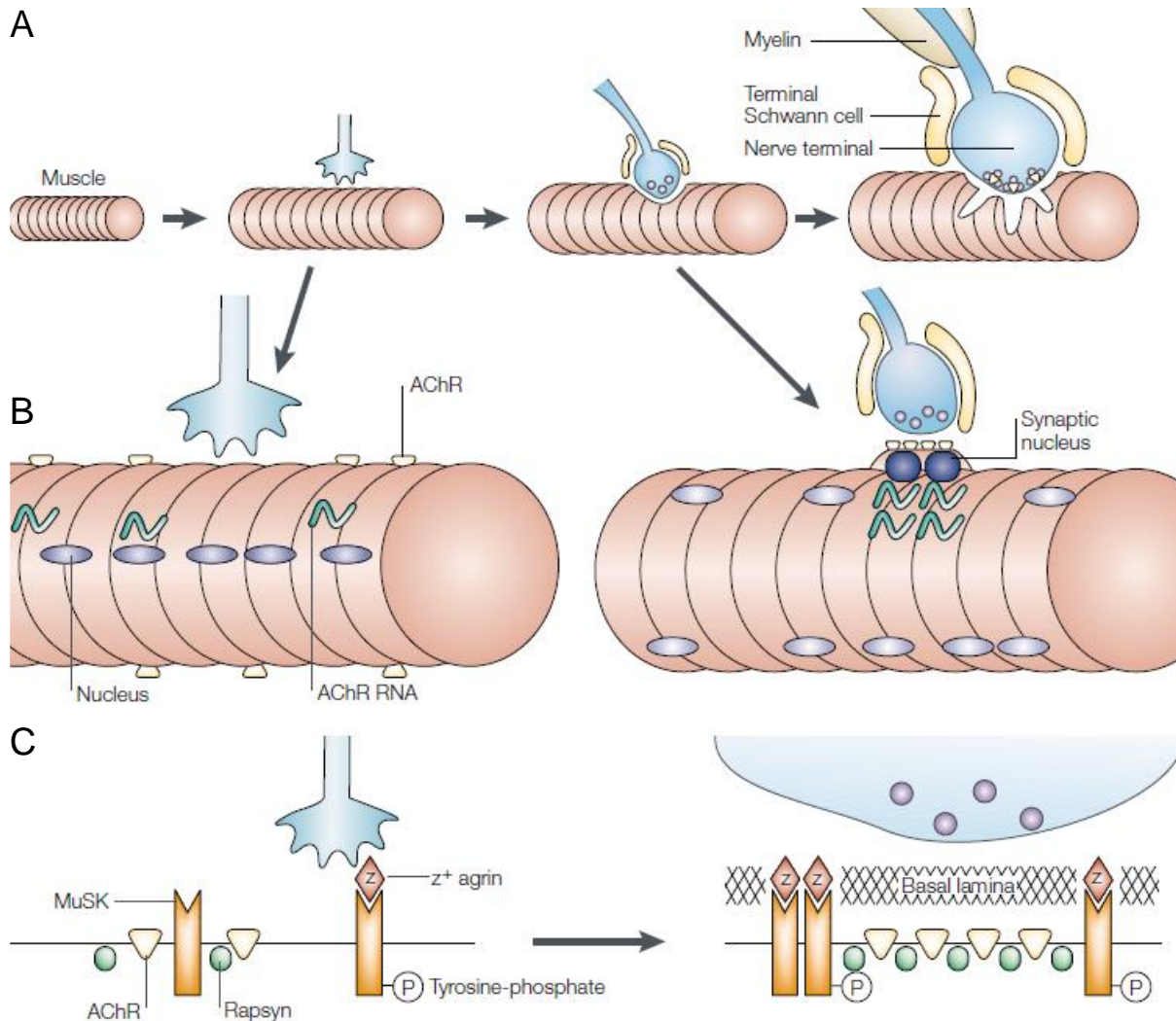


Figure 8- Scheme depicting NMJ development. In (A) is showed how the motoneuron, approaching the muscle fiber, leads to NMJ formation, in particular (B) by promoting AChR accumulation at the future postsynaptic site. In (C) the effect of agrin is schematized: upon its binding to MuSK it promotes MuSK phosphorylation, leading to its association with rapsyn and AChR accumulation. Figure modified from Sanes and Lichtman (Sanes and Lichtman 2001).

Early studies highlighted how muscle basal lamina was implicated during NMJ regeneration and development, as it was providing termination signals for the developing nerve and AChR aggregation signals for the muscle fiber. In particular, NMJ formation was observed to be based on pre-existing postsynaptic differentiation before motor-axon connection to the muscle fiber (Braithwaite and Harris 1979): this mechanism was indicated as “pre-patterning”. Agrin, a protein able to promote AChRs aggregation under the nerve during embryogenesis was detected in 1990 by the McMahan group at Stanford University (McMahan 1990). This protein is secreted by the developing nerve in the muscle basal lamina, promoting local AChR clustering and muscle regeneration. Agrin exerts its action by binding its receptor, the low-density lipoprotein receptor-related protein 4 (Lrp4), thus activating the muscle specific tyrosine kinase receptor (MuSK). Upon its phosphorylation, MuSK recruits rapsyn, a protein constitutively expressed in skeletal muscle cells and linked to AChR (Apel et al. 1997). The presence of rapsyn allows the recruitment at the NMJ site of more AChRs (Sanes and Lichtman 1999; 2001), leading to the final maturation of the postsynaptic structure. Amongst

other, the maintenance of the NMJ is mediated by the dystrophin-glycoprotein complex (DGC), a transmembrane complex linking the myofiber cytoskeleton to the basal lamina and the ECM. This developmental mechanism is schematized in Figure 8.

Subsequent studies challenged this model, as it was reported that postsynaptic differentiation was possible also in absence of the nerve (Kummer et al. 2004) and agrin (Gautam et al. 1996). In a review, Kummer et al. concluded that those studies highlighted the necessity to redefine the role of agrin during synaptogenesis, as its function as synaptogenesis inducer was questioned by recent findings (Kummer, Misgeld, and Sanes 2006). Those studies led to the consideration that, although agrin has an important role in NMJ development and stabilization, other mechanisms are thought to be involved during synaptogenesis as well.

The current opinion is that synaptogenesis is regulated by two mechanisms, one based on pre-patterning and an independent one (Burden 2011), as those two models are not mutually exclusive and postsynaptic differentiation has been observed also in absence of pre-patterning (N. Kim and Burden 2008). Although progress has been made in the understanding of the role of agrin (as stabilizer and inducer) and other molecules, as MuSK, during the synaptogenesis, there is still not a clear consensus on the precise mechanism that regulates this process, and further research is needed.

1.6 Neuromuscular junction damage models

Although animal models to specifically study neuromuscular junction degeneration and recovery have not been developed, NMJs have been studied in several conditions in which skeletal muscle is affected, from aging (Rudolf et al. 2014; Taetzsch, Valdez, and Tech 2019) to dystrophy (Rudolf, Deschenes, and Sandri 2016) to muscle damage models (Röder et al. 2012; S. J. Pratt et al. 2013; S. J. P. Pratt et al. 2014; Tu et al. 2017; Haddix et al. 2018).

The *mdx* mouse model is widely used as a paradigm for muscle dystrophy, as the ablation of the gene enabling dystrophin production leads to mice presenting overall weakened muscles. Moreover, this model is used as well in the study of endplate degeneration, as *mdx* mice NMJs showed a distinct fragmentation in their structure as depicted in Figure 9 (S. J. Pratt et al. 2013; S. J. P. Pratt et al. 2015).

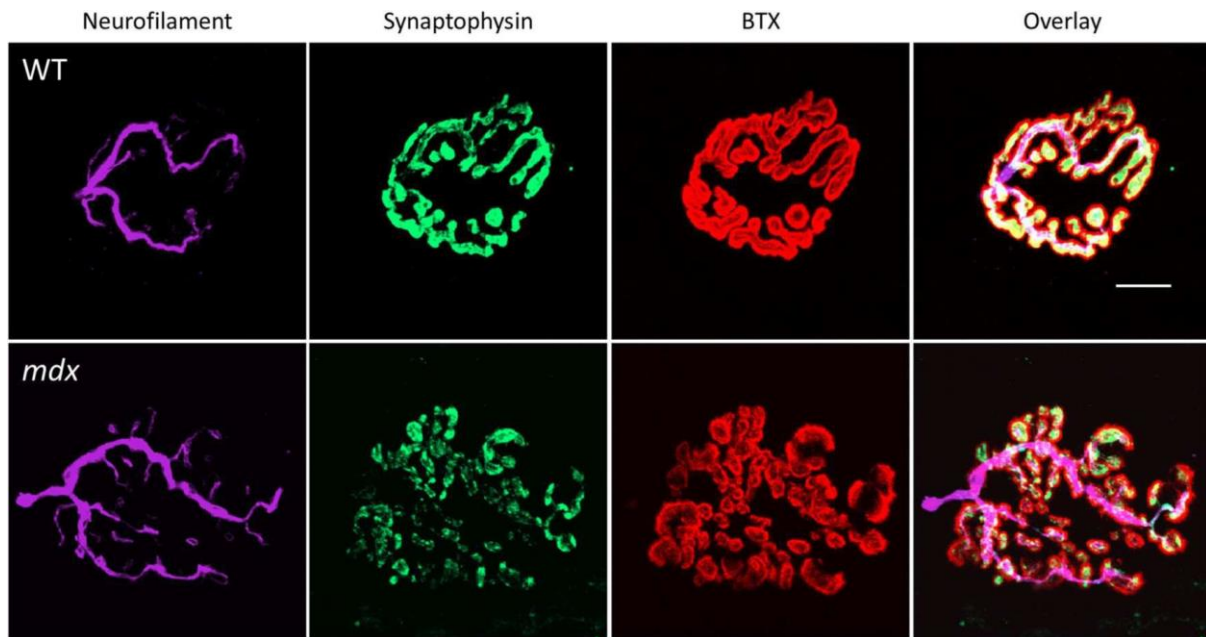


Figure 9- NMJ fragmentation in a wild type (WT) and in a *mdx* mouse. The motoneuron is detected using an antibody against neurofilament (purple), the presynapse with one against synaptophysin (green) and the postsynapse by using a BTX coupled with a fluorophore. It is clear how the NMJ in the *mdx* mouse is fragmented respect to the healthy ones in the wild type. Scale bar: 10 μ m. Figure from Pratt et al. (S. J. P. Pratt et al. 2015).

Endplate degeneration has been studied in this model also together with muscle injury, usually performed with physical methods, as causing myofiber necrosis performing few cuts on the exposed muscle (Haddix et al. 2018), exerting an eccentric contraction on the tissue (S. J. P. Pratt et al. 2014), or by tourniquet injury (Tu et al. 2017). The NMJ in the *mdx* muscles appears fragmented, and when injured endplates appear smaller and even more disrupted. Although NMJs in those conditions show signs of recovery, they will ultimately resume to their fragmented status (S. J. P. Pratt et al. 2014). Along with the *mdx* model, also the SOD1 mouse has been investigated regarding NMJs status, showing NMJ fragmentation (Rizzuto et al. 2015; Sugita et al. 2016; Tremblay, Martineau, and Robitaille 2017; Martineau et al. 2018).

NMJ disruption and recovery has been observed also in models where the nerve was affected, by surgical procedure (nerve excision) (Gwyn and Aitken 1966; Bongers et al. 2013; B. M. Carlson 2014; Komatsu et al. 2018; H. Liu and Thompson 2019) or with the use of toxins for its inactivation (Fex et al. 1966; Duregotti et al. 2015).

More recently, NMJ functionality has been also measured in a novel model of muscle atrophy (Deguise et al. 2020). Differently from what has been observed in the *mdx* mouse, in this model NMJs were denervated, but did not present a fragmentation as severe.

While NMJ development suggests an involvement of the basal lamina on endplate formation, no damage model focused on the disruption of this muscle compartment has never been analyzed regarding the ability of NMJ to recover in such condition.

1.7 Tissue clearing methods

The standard practice in histology has been to cut tissue samples in thin slices to study a specific structure and the presence of distinct molecules. This method has proven to be robust and efficient, but a major drawback resides in the fact that biological structures are inherently tri-dimensional: in order to obtain precise information several slices are needed from the same sample and a “reconstruction” of the 3D structure of interest has to be performed afterwards. Moreover, such reconstruction can be subject to mistakes both during the processing of sections (meaning during the slicing and immunohistochemical staining) and during data acquisition and analysis. Therefore, 3D pictures obtained with this method cannot be treated as a real images, but only as a virtual reconstruction, subjected to mistakes in data collection, analysis or interpretation.

Recent technological advancements in the fields of microscopy and tissue handling promise to overcome these shortcomings of classical 2D-histology. First, the obtainment of tri-dimensional data has become possible with current confocal and LightSheet microscopy techniques. Second, opaqueness of tissue, that has impaired penetration of light through biological samples, has been recently reduced by optical tissue clearing to enhance visualization of whole-mount specimens. Tissue opaqueness is due to two physical phenomena: light absorption (mainly due to the lipidic portion of the tissue) and light scattering, the latter caused by the different refracting indexes present within a complex structure as an organ. The classical classification, as depicted in Figure 10 (Silvestri et al. 2016), of different tissue clearing protocols is based on the main physical mechanism that is used to achieve tissue transparency, and divides the different techniques in four groups: organic solvents, high-refractive index aqueous solutions, hyperhydrating solutions and tissue transformation protocols. Those methods also differ in their ability to clear different tissues, the possible alteration they can cause to the tissue macrostructure and their compatibility with different staining and dyes.

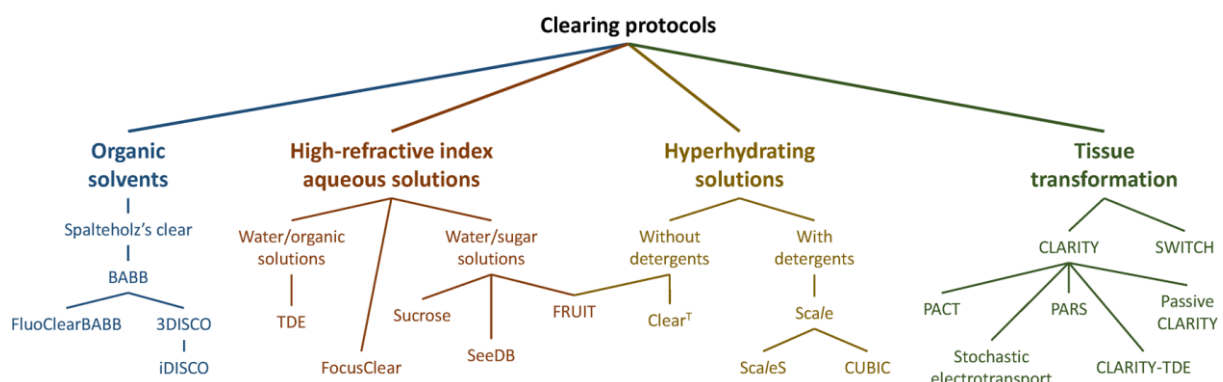


Figure 10- Classification of clearing protocols. The most common taxonomy divides the different methods for tissue clearing in four groups, depending on which mechanism they applied to obtain tissue transparency. Figure from Silvestri, 2016 (Silvestri et al. 2016).

Dating back to 1914, the organic solvent-based methods were the first to be developed, with Spalteholz’s method to substitute water within a fixed tissue sample with a higher refractive

index solution (Spalteholz 1914). More recent approaches along this line followed the same paradigm of dehydrate the fixed tissue and then incubate it in a high-refractive index solution, as done by Dodt et al. (Dodt et al. 2007), that used a combination of benzyl alcohol and benzyl benzoate (referred to as BABB) as index matching solution. Although successful, BABB quenches fluorescence emission after a brief time, so alternatives in terms of use combination of dehydrating agent and index-matching solution were needed. This led to the formulation of 3DISCO (as in “3D imaging of solvent clearing organs) (Ertürk et al. 2012), followed by iDISCO (Renier et al. 2014), uDISCO (Erturk et al. 2016) and FDISCO (Qi et al. 2019), that achieved good results in terms of tissue transparency and fluorescence preservation, as shown in Figure 11. From the BABB protocol, a further improvement based on pH control and a different hydration agent was produced, referred to as FluoClearBABB (Schwarz et al. 2015). Notably, also the FDISCO protocol focused on pH control as an important factor to be monitored in order to preserve protein fluorescence.

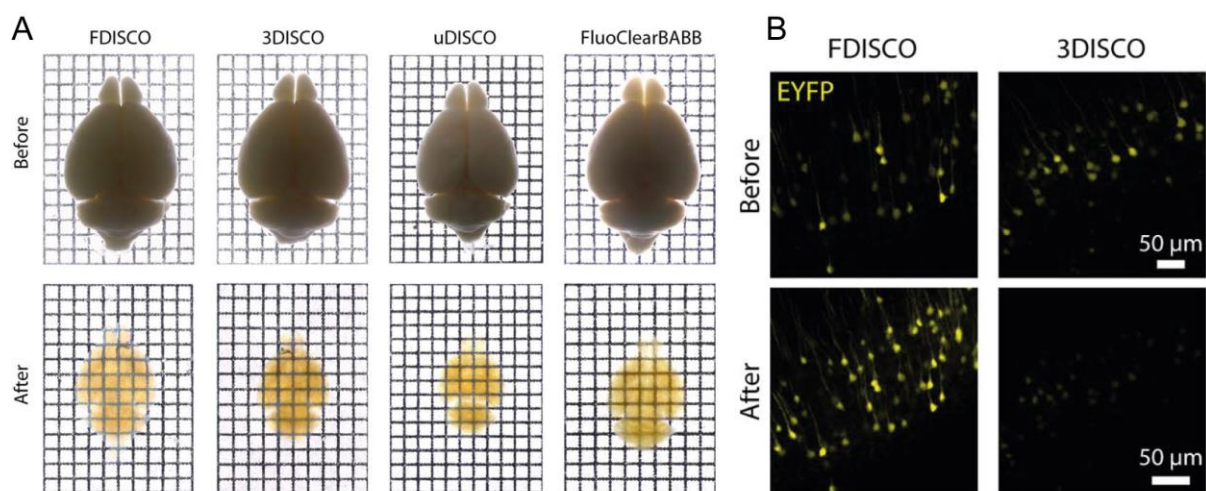


Figure 11- Representative figures of the results obtained with organic solvent-based tissue clearing protocols. Results on mouse brain transparency achieved with different organic solvent based methods (A, different methods as indicated in figure) and in the fluorescent signal preservation (B) of FDISCO respect to 3DISCO protocol (B, methods as indicated in figure, EYFP as endogenous yellow fluorescent protein). Figure adapted from Qi et al., 2019.

As highlighted from the findings on organic solvents-based clearing protocols, fluorescence maintenance can be difficult to achieve. For this reason, some methods aim to maintain the sample in an aqueous environment, that can preserve better fluorescent proteins. Several solutions have been used to obtain such results, including sucrose or fructose solution (the latter used in protocols as FRUIT (Hou et al. 2015) and SeeDB (Ke, Fujimoto, and Imai 2013). Due to the high viscosity of those mixtures, some organic compound alternatives, such as thiodiethanol (TDE), have also been used.

While the methods described previously act on increasing the refracting index of the solutions in which the biological sample is embedded, protocols based on hyperhydrating solutions aim to lower the refractive index of the sample itself. This is achieved through hyperhydrating the proteic portion of the sample and by removing the lipids. Lipid removal can be operated by

using glycerol combined with a detergent and proteins can be hyperhydrated with urea: those are the main components of the *Scale* method, from which *ScaleS* (that uses sorbitol instead of glycerol) and *CUBIC* were developed. In order to avoid the use of detergent as much as possible, *Clear^T* method was used: the lipid removal phase is absent, while protein hyperhydration is performed using formamide aqueous solution.

Lipid removal can greatly increase tissue transparency, but also leads to a decrease of the proteic portion that results in possible loss of biological information. Moreover, while the use of solvents for lipid removal can decrease the refractive index of proteins from $n=1.55$ down to $n=1.48$ (results achievable with the use of hyperhydrating solutions as well), urea can act as a denaturing agent and so eliminate useful epitopes that can normally be exploited in immunohistochemistry procedures (Silvestri et al. 2016). To avoid the loss of protein and useful epitopes, tissue transforming techniques were developed: with those methods the proteins are stabilized by being cross-linked in a gel mesh. In this way the biological and structural identity of the sample is preserved. The first method of this kind was *CLARITY*, which used a polyacrylamide gel where proteins were cross-linked by paraformaldehyde (Chung et al. 2013; S. Y. Kim, Chung, and Deisseroth 2013; Tomer et al. 2014). This stabilization allows the use of strong detergents, like SDS, to remove the lipids. Subsequently, the sample is incubated in a refractive index-matching solution prior to imaging to achieve transparency. The lipid removal phase can be speeded up or increased in efficiency by using electrophoresis or higher incubation temperatures, although those procedures have to be conducted carefully as they can lead to sample damage. A scheme depicting the pipeline used for *CLARITY* is shown in Figure 12.

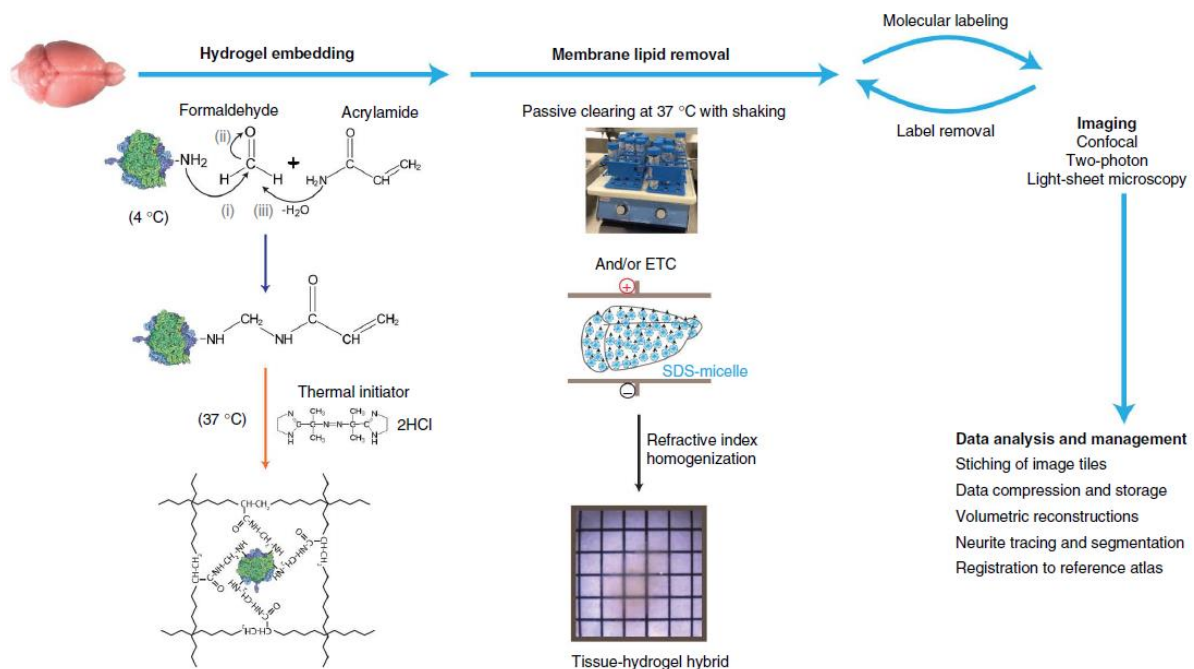


Figure 12- CLARITY pipeline for a mouse brain. The tissue sample is perfused with a formaldehyde and acrylamide solution containing the thermal initiator as well. After the polymerization, the sample will be embedded in a meshwork of fibers preserving its structural and biological identity. A membrane lipid removal phase (passive or with the use of an electrophoretic chamber, ETC) follows to achieve tissue transparency. The resulting sample will be then labelled and imaged with light microscopy. To note that the data analysis and

management phase as to be taken into account, as the volume of sheer data obtained can go from few Gb to ~1 Tb: a dedicated virtual infrastructure for data handling, segmentation and storage could be necessary. Image from Tomer et al. (Tomer et al. 2014).

As described, many different tissue clearing methods have been developed, each one addressing several issues: organic solvent methods focus on achieving a high tissue transparency, but can be harsh for the survival of the fluorescence signal and on the microscope mechanical components coming in contact with them, as well as causing shrinkage of the sample in some cases (that can be considered a disadvantage to be avoided because is a tissue deformation or, as in case of some DISCO protocols, an desirable feature because it can allow imaging techniques that can have size-related limitations, as LightSheet or Digital LightSheet microscopy); methods based on the use of high RI aqueous solutions achieved a good fluorescence preservation, but are not able to achieve great tissue transparency; hyperhydrating solutions address tissue transparency and signal preservation equally, but the loss in biological information is hard to quantify; tissue transforming techniques are efficient, but are time-expensive and complex, has they need a tight control on several different parameters at the same time. In the end, a tissue clearing method has to be selected in virtue of its specific application, considering which structure or epitope is of interest and how it is possible to analyze it. In the specific case of this study, NMJ structure was investigated along with the presence of eMHC in muscle fiber using a fluorophore-conjugated marker for AChR, α -bungarotoxin (α BGT), and an anti-eMHC antibody staining, respectively. For this reason, the MYOCLEAR protocol was developed in-house (Williams et al. 2019). Derived from the CLARITY protocol, MYOCLEAR is based on tissue embedding in an acrylamide hydrogel and applies a gentler detergent treatment than in CLARITY. These differences were necessary, since CLARITY is not compatible with the use of α BGT. As depicted in Figure 13, MYOCLEAR allowed penetration of mouse diaphragm and EDL murine muscle up to a depth of 1200 μ m and the total visualization and segmentation of NMJs in such muscle.

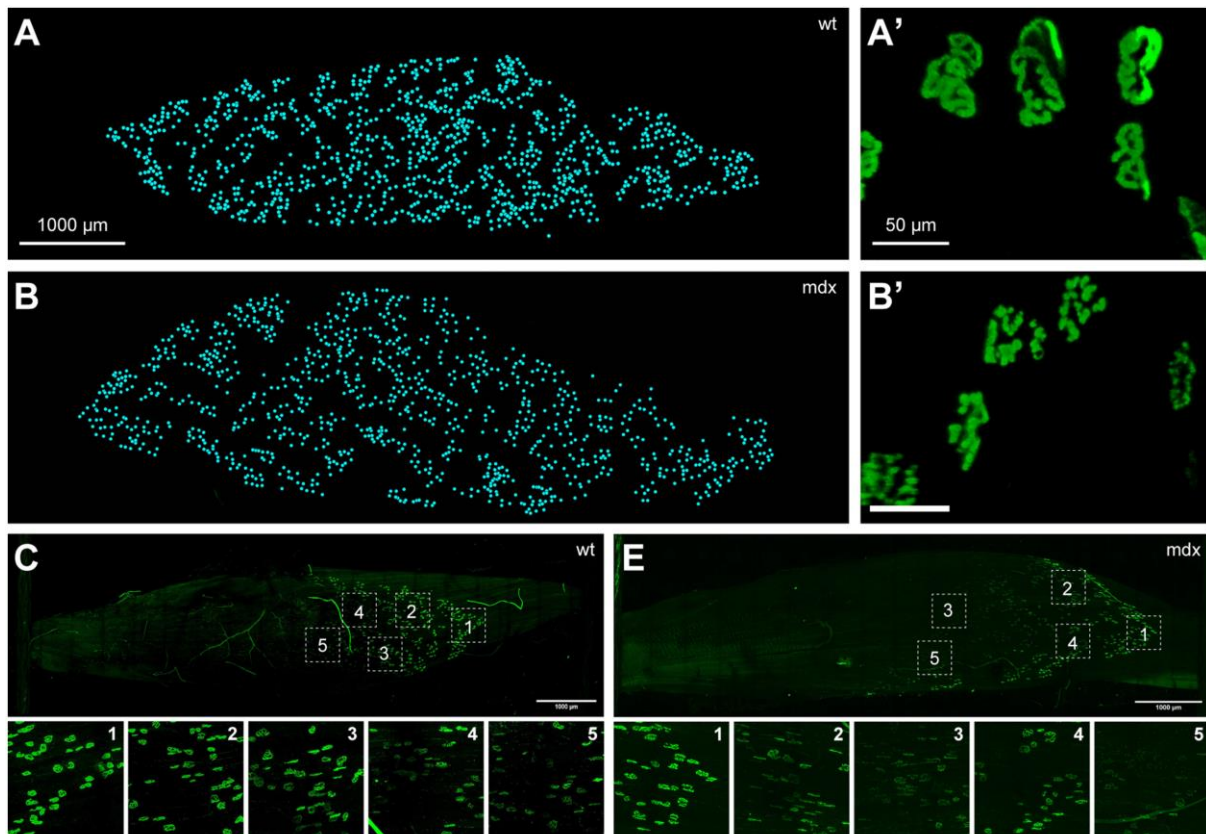


Figure 13- Results on NMJs visualization and segmentation in a murine EDL muscle with MYOCLEAR. EDL muscles from wild type (wt) and mdx mice were cleared using the MYOCLEAR protocol and then stained with BGT linked to a fluorophore to study postsynapse number, position, shape and structure. NMJs were successfully identified through the entire EDL (A,B) and their structure was clearly conserved, with mdx NMJs presenting the fragmentation as expected (A', B'). When parameters describing NMJs structure were measured from different areas of the same muscle, and heterogeneity was found (C, E). Figure modified from Williams et al. (Williams et al. 2019).

1.8 Adipose-derived mesenchymal stem cells (ASCs) and their therapeutic applications

Currently, several stem-cell based therapies are being tested as possible treatment for enhancing muscle regeneration. Different stem-cell sources are being considered for possible clinical application, including muscle-derived stem cells, mesangioblasts, muscle progenitor cells, interstitial cells and mesenchymal/stromal cells (Gois Beghini et al. 2019). This last group comprises the adipose-derived mesenchymal stem cells (ASCs), that present several interesting advantages compared to other sources: ASCs are immune-privileged, readily accessible from lipoaspirates and relatively easy to isolate and expand *in vitro* (Kern et al. 2006; Torres-Torrillas et al. 2019). This last feature also allows for their accurate characterization and production following the good manufacturing practices. They have proven to be interesting for regenerative therapy applications in virtue of two characteristics: their differentiation potential and their trophic effects on other cell types. Even if ASCs are of mesodermal origin, they can be differentiated in cells from ectodermal, mesodermal and endodermal origin (Timper et al. 2006; Radtke et al. 2009; Deshpande, Grayson, and Spector 2015; Si et al. 2019) (the specific cell types obtained are schematized in Figure 14).

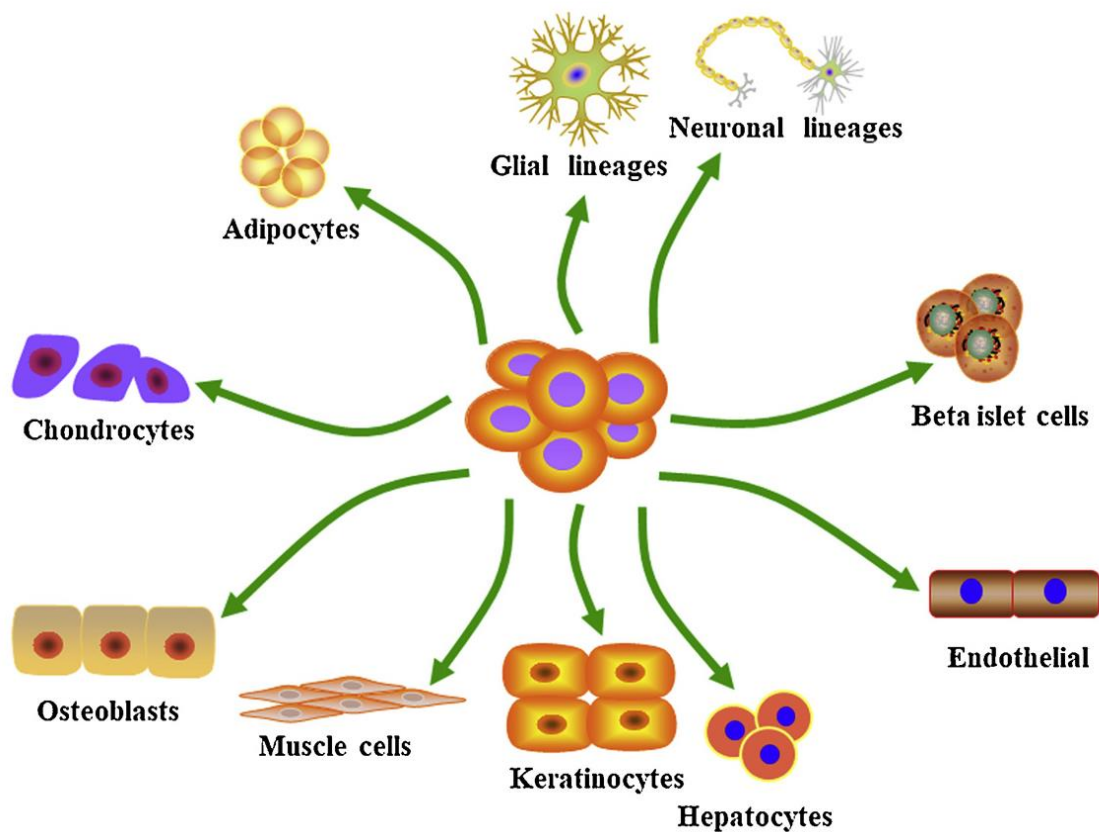


Figure 14- Scheme showing the different cell types that could be obtained by adipose-derived mesenchymal stem cells. Figure from Si, 2019 (Si et al. 2019).

It is still unclear, if for a possible therapeutic application in the treatment of neuromuscular disorder a systemic administration has to be preferred over a local injection in the interested site. A local injection can improve cell engraftment in the affected area, but could be difficult in diseases where large parts of the tissue or different organs are affected, as it is for most of neuromuscular disorders (Gois Beghini et al. 2019). A systemic application can lead to the entrapment of most of the cells injected in specific organs as lungs and liver (Gois Beghini et al. 2019), but, on the other hand, several studies suggest that one of the principal function of stem cell based therapies is linked to their modulatory capability on cellular signaling rather than to their integration in the affected tissue (Law and Chaudhuri 2013; Gorecka et al. 2018; Boldyreva et al. 2019; Mitchell et al. 2019; Torres-Torrillas et al. 2019; Figliolini et al. 2020).

2. Aims of the study

This dissertation has three aims:

- i) the investigation of skeletal muscle regeneration upon damage in an *in vivo* model, considering its sarcomeric components and the common indicators of damage, as muscle cells necrosis and fibrotic tissue deposition, together with the presence of markers associated with muscle regeneration as center-nucleated myofibers (CNFs) and cytosolic expression of eMHC.
- ii) the characterization of NMJ disruption and recovery in such muscle damage model, obtained by analyzing the pre- and postsynaptic compartments.
- iii) the study of the effects of stem cell application with respect to muscle and synapse recovery.

In addition, this study focuses on the possible application of the MYOCLEAR tissue clearing protocol on glycerol-injected muscle in order to study muscle regeneration and NMJs in a three-dimensional aspect, providing some interesting, although preliminary, insights.

Regarding the first point, a glycerol-induced muscle damage model was selected among those available. This choice was based on two characteristic effects of glycerol on the muscle, namely its capability to destroy the basal lamina and its reproducibility. While most studies on glycerol-induced muscle damage model use quantities of 50-100 μl of glycerol solution at different concentrations (most commonly 50% in saline solution) per muscle treated, usually *gastrocnemius* or *tibialis anterior* (TA) muscles (Lluís et al. 2001; Mahdy et al. 2015; Mahdy 2018). Similar protocols are applied to induce rhabdomyolysis in order to study acute kidney injury (Korrapati, Shaner, and Schnellmann 2012; Huang et al. 2018; Reis et al. 2019). Since the interest of this study resides more into investigating skeletal muscle and synapse regeneration, a milder approach was chosen. One group reported that a dose of 25 μl of 50% glycerol solution (in saline) per TA muscle is able to cause a limited damage with adipocyte infiltration, necrosis and fibrosis (Arsic et al. 2004). Indeed, a similar quantity was used (20 μl) in this study. With this study, the possibility to efficiently trigger a cycle of muscle degeneration and regeneration was tested. The use of smaller glycerol doses could result advantageous, as it could lead to better animal condition during the experiments and study reproducibility.

Moreover, as NMJ status was usually assessed in genetic models or after denervation, the pre- and postsynaptic compartment of the motor endplate where monitored, in order to study eventual NMJ disruption and recovery. Endplate degeneration and regeneration, while being

extensively studied in other animal models, have never been investigated in condition where the basal lamina was directly damaged, as happens in glycerol-induced injuries.

After having successfully characterized the damage model, ASCs therapeutic effects were tested. Thanks to the precious collaboration with professor K. Bieback, this study was able to test their systemic application to the glycerol-induced muscle damage model. ASCs are immuneprivileged and, since using lipoaspirates as source, easy to isolate and ethically available. For those reasons, ASCs and ASCs-derived products were evaluated as good candidates for possible therapeutic application in several treatments. In this study, human ASCs were administered systemically shortly after the glycerol injection in the TA was performed. Then, similar timepoints to the ones at which the damage model was monitored were chosen, along with all the markers used. This approach made possible to analyze muscle fiber necrosis, tissue fibrosis, muscle cells structure preservation and their regenerative state. The size and number of muscle fibers were measured as well. The same analysis and quantification performed for characterizing NMJ disruption and regeneration in the glycerol-induced muscle damage model were performed also in the animals where ASC treatment was applied, with the exception of one of the time points used to characterize the model was not repeated in the ASC treatment, as it did not provide interesting findings (the day eight after the injection).

The comparison between the glycerol-induced muscle damage model and the muscles that were subjected to the ASCs treatment would provide important information on their possible application in enhancing muscle recovery. Moreover, the focus on NMJ in such model and treatment is a complete novelty, as NMJ status and structure have never been observed before in this experimental condition. This can allow the researcher to obtain new insights not only on the muscle capability to regenerate, but also on the NMJ recovery.

3. Animals, materials and methods

3.1 Animal experiments

All animal experiments were approved by the local authority (Regierungspräsidium Nordbaden, Karlsruhe/Germany in agreement with EU guideline 2010/63/EU; license G-139/18) and conducted in accordance with the German Animal Protection Law. To induce damage to the skeletal muscle, 20µl of 50% glycerol solution diluted in physiological saline were administered in the *tibialis anterior* (TA) muscle of two months old C57BL6 female mice, previously anesthetized. The same volume of saline solution was injected contralaterally as a sham. Foot contraction was used to determine if the injection was performed correctly (as shown in Figure 15), as it appeared few seconds after the glycerol injection. While still anesthetized, mice were also treated with painkillers and monitored up to 6 hours after the procedure. Subcutaneous injections of 500 µl of saline solution were administered every hour to avoid dehydration, while the animals were kept in a heating chamber at 37°C in order to avoid hypothermia. Once the animals showed sign of recovery, they were transferred to normal cages. Muscles dissected from animals that, after injection, did not present any contraction were also lacking any sign of damage at early phase (three days after the treatment). For this reason, in such animals the procedure was evaluated as unsuccessful and they were not considered in further analysis. Notably, this hindlimb contraction lasted around 10 minutes after the glycerol injection, not hindering the mouse motility. The animals in which the injection was successful were euthanized by cervical dislocation three, five, eight, or eleven days after the procedure and the muscles dissected.

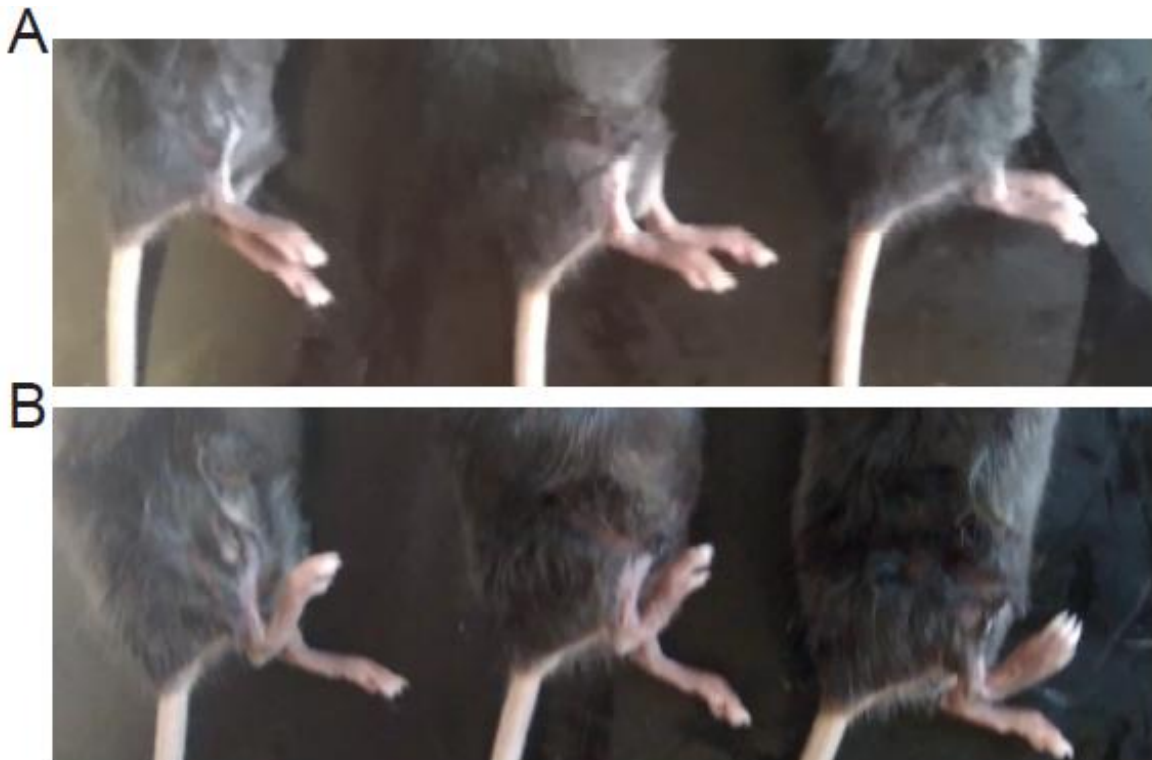


Figure 15-Successful glycerol injection in the tibialis anterior leads hindlimb contraction. In the upper panel (A), mice hindlimbs are showed before the treatment, in the lower panel (B) the same mice are showed less than a minute after 50% glycerol solution (right hindlimb) or saline (left hindlimb) injection. The contraction in the glycerol-treated limb is evident.

Where ASCs were applied, 1 million cells diluted in 100 μ l of sterile PBS were injected via tail vein directly after glycerol treatment, whose was administered as previously described. In this case, animals were euthanized by cervical dislocation and dissected three, five, and eleven days after the injection. At least three animals for each timepoint and condition (glycerol and ASC with glycerol) were analyzed. A scheme of the experimental design is shown in Figure 16.

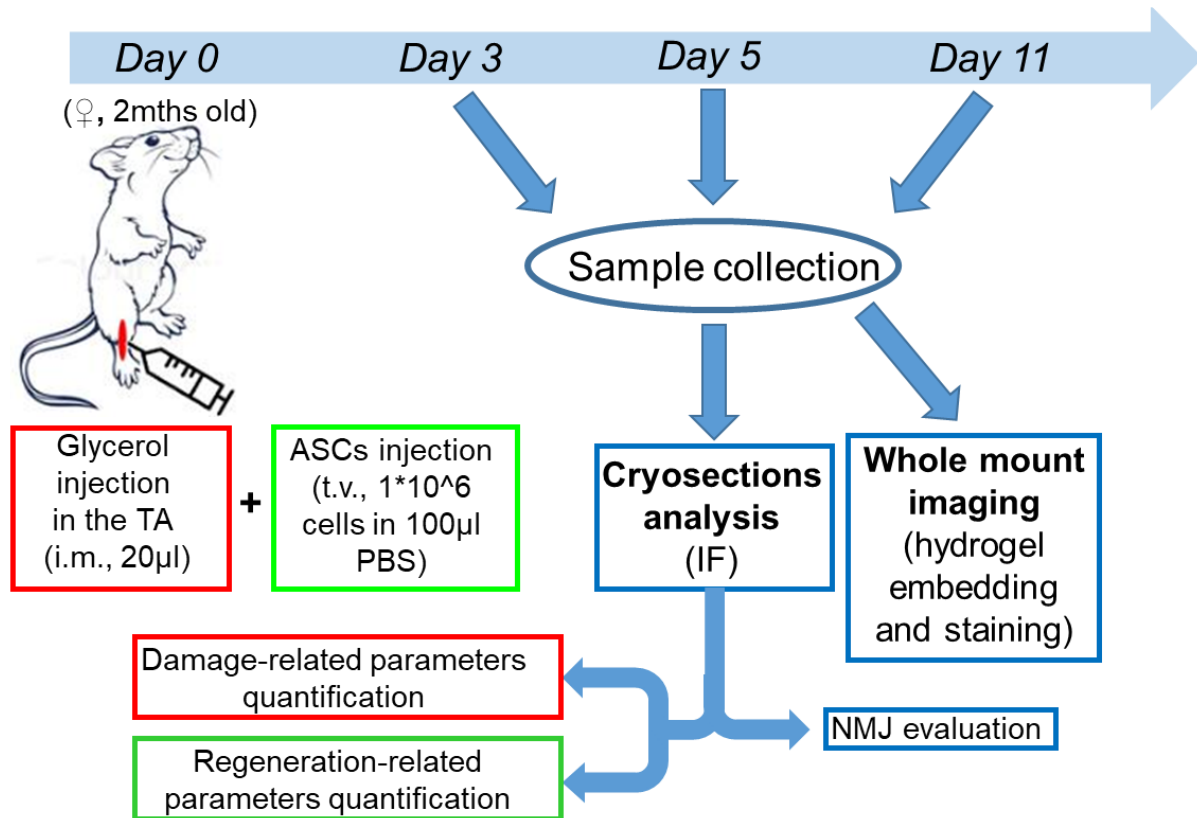


Figure 16- Scheme of the experimental design for the glycerol-induced muscle damage model. The days indicated start from the glycerol injection day (Day 0). 20 µl of 50% glycerol solution in saline solution were injected intra-muscle (i.m.). When adipose-derived stem cells (ASCs) treatment was applied, 1×10^6 cells resuspended in 100 µl of sterile PBS were systemically applied via tail vein (t. v.) soon after the glycerol injection was performed. Following dissection (Sample collection), TA muscles were snap-frozen in liquid nitrogen and embedded in OCT. Soon after cryosections from those muscles were obtained and subjected to immunofluorescence (IF) analysis in order to quantify both muscle damage and its recovery, along with the status of the endplates. When glycerol injection without the stem cell treatment was analyzed, samples were collected three, five, eight and eleven days after the injection. Where ASCs were applied, the days considered for sample collection were three, five and eleven days after the injection.

3.2 Adipose-derived mesenchymal stem cells (ASCs)

ASCs were kindly provided by Prof. K. Bieback's group, with the help from Daniela Nardozi (Prof. N. Gretz's group) for their expansion and transport to the animal facility. ASCs were isolated from adult adipose tissue obtained from lipoaspirates of healthy donors, after obtained informed consent (Mannheim Ethics Commission II vote numbers 2010-262 N-MA, 2009-210 N-MA, 49/05 and 48/05), as described before (Bieback et al. 2012). Briefly, the lipoaspirate was washed with sterile PBS to remove cellular debris and red blood cells and digested with 0.15 % w/v collagenase type I (Sigma-Aldrich) for 45 min at 37 °C. After washing, the pellet was resuspended in medium (DMEM low glucose, 10 % human AB serum, 100 U/ml penicillin, 0.1 mg/ml streptomycin and 4 mM L-glutamine), plated and incubated overnight at 37 °C, 5 % CO₂. After one day, the non-adherent and red blood cells were removed. Expanded cells were characterized regarding their proliferation capacity, immune phenotype, and adipo- and osteogenic differentiation potential, as described previously (Bieback et al. 2012). Before injection, ASCs were seeded at 750 ASC/cm² and

expanded. On injection days, ASCs were trypsinized for 5 min at 37 °C and washed once with medium. The ASC pellet was then resuspended in sterile PBS at a concentration of 1×10^7 cells / ml shortly before the injection.

3.3 Immunofluorescence analysis

Immediately after dissection, tibialis anterior (TA) muscles were covered with a thin layer of Frozen Section Compound (Leica) and frozen on liquid nitrogen. Transverse cryosections of 15 – 20 μm thickness were produced using a Leica CM1950 cryostat, and then positioned carefully on glass microscope slides (Thermo Scientific) and subsequently immunostained for epitope detection. For immunohistochemical analysis, antibodies against specific antigens coupled directly to fluorescent dyes or with the use of fluorophore-coupled secondary antibodies and dyes. Cryosections were permeabilized with 0.1 % TritonX-100 / PBS for 10 minutes at room temperature and, after three washing steps in PBS (5 minutes each), incubated with 2 % BSA / PBS for two hours to avoid unspecific binding of primary antibodies. Sections were then incubated overnight at + 4 °C with primary antibodies diluted in 2 % BSA / PBS. After three washing steps in 2 % BSA / PBS, sections were incubated with the secondary antibodies / dyes / toxins in 2 % BSA / PBS for three hours at room temperature and in the darkness. Antibodies, dyes, and dilution rates are listed in Table 3. Subsequently, after 15 minutes incubation with DAPI (Sigma) in 2 % BSA / PBS and three more washing steps with PBS (5 minutes each), glass slides were left to briefly dry and then mounted in Mowiol. The samples were then analyzed at the confocal microscope the day after. On the following day, images were taken using a Leica TCS SP8 microscope equipped with 405 nm, 488 nm, 555 nm, and 633 nm lasers, and Leica HC PLAN APO 20x/0.75 IMM CORR CS2 objective and at z-steps of 3 μm . For every sample, three to five entire cryosections from the central portion of the muscle at an intersection interval of roughly 200 μm were visualized. Where ASCs were analyzed, they were immunostained with a slightly different protocol than the one used for TA muscles cryosections. Cells on Eppendorf 8 chamber cell imaging slides were briefly fixed with 2% PFA / PBS and then permeabilized with 0.1 % TritonX-100 / PBS for 5 minutes at room temperature and, after three washing steps in PBS (5 minutes each), incubated with 2 % BSA / PBS for one hour to avoid unspecific binding of primary antibodies. The cells were subsequently incubated overnight at 4 °C with the primary antibody diluted in 2 % BSA / PBS. After three washing steps in 2 % BSA / PBS cells were incubated with the secondary antibody and DAPI diluted in 2 % BSA / PBS for 45 minutes and in the darkness. After three more washing steps with PBS and one with ddH₂O, the slides were mounted in Mowiol and analyzed using the same microscope and objective used for the muscle cryosections. As for the muscle cryosections, antibodies, dyes and dilution rates are indicated in Table 2 and Table 3.

| Primary antibody | Company | Catalog number | Lot number | Dilution rate |
|--|------------------|-----------------|------------|---------------|
| Dystrophin antibody | Invitrogen | PA 1-21011 | TK2665551J | 1:200 |
| Myosin 3 antibody | Biorbyt | orb385438 | RBQ34 | 1:100 |
| VACHT | Synaptic Systems | 139 03 | 2-44 | 1:500 |
| Collagen type I antibody | Rockland | 600-401-103-0.1 | 40681 | 1:500 |
| Recombinant Anti-Ku80 antibody [EPR3468] | Abcam | GR3216586-3 | ab80592 | 1:300 |

Table 2- Primary antibodies used for immunofluorescence analysis. Dilution rates refer to the original antibody or dye solution diluted in BSA 2%.

| Secondary antibody/marked toxins/dyes | Company | Catalog number | Lot number | Dilution rate |
|---|---------------|----------------|------------|---------------|
| Donkey anti-Rabbit IgG (H+L) Highly Cross-Adsorbed Secondary Antibody, Alexa Fluor™ 488 | Thermo Fisher | A-21206 | 176375 | 1:500 |
| Donkey anti-Rabbit IgG (H+L) Highly Cross-Adsorbed Secondary Antibody, Alexa Fluor™ 488 | Thermo Fisher | A-21206 | 176375 | 1:500 |
| Goat anti-Rabbit IgG (H+L) Cross-Adsorbed ReadyProbes™ Secondary Antibody, Alexa Fluor 594 | Thermo Fisher | R37117 | 1875978 | 1:500 |
| F(ab') ₂ -Goat anti-Rabbit IgG (H+L) Cross-Adsorbed Secondary Antibody, Alexa Fluor™ 647 | Thermo Fisher | A-21246 | 55002A | 1:500 |
| Goat anti-Mouse IgG (H+L) Highly Cross-Adsorbed Secondary Antibody, Alexa Fluor™ 555 | Thermo Fisher | A-21424 | 1802436 | 1:500 |
| Goat anti-Mouse IgG (H+L) Cross-Adsorbed Secondary Antibody, Alexa Fluor™ 488 | Thermo Fisher | A-11001 | 1834337 | 1:500 |
| α-Bungarotoxin, Alexa Fluor™ 488 conjugate | Thermo Fisher | B13422 | 1750294 | 1:500 |
| α-Bungarotoxin, Alexa Fluor™ 555 conjugate | Thermo Fisher | B35451 | 1880574 | 1:500 |
| Alexa Fluor™ 555 Phalloidin | Thermo Fisher | A34055 | 1780358 | 1:500 |
| DAPI | Sigma Aldrich | D9542 | 28114320 | 1:1000 |

Table 3- Secondary antibodies used for immunofluorescence analysis. Dilution rates refer to the original antibody or dye solution diluted in BSA 2%.

3.4 Tissue clearing and whole mount immunofluorescence

The protocol used for skeletal muscles tissue clearing is the one already described by Williams et al. (Williams et al. 2019) and summarized in Figure 17. Briefly, freshly dissected TA muscles were incubated for less than 24 hours in freshly prepared 4% PFA (Roth) solution (in 1X PBS) and then transferred overnight in one 50 ml tube with 0,5% Tween-20 (Sigma) 10 μ g/ml heparin (Sigma) solution (in 1X PBS) (PTwH) on a roller mixer at room temperature, to eliminate the residual PFA. The hydrogel embedding was then performed by incubating the sample with 40 ml of 4% acrylamide solution (in deionized water, as the salts contained in PBS could interfere with the gel polymerization) containing 2,5 g/l of VA-044 activator as polymerization temperature-controlled catalyst. The tube used was a dark brown light-resistant 50 ml tube, necessary as light can interfere with the polymerization. After mixing, the tubes were incubated at 4°C on a roller mixer for five days. The hydrogel solution was then degassed using the Life Canvas EasyGel system: after being subjected to -90kPa pressure, the samples were flushed with nitrogen. Then the temperature was set to 37°C and the sample incubated for 4 hours while shaking. The muscles were then retrieved from the polymerized hydrogel and placed in 2ml tubes in PTwH on a roller mixer at room temperature to remove hydrogel excess. PTwH solution was frequently changed to guarantee the elimination of undesired residual hydrogel.

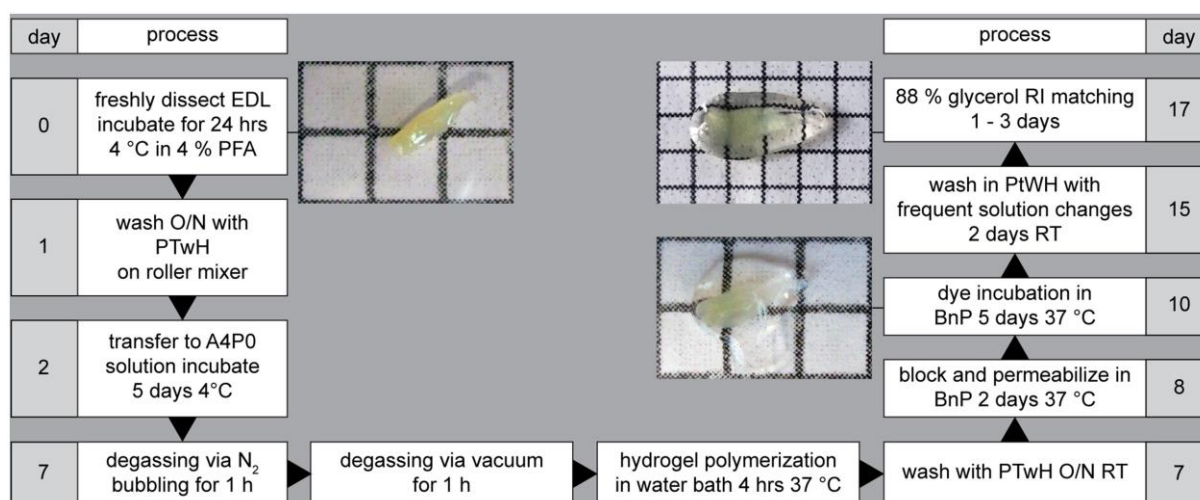


Figure 17- Scheme representing the different phases of the MYOCLEAR protocol. Hydrogel embedding phase last from day 2 to day 7, staining from day 8 to day 15, RI matching from day 16 to 17. It has to be considered that, where needed, a second washing step and dye incubation step are needed if primary and secondary antibodies are used, increasing the procedure time by 7 days.

The staining procedure of the hydrogel-embedded samples started immediately after, by incubating the sample in “Blocking and Permeabilization” solution (BnP, 10% PTwH, 0,5% Triton X-100, 1% DMSO, 6% BSA in 1X PBS) for two days. Then the samples were incubated with fresh BnP containing primary antibody solution for five days at 37°C, then washed for two days in fresh BnP and subsequently transferred in the secondary antibody/dye solution (in BnP) (for the Myosin 3 antibody, the α -Bungarotoxin Alexa Fluor™ 555 conjugate and the F(ab')₂-Goat anti-Rabbit IgG (H+L) Cross-Adsorbed Secondary Antibody,

Alexa Fluor™ 647 the dilution rates are as indicated in Table 3). The samples were then washed for two days with PTwH with frequent solution changes.

Before imaging, the samples were incubated in distilled water for one day with frequent solution changes to remove any residual detergent presence, and then subjected to R.I. matching by being incubated for three days in 88% Glycerol solution whose R.I. was matched to a value of $n=1.457$. As it was observed that an exact n was necessary (differences from the value indicated as little as 0.002 can cause the images obtained to be blurry) the 88% glycerol solution was prepared and then exactly matched at the R.I. value desired, adding distilled water or glycerol. Another detail that has to be taken in account is the temperature at which the sample is kept before imaging, as it is suggested to store the sample in the same room where the microscope that will be used for imaging is kept, to avoid any temperature changes.

3.5 Image analysis and semi-automated quantification

Confocal images obtained from muscles cryosections were processed and analyzed using ImageJ (FIJI version). From maximum projections of the images, areas which showed the presence of mIgG or collagen I or actin were manually thresholded, areas selected and measured. The entire area of the cryosection was contoured by hand using the background signal. The areas where dystrophin-outlined cells were present were obtained from maximum projected confocal images to which was applied a median filter and then thresholded. Subsequently the “analyze particles” function of ImageJ was used (selecting 20 μm as lowest value and including holes). The image obtained was then measured. Muscle fibers, center-nucleated fibers, and eMHC+ fibers were counted manually. Where myofiber cross-sectional area was measured, five patches of ten muscle fiber each were hand-contoured and their area measured for each cryosection analyzed. For each sample a minimum of three cryosections was processed and analyzed. NMJs, marked by AChR and VACHT expression, their shape and/or position with respect to muscle fibers, were analyzed and quantified manually. Signals for pre- and postsynapses obtained from three different cryosections per sample were analyzed. Details on the precise number of synapses analyzed are shown in Table 4. In order to quantify the presence of ASCs, a different analysis was performed to quantify Ku80 detection. DAPI signals corresponding to cell nuclei were thresholded and segmented. A selection created from those signals was then used to hand-segment the Ku80-positive signal, selecting those areas where it was colocalizing within the cell nuclei.

| Days post injection | No ASCs | | ASCs | |
|---------------------|--------------------------------|---------------------------------|-------------------------------|--------------------------------|
| | Glycerol | Saline | Glycerol | Saline |
| 3 | 46.25 \pm 4.33; 185 (n=4) | 78.0 \pm 20.6; 312 (n=4) | 36.3 \pm 13.1; 101 (n=3) | 71.5 \pm 11.79; 213 (n=3) |
| 5 | 67.3 \pm 24.4; 202 (n=3) | 94.3 \pm 15.7; 283 (n=3) | 88.5 \pm 17.2; 254 (n=3) | 76.0 \pm 3.9; 232 (n=3) |
| 8 | 59.3 \pm 10.7; 178 (n=3) | 79.33 \pm 17.42; 238 (n=3) | - | - |
| 11 | 44.3 \pm 15.8; 133 (n=3) | 119.7 \pm 19.2; 359 (n=3) | 85.0 \pm 8.1; 255 (n=3) | 79.66 \pm 7.17; 239 (n=3) |

Table 4- Number of NMJs per experimental condition. Shown is mean \pm SEM per muscle; number of NMJs found in total per condition (n indicates number of analyzed muscles per condition).

3.6 Statistical analysis and figures

For statistical analysis, data were first screened for normality and homoscedasticity using Kolmogorov-Smirnov test and F-test. Mean and SD/SEM were calculated. Then, significance was assessed with Student's t-test or Welch test. Data compilation was done in Microsoft Excel for Mac, plots were made using either Microsoft Excel for Mac or Graph Pad Prism. Figures were prepared in Adobe Photoshop and then compiled in Adobe Illustrator.

4. Results

4.1 Glycerol injection leads to early necrosis and robust regeneration

In order to observe the effects of glycerol injection in the *tibialis anterior* (TA) muscle, 20 μ l of 50% glycerol (in saline solution) or saline (injected contralaterally as a sham procedure) were administered intramuscularly. The muscles were then harvested 18 hours, three, five, eight and eleven days after the procedure. Cryosections obtained from those muscles were then stained for different markers to study the muscle response to injury. Several parameters were evaluated to quantify how glycerol injection affects muscle degeneration and recovery. Firstly, necrosis and fibrosis were considered as they typically appear upon muscle injury. To evaluate muscle necrosis and general inflammatory state we observed the percentage of the area positive for mouse immunoglobulin type G (mIgG). While in healthy muscle, mIgG is normally located only in blood vessels and in the interstitial space, the compromised plasma membrane of damaged myofibers is expected to let serum proteins to be taken up into the cytosol (Iwata, Suzuki, and Wakabayashi 2013; Judson et al. 2013; Proto et al. 2015; Arecco et al. 2016; Rodrigues et al. 2016). Thus, while in healthy muscles the signal for mIgG was expected to be weak and concentrated mostly in blood vessels and interstitial space, damaged muscles were expected to show the presence of necrotic myofibers, whose cytosolic space should be positive for mIgG. For the same reason, those fibers should be subjected to leakage, losing f-actin from their cytosol. F-actin is the most abundant actin in myofibers (Prochniewicz Nakayama, Yanagida, and Oosawa 1983; Gokhin and Fowler 2011; Demonbreun et al. 2016) and is critical to myofiber functionality. Its presence was detected exploiting the ability of phalloidin toxin to bind it (Allen et al. 1996), so a fluorophore-marked phalloidin was used. Muscle fibrosis, one of the early phenomena appearing upon muscle damage (Tedesco, F. S., Dellavalle, A., Diaz-Manera, J., Messina, G., & Cossu 2010; Garg, Corona, and Walters 2015; Webster et al. 2015) was evaluated by measuring the area that marked positive for the presence of collagen type I. Collagen type I is one of the most abundant protein in muscle extra-cellular matrix (ECM) (Huebner et al. 2008; Serrano and Muñoz-Cánoves 2010; Gillies and Lieber 2011; Feng et al. 2019). Together with those markers, also the presence of dystrophin was monitored, as it is a key element of the dystrophin-associated glycoprotein complex (DGC) and acts as a link between the cytoskeleton and the ECM. Its functionality ensures the coordination between those two muscle tissue elements and avoids the contraction-induced muscle damage (Biral et al. 2000). After immunostaining for mIgG, collagen I, dystrophin and eMHC (along with the marking of f-actin through phalloidin) confocal analysis of the TAs cryosections was performed. After 18 hours from the injection, glycerol-injected muscles showed extensive damage, characterized by f-actin leakage and serum protein uptake as shown in Figure 18. Along with the loss of dystrophin, those parameters indicate a compromised cell membrane and overall loss of function in the areas affected. Moreover, cell nuclei not belonging to muscle fibers were observed in the areas affected by glycerol-induced injury, suggesting a cell infiltration. That

resembles what happens after an injury to the skeletal muscle, with fibroblast and monocyte presence in the damaged site (Tidball 2005; Tidball and Villalta 2010; Mahdy 2018).

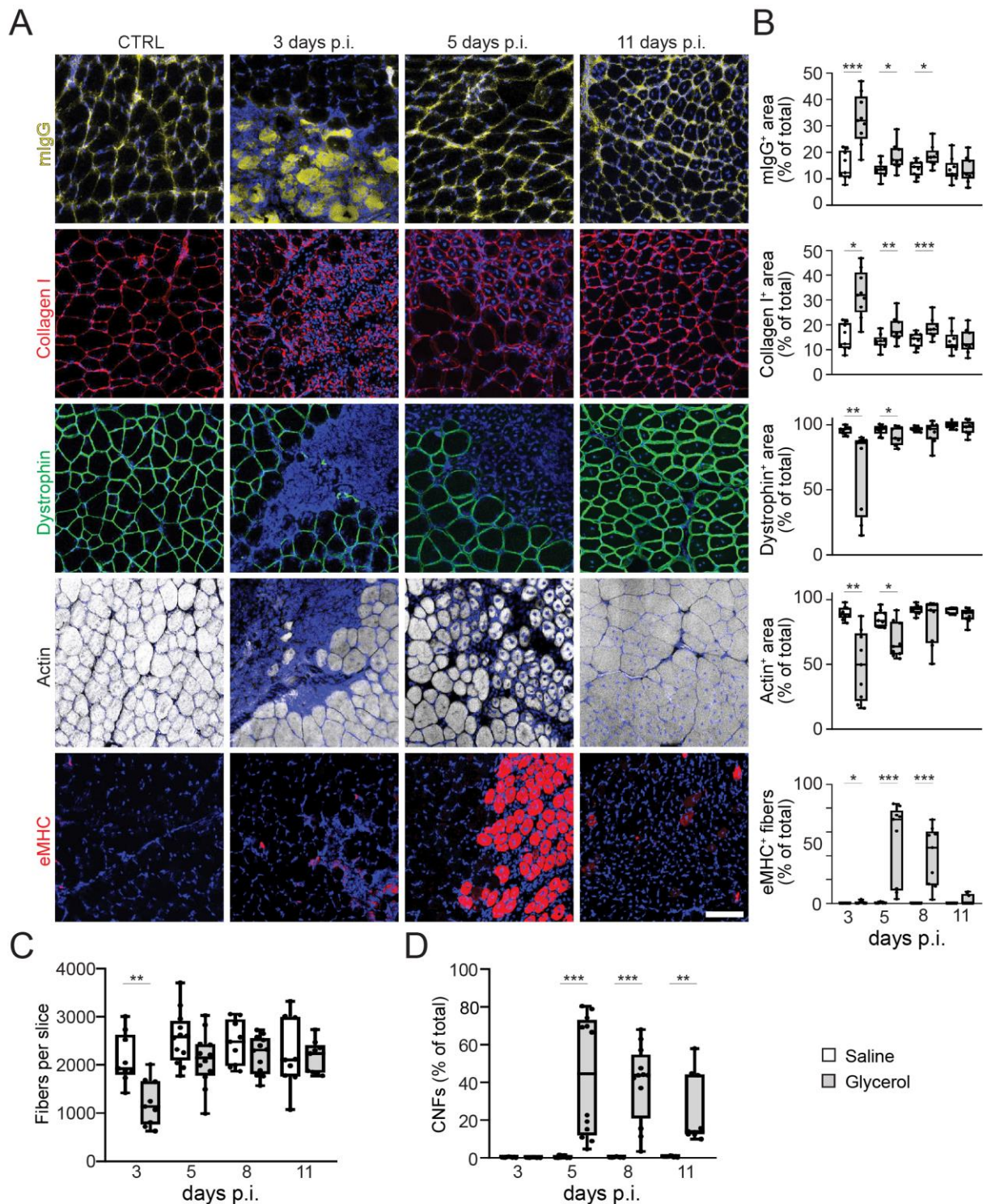


Figure 18- Glycerol induced muscle damage is characterized by necrosis and loss of dystrophin and actin, followed by a transient expression of eMHC and the increase in center-nucleated fibers. Representative optical sections of fluorescent signals as indicated (A), nuclear DAPI staining always shown in blue, mIgG in yellow, collagen I and eMHC in red, dystrophin in green, actin in grey. CTRL indicates muscle injected with saline three days post-injection, while the other panels show TA sections at three, five and eleven days after

glycerol treatment. (B) Quantitative analysis of section areas positive for fluorescence signals of either mIgG, collagen I, dystrophin, or actin, or number of eMHC-positive fibers, as a function of days p.i. Box-Whisker plots show all individual data points as dots, the extensions of upper and lower quartiles in the boxes, the medians as horizontal lines in the boxes, and maxima and minima as whiskers. * $p \leq 0.05$, ** $p \leq 0.01$, *** $p \leq 0.001$. (C-D) Quantitative analysis of fibers per muscle slice (C) or center-nucleated fibers (% of fiber number, D) as a function of days p.i. Box-Whisker plots show all individual data points as dots, the extensions of upper and lower quartiles in the boxes, the medians as horizontal lines in the boxes, and maxima and minima as whiskers. ** $p \leq 0.01$, *** $p \leq 0.001$. Scale bar: 100 μm

TA muscles dissected three, five, eight and eleven days after glycerol (or saline) injection were considered for the quantification of muscle damage and regeneration markers, as shown in Figure 18. Three days after the treatment, large areas of the muscle were interested by immunoglobulin infiltration, presence of necrotic myofibers, accumulation of fibrotic tissue and loss of functional markers as phalloidin and dystrophin, resembling closely an injured status already observed 18 hours after injection (Figure 19).

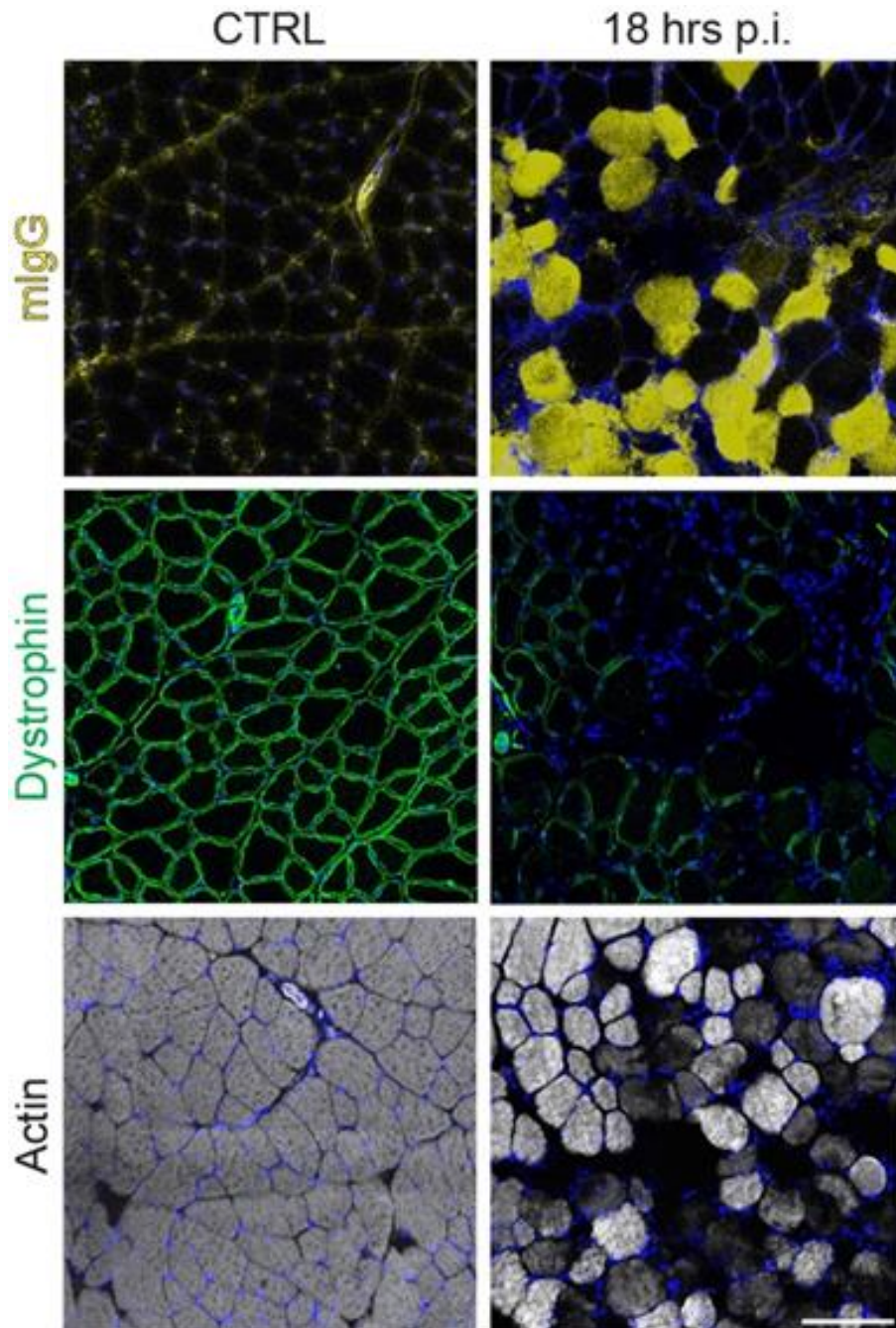


Figure 19- Glycerol injection leads to structural damage to muscle fibers within 18 hours from the treatment. After either glycerol or saline solution injection, TA muscles were harvested 18 hours after the treatment and snap-frozen. Subsequently, cryosections were obtained and stained with mouse immunoglobulin G antibody, phalloidin (both coupled with a fluorophore) and anti-dystrophin antibody. Treated muscles (18 hrs p.i., on the right) show serum proteins uptake (mIgG) in the cytosolic space, indicating necrosis, along with loss of dystrophin and actin respect to the contralateral muscles (CTRL, on the left). Scale bar: 100 μ m.

Moreover, the number of muscle fibers was significantly decreased (Figure 18C). In the following timepoints, five, eight and eleven days after the injection, these signs of muscle damage decreased and regeneration markers started to appear: between five and eight days post-injection a wave of eMHC expression was observed, along with a significant increase in CNFs and the return of the muscle fibers number back to the one counted in saline-injected samples. Both eMHC⁺ and CNFs fibers were present until eleven days after the injection,

while damage-related parameters returned to normal levels. This indicated that within eleven days from the treatment, although a strong initial damage with necrosis, fibrosis and loss of functional proteins, the muscle was able to regenerate efficiently. The remaining muscle fibers cross sectional area (CSA) was measured in order to detect any kind of change in the myofiber size (Table 5). No significant difference between the control and the glycerol-treated samples was detected at any timepoint, suggesting that the fibers surviving the glycerol treatment were not subjected to any shrinking or swelling.

| Days post injection | CSA | |
|---------------------|------------------|----------------|
| | Saline (control) | Glycerol |
| 3 | 2010.5 ± 104.8 | 2136.5 ± 164.4 |
| 5 | 1885.6 ± 290.3 | 1969.0 ± 312.1 |
| 11 | 1934.6 ± 122.1 | 1963.1 ± 218.2 |

Table 5- Cross-sectional area per fiber in μm^2 per experimental condition. Shown is mean \pm SEM (n=3 mice). None of the values differed significantly from any other.

Notably, as shown in Figure 20, the damage was not homogenous, probably due to the low volume of glycerol used. Both, damage-related (mIgG and collagen I presence and absence of actin and dystrophin) as well as regeneration-associated markers (eMHC) were localized in distinctive areas. After having characterized how a low-dose glycerol injection affects muscle destruction and subsequent recovery, the focus moved towards analyzing pre- and postsynaptic regions in order to characterize NMJ degeneration and regeneration.

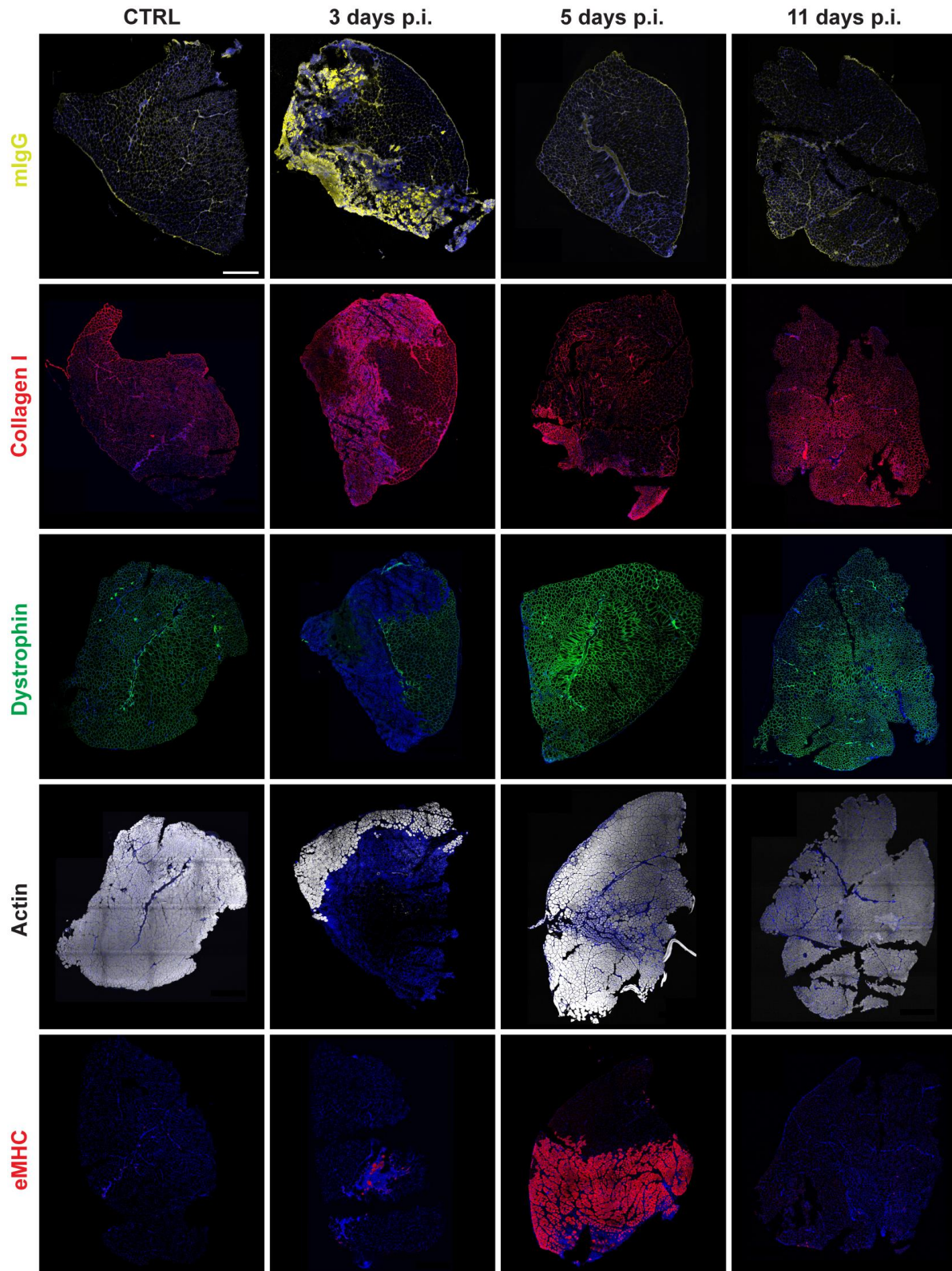


Figure 20- Glycerol induced muscle damage is characterized by necrosis and loss of dystrophin and actin, followed by a transient expression of eMHC and the increase in center-nucleated fibers. Representative optical sections of fluorescent signals as indicated, nuclear DAPI staining always shown in blue, mIgG in yellow, collagen I and eMHC in red, dystrophin in green, actin in grey. CTRL indicates muscle injected with saline three days post-injection, while the other panels show TA sections at three, five and eleven days after glycerol treatment. Scale bar: 500 μ m

4.2 Glycerol injection leads to transient loss of presynapses

In order to characterize the effect of glycerol-induced muscle damage on NMJs, TA muscles were injected with 50% glycerol solution or saline and samples were taken three, five, eight and eleven days after the injections. Cryosections were stained against nicotinic acetylcholine receptors (AChR) using fluorescent α BGT in order to identify postsynapses. Presynapses were analyzed by investigating the presence of vesicular acetylcholine transporter (VACHT), using anti-VACHT immunofluorescence staining. Analysis at the confocal microscope of treated samples showed that AChR+ signals were present at all time-points, indicating that the presence of postsynapses was largely retained throughout the entire experiment. On the other hand, many of the sites identified by AChR+ signals were negative for VACHT at three, five and eight days after glycerol injection. Further analysis showed that in glycerol-treated muscles the number of AChR+ sites was slightly, but not significantly, reduced compared to the ones counted in the muscles injected with saline. The only exception was at eleven days after the injection, where the number of postsynapses detected in the control was significantly higher than the one obtained from the treated muscles.

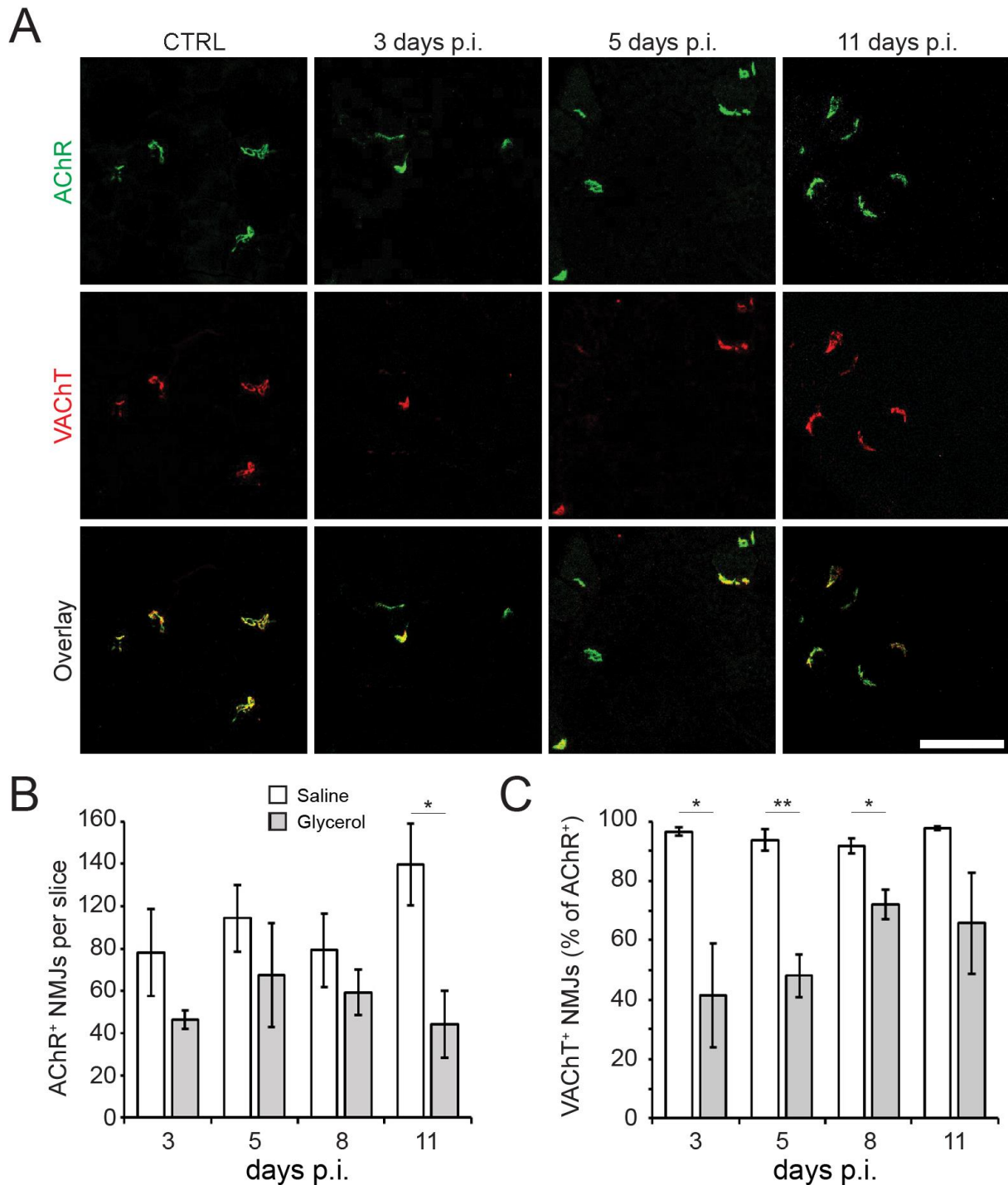


Figure 21-Glycerol treatment affects differently pre- and postsynapses. Representative images of the localization of AChR (in green) and VAcHT (in red) and their overlay in TA muscle cross section (A) at different timepoints (The sham procedure three days after the injection indicated as sham, the other timepoints as in the amount of days post-injection (p.i.)). Scale bar: 100 μ m. Quantitative analysis of AChR+ sites (B) present per cryosection and percentage of how many of them were positive for VAcHT as well (C). Shown is mean \pm SEM (n = 3 muscles). * $p \leq 0.05$, ** $p \leq 0.01$.

Although some features of the NMJs, such as volume and fragmentation, cannot be evaluated effectively from cryosections, a measure of the area of the post-synaptic sites was conducted. This showed that the measured postsynaptic sites areas were not altered by condition or day after treatment (Table 6).

| Days post injection | Saline | Glycerol |
|---------------------|--------------|--------------|
| 3 | 122.6 ± 38.6 | 203.5 ± 26.4 |
| 5 | 158.0 ± 33.7 | 180.3 ± 33.8 |
| 11 | 184.7 ± 20.3 | 158.2 ± 42.4 |

Table 6- Areas of NMJs in μm^2 per experimental condition. Shown is mean \pm SEM (n=3). None of the values differed significantly from any other.

As previously indicated, AChR+ sites were analyzed regarding the presence of VAcHT as well, in order to quantify how many of the postsynapses detected presented also a signal associated with a presynaptic marker, and so could be assumed to indicate a functional NMJ. AChR-positive and VAcHT-positive synapses were significantly less abundant in the glycerol-treated muscles three, five and eight days after the injection respect to the sham. (Figure 21C). Notably, postsynaptic but not presynaptic sites appeared also in areas that presented severe necrosis (Figure 22).

These results show that glycerol lead to a reduction in the number of the postsynapses, that became significantly reduced at a latter timepoint (11 days p.i.) respect to the one measured in the muscle subjected to the sham. Moreover, the presynapses showed to be more sensitive to the glycerol treatment, showing a significant reduction respect to the control three, five and eight days after the injection. Overall, these results indicate that glycerol has a more detrimental effect on the presynapse than on the postsynapse. Although, while the former shows a recovering trend, the diminished number of the latter at eleven days after the treatment suggest that some postsynapses undergo to degradation several days after the muscle was subjected to the damage.

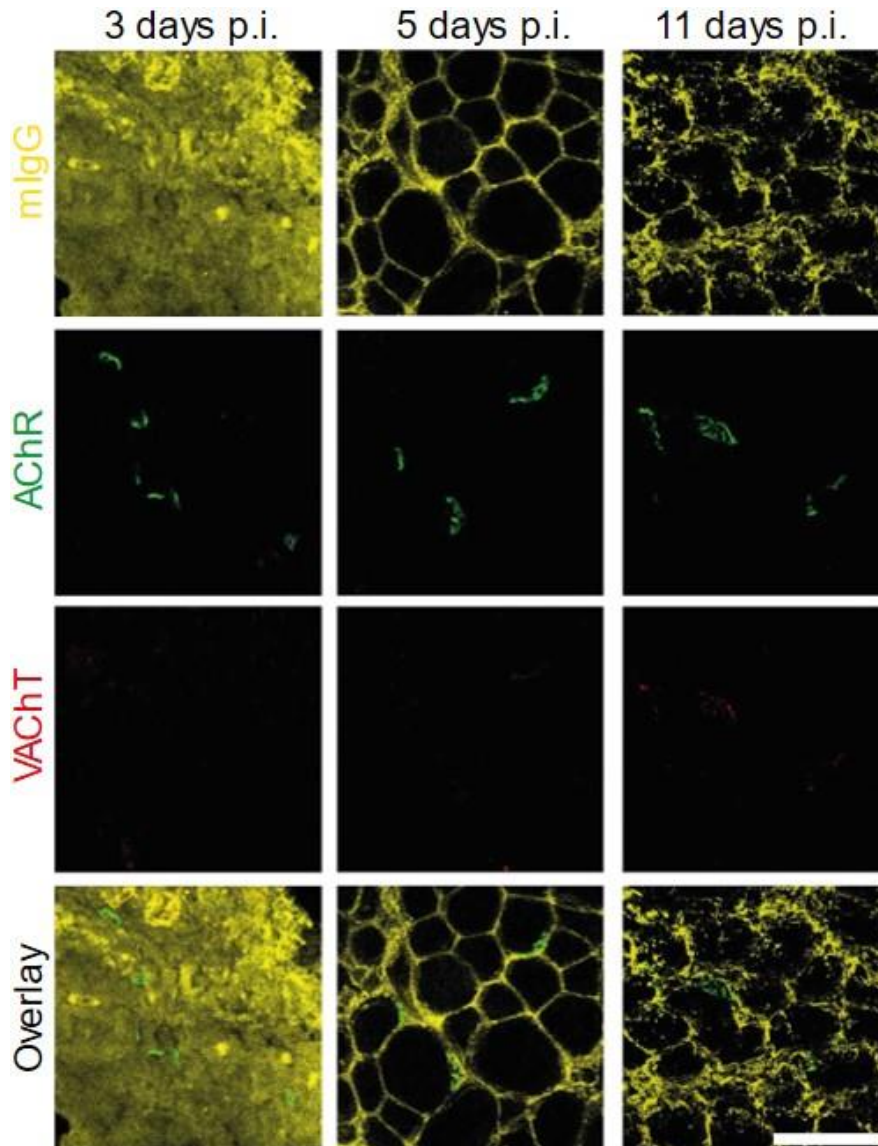


Figure 22- AChR+ VAcHT- sites were identified in highly necrotic areas as well as in unaffected regions. Representative images AChR+ VAcHT- NMJs. mIgG (in yellow), AChR (in green) and VAcHT (in red) and their overlay in TA muscle cross section at different timepoints (indicated as in the amount of days post-injection (p.i.)). Postsynaptic sites were conserved in necrotic areas of the muscle as well as in those regions not interested by fiber disruption or inflammation. At the same time, VAcHT absence was registered as well. Scale bar: 100 μ m

4.3 Glycerol-induced muscle degeneration and recovery are altered by adipose-derived stem cells (ASCs)

A further goal of this dissertation is to address the effect of stem cells, ASCs in particular, on muscle recovery after an insult. In order to do so, few minutes after intra-muscle injection of either saline or glycerol solution, ASCs were administered systemically via tail vein. Then, the same analysis performed for the characterization of the damage model were repeated on TAs cryosections harvested at three, five and eleven days after the injection. While the findings on the number of myofibers and on dystrophin and f-actin distribution resembled those obtained from samples not treated with ASCs (Figure 23), the data regarding mIgG,

collagen I, eMHC presence and the number of CNFs proved to be interestingly different from those collected from muscle treated only with glycerol (Figure 23, A-B). mIgG ad collagen I significantly increased at eleven days after the injection, while in the damage model at this timepoint their presence was comparable to the one detected in the controls.

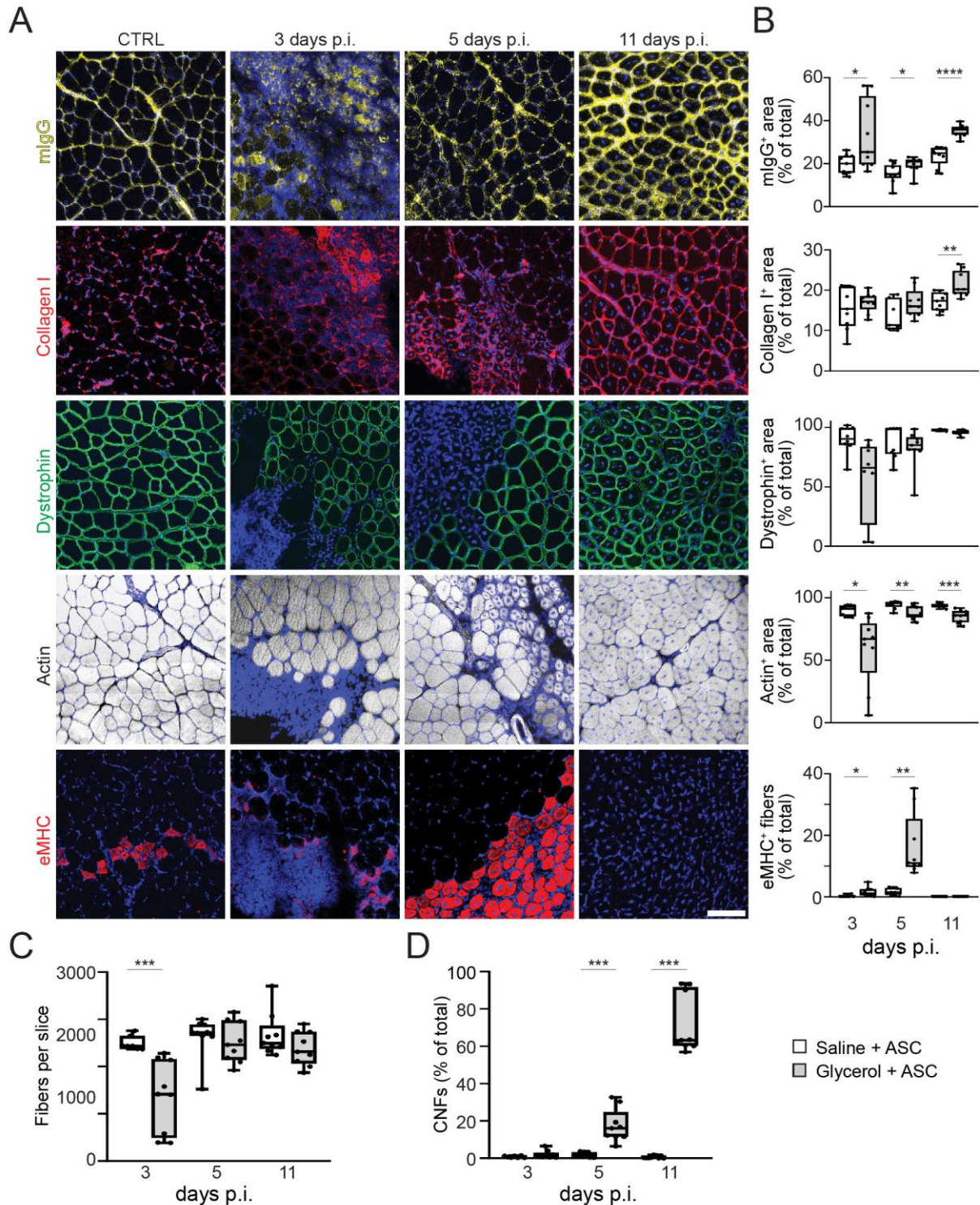


Figure 23- ASCs systemic application leads to mIgG infiltration, enhanced eMHC basal expression and increase in the center-nucleated fibers. Representative optical sections of fluorescent signals as indicated (A), nuclear DAPI staining always shown in blue, mIgG in yellow, collagen I and eMHC in red, dystrophin in green,

actin in grey. CTRL indicates muscle injected with saline three days post-injection, while the other panels show TA sections at three, five and eleven days after glycerol treatment. (B) Quantitative analysis of section areas positive for fluorescence signals of either mIgG, collagen I, dystrophin, or actin, or number of eMHC-positive fibers, as a function of days p.i. Box-Whisker plots show all individual data points as dots, the extensions of upper and lower quartiles in the boxes, the medians as horizontal lines in the boxes, and maxima and minima as whiskers. * $p \leq 0.05$, ** $p \leq 0.01$, *** $p \leq 0.001$. (C-D) Quantitative analysis of fibers per muscle slice (C) or center-nucleated fibers (% of fiber number, D) as a function of days p.i. Box-Whisker plots show all individual data points as dots, the extensions of upper and lower quartiles in the boxes, the medians as horizontal lines in the boxes, and maxima and minima as whiskers. ** $p \leq 0.01$, *** $p \leq 0.001$. Scale bar: 100 μ m

As for the glycerol-induced muscle damage model, a measure of the myofiber CSA was performed (Table 7). The CSA did not change between the different days or condition, and no significant differences between the values was detected when compared to the measures on the damage model without stem cell application.

| Days post injection | CSA | |
|---------------------|-------------------------|--------------------|
| | Saline + ASCs (control) | Glycerol + ASCs |
| 3 | 1852.4 \pm 64.6 | 2028.0 \pm 209.5 |
| 5 | 2234.0 \pm 129.6 | 2075.5 \pm 145.1 |
| 11 | 1836.1 \pm 132.5 | 1651.3 \pm 59.2 |

Table 7- Cross-sectional area per fiber in μm^2 per experimental condition. Shown is mean \pm SEM (n=3 mice). None of the values differed significantly from any other.

Notably, mIgG were identified in the extracellular space, indicating more likely an inflammatory state of the tissue than the presence of necrotic fibers, whose presence was not detected at that timepoint. Also, in terms of fibrosis, instead of detecting the deposition of scar tissue in specific areas as seen in the damage model, the increase in collagen I was located mostly along the borders of the muscle fibers. The presence of collagen I in such areas could be indicative of a more systemic inflammatory state, instead of a fibrotic area with large deposition of scar tissue as observed in the absence of ASC. Together with the data obtained from the staining for mIgG presence, this can indicate the presence of a late-phase inflammatory status of the muscle. eMHC expression, although following a similar trend to the one observed in the damage model, was present also in the saline controls when stem cells were applied. Moreover, in the animals treated with glycerol and ASCs the percentage of center-nucleated fibers rose over time up to 71.4% \pm 15.8% (mean \pm SEM, n=3 samples) eleven days after the injection, while in the corresponding saline controls it remained at basal levels (0.6 % \pm 0.7 %, mean \pm SEM, n = 3 samples). These results lead to two observations: First, ASC application induces a late-phase inflammatory phase, as shown by the increased levels of mIgG and collagen I, indicating serum protein increase in the extracellular space and fibrosis respectively. Second, ASCs can enhance the regenerative process, leading to a prolonged muscle recovery phase, as shown by the high amount of CNFs and by the expression of eMHC in the controls where ASCs were applied. So, while a secondary inflammation, although limited and not indicating a severe damage condition as the one

observed three days after the treatment, is not desirable, a prolonged regenerative phase is a promising sign for the possible therapeutic application of ASCs for muscle damage treatment.

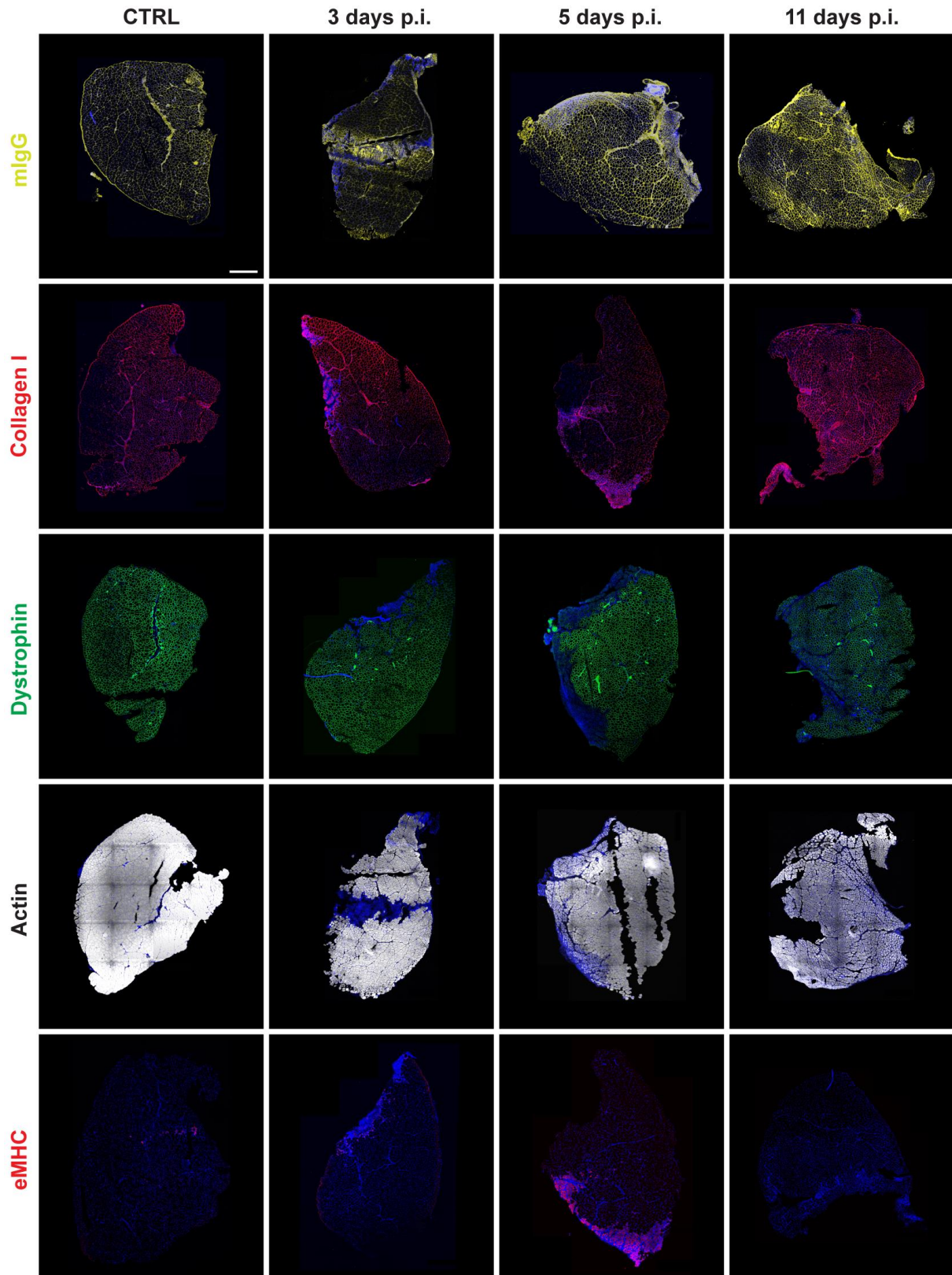


Figure 24- ASCs systemic application leads to mIgG infiltration, enhanced eMHC basal expression and increase in the center-nucleated fibers. Representative optical sections of fluorescent signals as indicated (A),

nuclear DAPI staining always shown in blue, mIgG in yellow, collagen I and eMHC in red, dystrophin in green, actin in grey. CTRL indicates muscle injected with saline three days post-injection, while the other panels show TA sections at three, five and eleven days after glycerol treatment. Scale bar: 500 μ m

4.4 Adipose-derived mesenchymal stem cells (ASCs) treatment reduces the loss of presynapses in the glycerol damage model

Next, the effects of ASCs in the kinetics of loss and recovery of NMJs were quantified. TA muscles cryosections from the animals treated with ASCs and then injected with glycerol or saline solution were investigated for the presence of AChR and VACHT and analyzed by confocal microscopy.

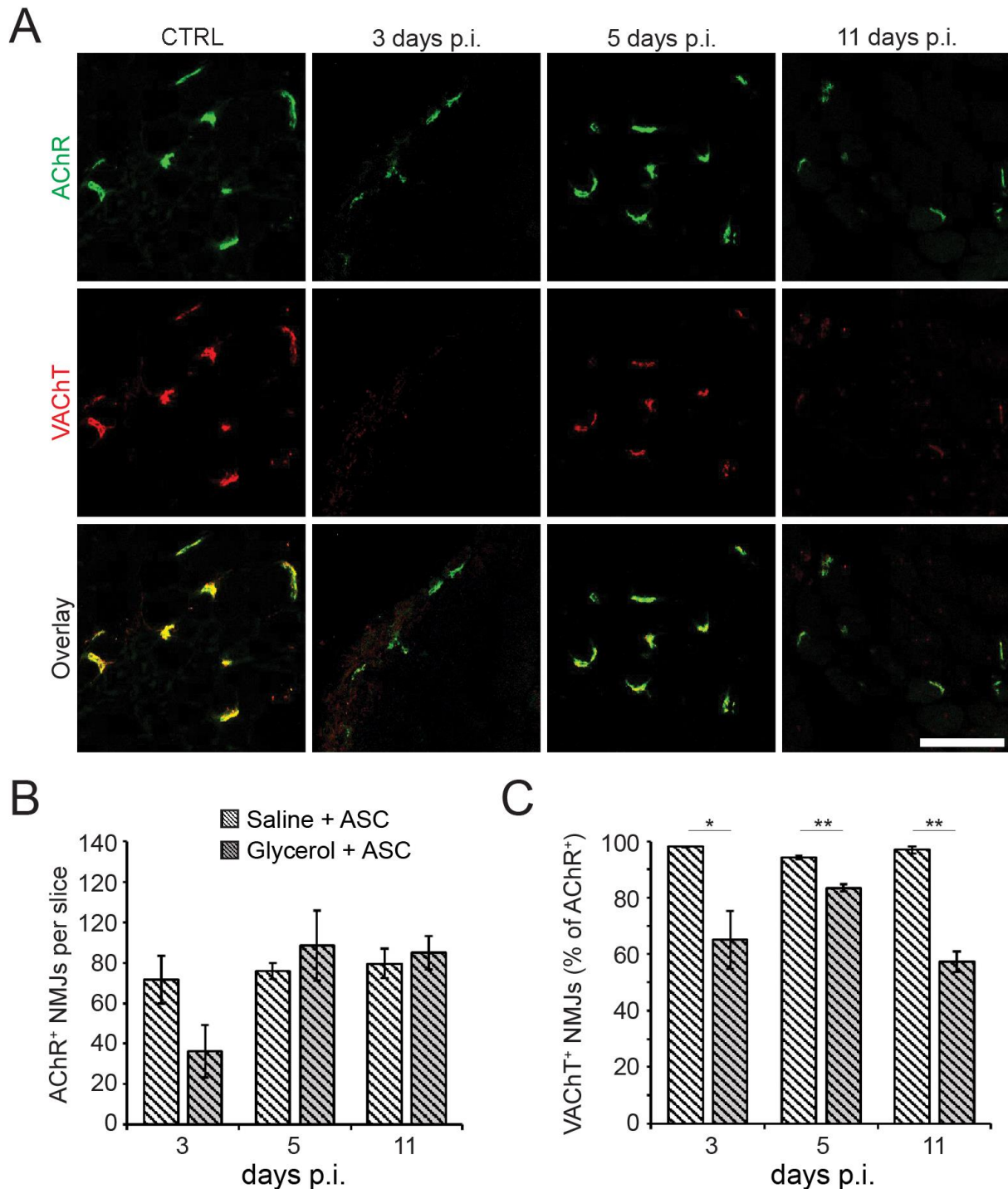


Figure 25- ASCs enhance recovery of presynapses at early stages, but such effect is not present at late time point. As soon as TA muscles were injected with either saline or 50% glycerol solution, mice were injected via tail-vein with ASCs. TA muscles were then harvested and immediately snap-frozen three, five or eleven days after the injection (days p.i.). After cryosectioning, muscle sections were stained with α BGT (marking AChR) and antibodies against VAcHT to label post- and presynaptic portions of NMJs, respectively. Cryosections were then analyzed with confocal microscopy. (A) Representative images of fluorescence signals as indicated, AChR in green, VAcHT in red, in overlay images yellow indicates the colocalization of both signals. Saline-injected muscles at 3 days p.i. indicated as CTRL, while the other panels show representative images from glycerol-injected muscles at three, five, and eleven days post-injection. Scale bar: 100 μ m. (B-C) Quantitative analysis of AChR+ post-synaptic sites present per section (B) and of VAcHT+ NMJs (as percentage of VAcHT+ structure, C) as a function of days after the treatment. Shown is mean \pm SEM (n = 3 muscles). * p \leq 0.05, ** p \leq 0.01.

The quantification of AChR+ sites did not show any difference between glycerol and saline injected muscles (Figure 25, B), though a reduction (not significant) of postsynapses was observed in glycerol treated muscles. Quantification of AChR+/VAcHT+ sites showed an improved recovery at three and five days after the injection respect to the samples were ASCs were not applied. At those timepoints, the amount of AChR+/VAcHT+ NMJs detected in glycerol treated muscles was $41.4\% \pm 17.3\%$ and $48.1\% \pm 7.2\%$ (mean \pm SEM, n = 3 muscles) at three and five days post-injection respectively, while where ASCs were applied they reached $65.1\% \pm 10.3\%$ and $83.4\% \pm 1.3\%$ (mean \pm SEM, n = 3 muscles) at the same timepoints. On the other hand, these seemingly better regeneration was proven to be only temporary, as the values dropped to $57.3\% \pm 3.7\%$ (mean \pm SEM, n = 3 muscles) eleven days after the treatment with glycerol and ASCs instead of showing further recovery as it was observed in animals were only the damage procedure was applied ($65.8\% \pm 16.9\%$ (mean \pm SEM, n = 3 muscles) AChR+/VAcHT+ sites on day eleven).

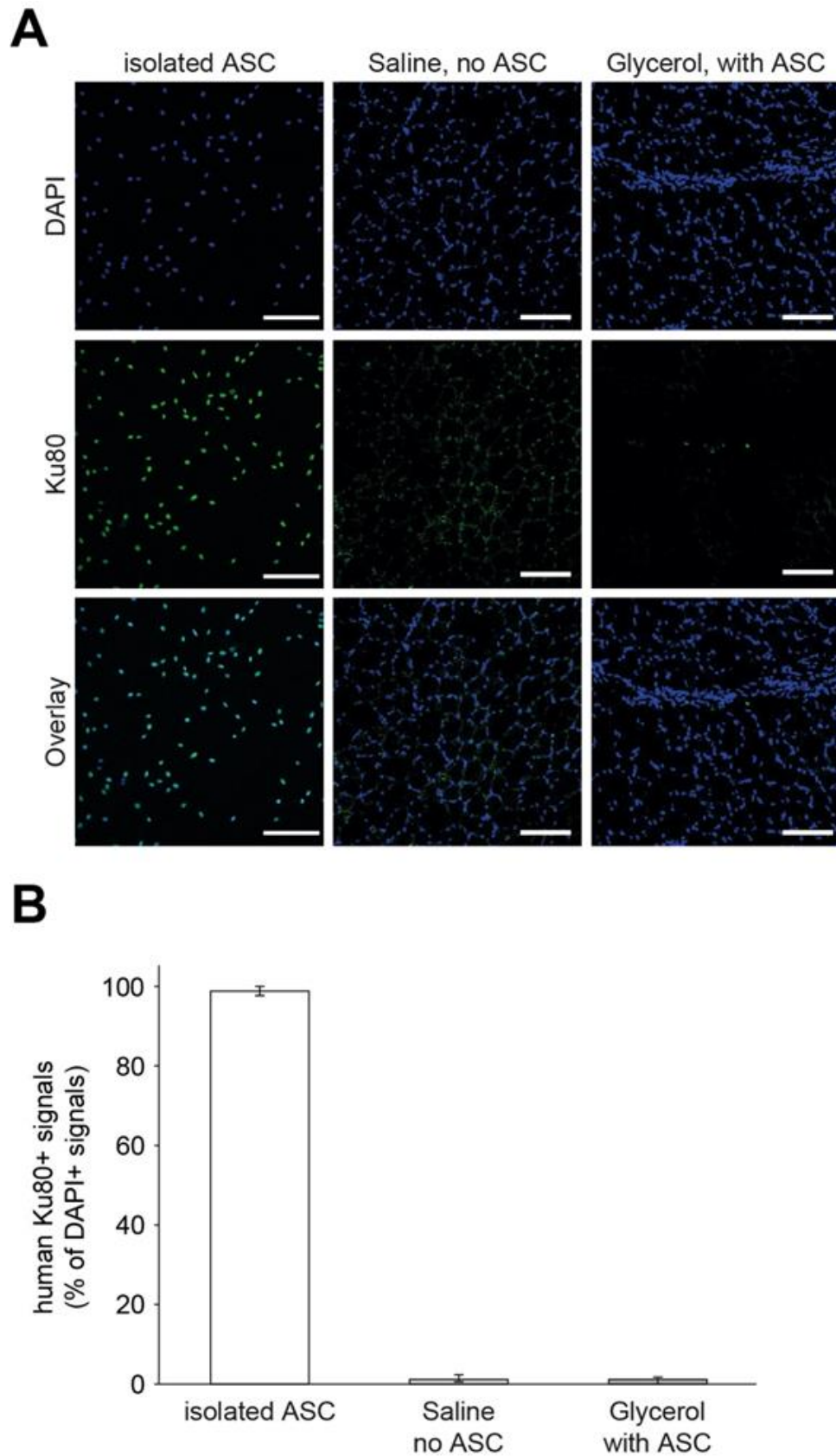


Figure 26-Integration of systemically injected ASC into muscle is not detectable by immunofluorescence. Isolated human ASC and mouse TA muscle sections taken five days post injection of either saline or glycerol (indicated) were stained with DAPI and an anti-human Ku80 antibody against DNA and human nuclei, respectively. (A) Representative confocal micrographs showing fluorescence signals of DAPI and human Ku80 in blue and green, respectively. (B) Quantitative analysis of the percentage of human Ku80+ signals found in DAPI+ nuclei.

Subsequently, the possible presence of ASCs was investigated within the muscles treated, to verify if their effect on the muscle and the NMJs was to be ascribed to their local presence or to indirect effects. In order to do that, ASCs in culture, and control muscles 5 days after the glycerol treatment (with or without the stem cell application) were stained for the detection of Ku80, a nuclear marker for hASCs (Koike et al. 1999). While in the ASCs the presence of Ku80+ cell nuclei was evident (Figure 26A), in the muscles such signals were absent. Moreover, when quantified (Figure 26B) the amount of Ku80+ cell nuclei present in the muscle not treated with ASCs was comparable to the values measured in the samples that were subjected to stem cell application. It has to be noted that, since ASCs were injected systemically, any effect linked to their human origin should be normalized when compared to the controls. In summary, systemic treatment with ASCs resulted in a transiently better recovery of the damaged skeletal muscle after the glycerol injection. However, these beneficial effects lasted only for the early timepoints (three and five days after the injection), as the number of functional sites at eleven days after the injection was comparable to the one measured in the muscles where only the damage was induced, without any stem cell infusion. Such beneficial, although temporary, effects on muscle regeneration cannot be ascribed to a direct effect of ASCs on skeletal muscle, as their presence was not detected at any of the timepoints considered. On the other hand, another theory could be that ASCs can exert their influence of muscle regeneration by a “long-range” mechanism, through the secretion of anti-inflammatory substances as IL-6 (Wu et al. 2017). Such chemical species have been proven to promote an anti-inflammatory state (Belizário et al. 2016) that could explain the decrease in fibrosis and mIgG presence detected along with a more prominent muscle regeneration registered at 11 days p.i. Both those effect could be a direct consequence of a M2 macrophage activation, promoted in fact by molecules as IL-6 (Mahdy 2018). Although fascinating, such hypothesis would require further investigation both regarding the presence of specific molecules within the recovering muscle tissue and the macrophage activation.

4.5 Tissue clearing for postsynapse structure and embryonic myosin heavy chain (eMHC) expression

In order to investigate the postsynaptic structure preservation and eMHC expression in the glycerol damaged muscle, one glycerol-injected and one saline-injected TAs were dissected five days after the treatment and subjected to the MYOCLEAR tissue clearing procedure. Afterwards, whole-mount scan of the two muscles were performed in order to study the expression of eMHC in 3D and to investigate the postsynaptic structure in detail. In the control, as shown in Figure 27, the results obtained showed an overall conserved muscle fibers structure together with the presence of NMJs presenting the classical pretzel-shaped structure. eMHC expression was absent, with the only few signals detected to be ascribed to secondary antibody residue.

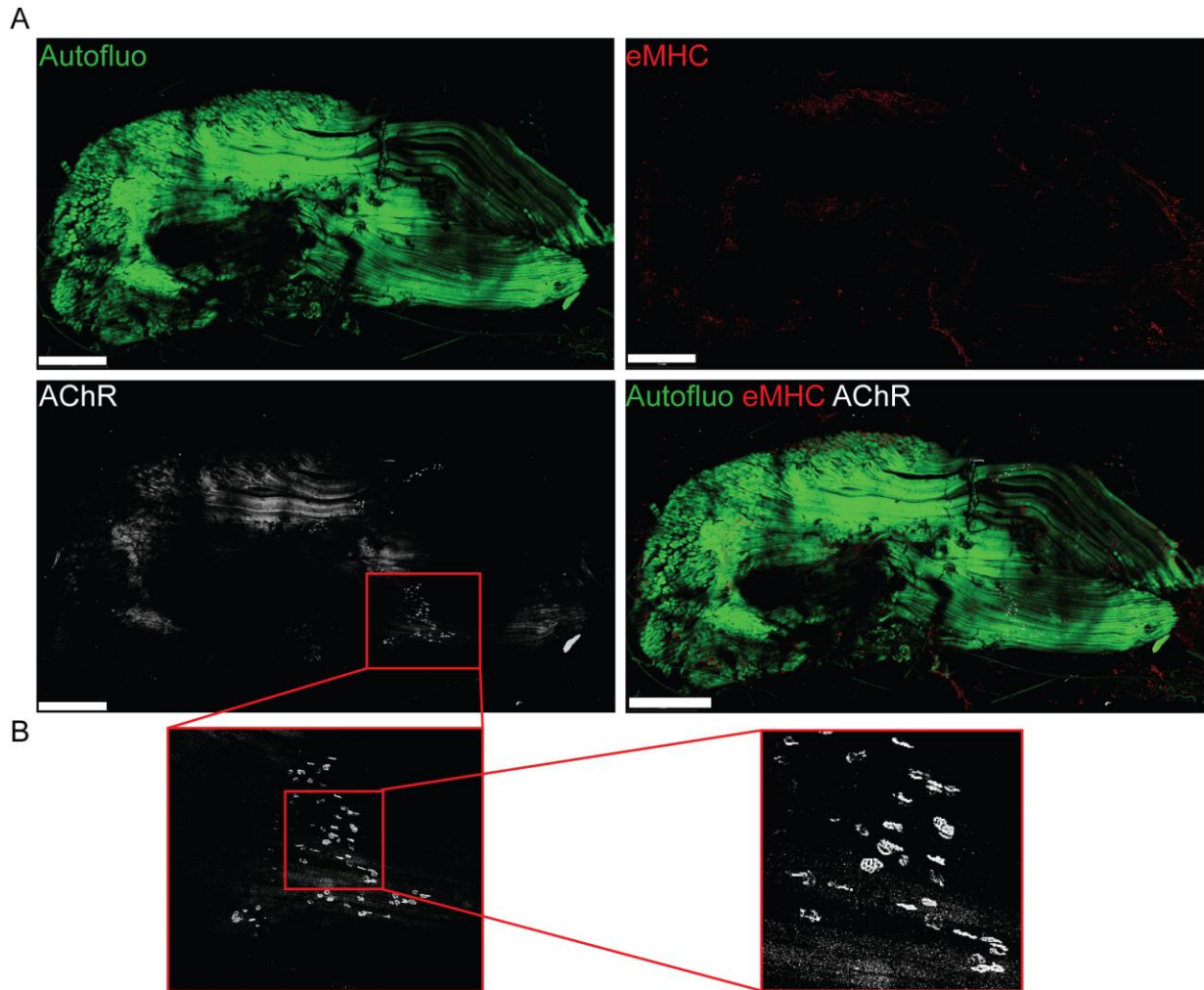


Figure 27- eMHC is not present in saline-injected muscles and postsynaptic structure is preserved. Five days after saline injection, TA muscle was dissected and cleared using the MYOCLEAR procedure and then immunostained with anti-eMHC antibody (subsequently coupled with a fluorophore-conjugated secondary antibody) and a fluorophore-conjugated α -BGT. (A) 3D images of saline-injected TAs. Autofluorescent background (Autofluo) signal in the 488 nm channel was used to highlight the muscle structure and is shown in green, eMHC in red and presence of AChR in white. No constitutive expression of eMHC was observed in this sample. Scale bar: 1 mm. (B) Magnification of the postsynaptic structures showed the preservation of their classical pretzel-like shape, without any sign of fragmentation.

Once analyzed the control, the muscle who was injected with glycerol five days before dissection was investigated. As mentioned before, data from classical immunohistochemistry showed a peak in eMHC expression at this timepoint. As shown in Figure 28, those findings were confirmed from the whole mount three-dimensional scan of the glycerol treated muscle: eMHC presence was evident within the muscle, and seemed to be concentrated in the area where the injection site could be located (circular-shape wound, is clearly visible in the upper right and middle right panels).

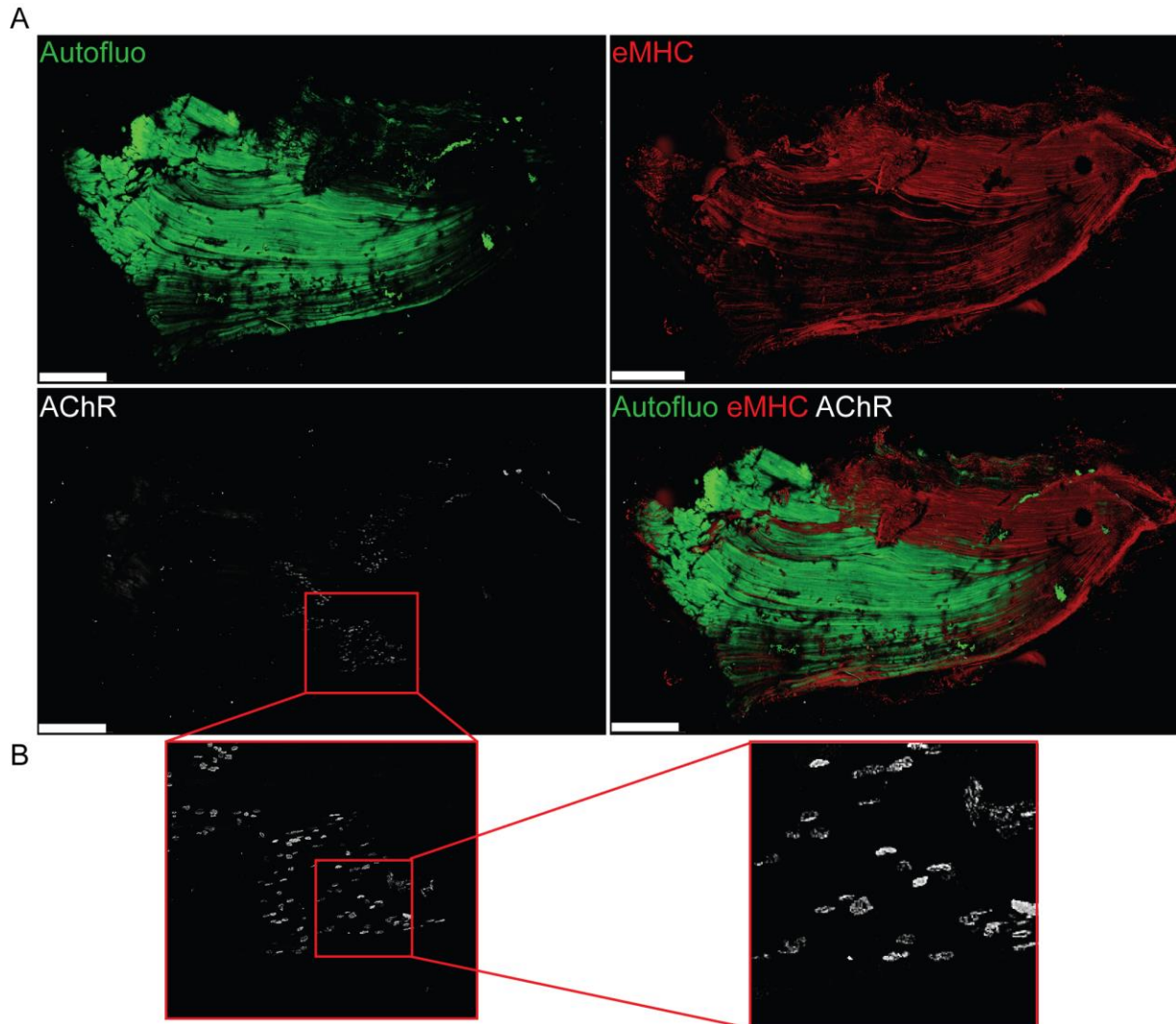


Figure 28- eMHC expression in glycerol-injected TA, postsynaptic structure is preserved. Five days after glycerol injection, TA muscle was dissected and cleared using the MYOCLEAR procedure and then immunostained with anti-eMHC antibody (subsequently coupled with a fluorophore-conjugated secondary antibody) and a fluorophore-conjugated α -BGT. (A) 3D images of saline-injected TAs. Autofluorescent background (Autofluo) signal in the 488nm channel was used to highlight the muscle structure and is shown in green, eMHC in red and presence of AChR in white. Strong presence of eMHC was observed in this sample. Scale bar: 1mm. (B) Magnification of the postsynaptic structures showed the preservation of their classical pretzel-like shape, without any sign of fragmentation.

Moreover, areas that were positive for eMHC did not present a background autofluorescent signal as strong as those regions where eMHC was absent. Another interesting observation was that some fibers were only partially positive for eMHC presence, showing as a perfect example of biological information only obtainable by 3D microscopy. Moving forward to the NMJs, the postsynapses observed seemed unaffected by the degeneration/degeneration mechanism that was occurring in the muscle: none of the NMJs detected in the treated muscle was either fragmented, indicating a possible degeneration of the synapse, nor presented a button-like shape as newly developed synapses could have during their formation. This is clearly shown in Figure 29, where it is possible to appreciate how the postsynapse structure is conserved three days after the glycerol treatment. There are some differences in the cell nuclei presence and in the mIgG distribution. In the control muscle seems to be an

enrichment in cell nuclei, with some of those colocalizing in the NMJs region, while the damaged muscle does not show many cell nuclei near the NMJs. The mIgG presence in the control is detected mainly in those areas that, by their shape, position and size, can be identified as blood vessel, while in the damaged muscle its presence is more ubiquitous. Although interesting, those findings could not be confirmed due to a lack of available samples, but suggest that the glycerol treatment leans more to a “all or nothing” damage mechanism in regards to NMJs: instead of having them to degenerate, showing fragmentation, it leads to a complete disruption of the synapse, that is then reformed anew in the day following the treatment.

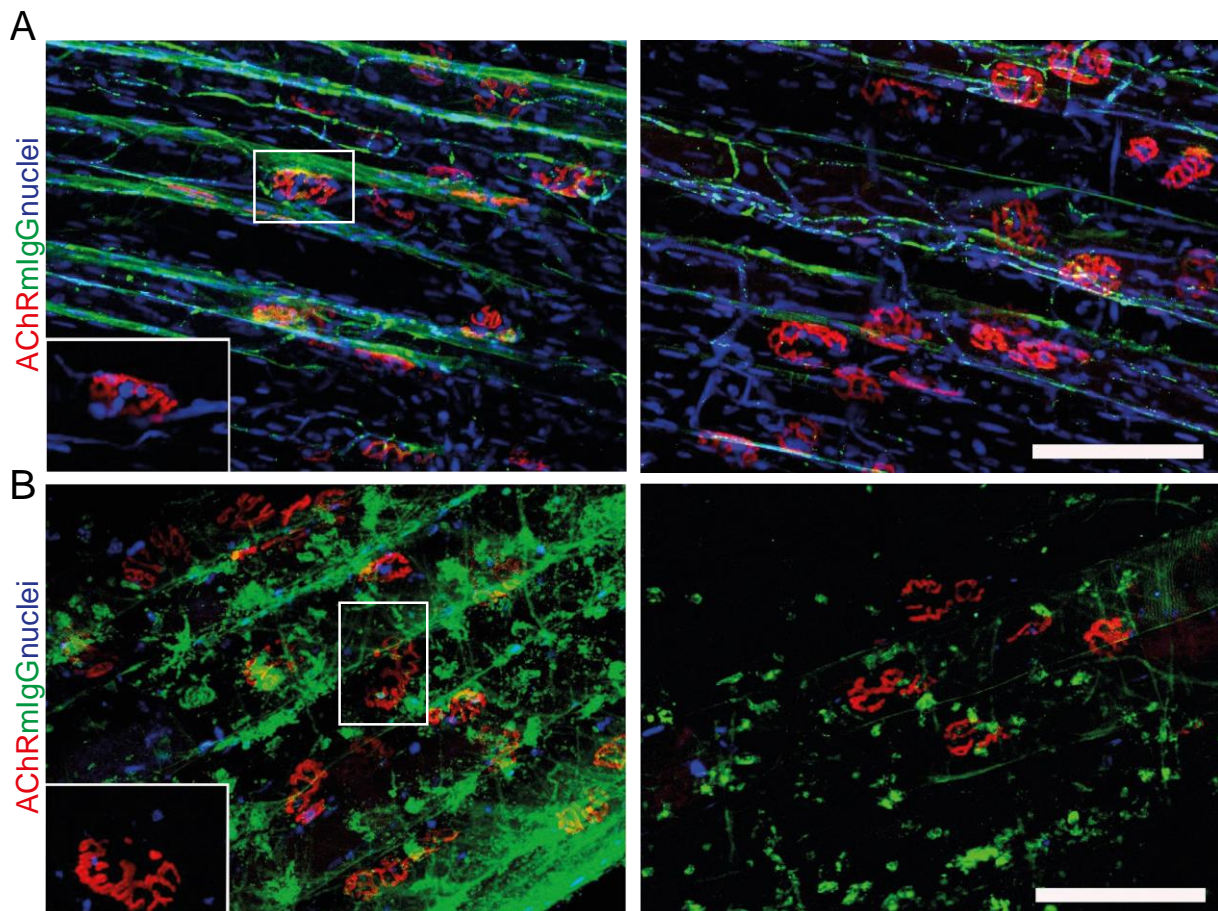


Figure 29- Post-synapses structure is conserved in the glycerol-treated muscles three days after the injection. Three days after glycerol injection, TA muscles were dissected and cleared using the MYOCLEAR procedure and then immunostained with an anti-mouse mIgG antibody fluorophore-conjugated secondary antibody (mIgG, in green) and a fluorophore-conjugated α -BGT (AChR, in red) together with a DAPI to detect cell nuclei (in blue). Confocal tile-scans were then taken and analyzed. (A) 3D images of TA muscle injected with saline, in the magnification is possible to appreciate the post-synapse pretzel-shaped structure. (B) 3D images of TA muscle injected with glycerol, in the magnification is possible to appreciate a similar post-synaptic structure as the one detected in the control. Scale bar: 100 μ m.

5. Discussion

In this study three biological questions were answered:

- i) the possibility that a lower dose of glycerol, respect to the one commonly used, could still effectively induce a damage-recovery mechanism in the skeletal muscle;
- ii) how this kind of damage would affect the neuromuscular junction, as this aspect of muscle regeneration has never been investigated before in such model;
- iii) how a systemic stem cell-based treatment with adipose-derived mesenchymal stem cell could be beneficial for muscle and synapse recovery.

Moreover, the application of the MYOCLEAR tissue clearing protocol on glycerol-treated muscles provided some interesting observations, although the number of experiments performed does not permit to reach any final conclusion on muscle damage and recovery, as well as regarding NMJ status, from a tridimensional point of view.

5.1 Low glycerol dose leads successfully to muscle damage and subsequent recovery

Regarding the first point, a lower amount of 50% glycerol solution (20 μ l) was preferred to the amount normally used 50-100 μ l in the literature (Mahdy 2018). This was decided considering that a higher amount could trigger some undesired secondary effects, such as acute kidney injury linked to rhabdomyolysis, and for technical reasons: glycerol viscosity causes the solution to drip from the injection site, without guaranteeing the same amount to be injected at every procedure, reducing the reproducibility of the experiments. 20 μ l proved to be the maximum amount that was possible to inject in TA muscle without any leakage: any larger amount caused few droplets to not efficiently penetrate the tissue, and so making it impossible to assure the exact quantity of glycerol administered. As the results show, 20 μ l was enough volume to successfully trigger a degeneration-regeneration cycle within the skeletal muscle. Fiber necrosis was present as early as eighteen hours after the injection, and necrotic myofibers were seen up to three days after the procedure. The levels of mIgG (and more in general of serum proteins) did not come back to normal levels until eleven days after the glycerol treatment. A similar trend was presented by the collagen I deposition, indicating intense muscle fibrosis at three days after the injection, which lasted in a milder form until eleven days. This indicated that, while glycerol led to an intense acute tissue necrosis and fibrosis at early timepoints, it lasted more than few days. Compared to models using higher volumes of 50% glycerol solution, the present less severe approach was able to avoid a late fibrosis phase, as it is usually reported (Mahdy et al. 2015). Simultaneous to the occurrence of the first necrotic fibers, loss of f-actin and dystrophin as markers for functional skeletal muscle fibers was observed. However, these proteins showed faster return to normal levels. To assess muscle regeneration, the amount of eMHC+ and/or center-nucleated myofibers (CNFs) as well as the overall total fiber counts were monitored. Fibers positive for eMHC were transiently increased between five and eight days post-injection in glycerol-treated muscles. Conversely, CNFs were also present at five days post glycerol injection but then

persisted in the treated muscles. Finally, reduced fiber numbers were only found at three days post glycerol and then rapidly returned to normal values. Overall, those findings defined the 20 μ l glycerol injection procedure as an efficient muscle damage/regeneration model causing injury to the tissue in the early phase with severe necrosis and fibrosis together with widespread loss of functional muscle markers, followed by a regenerative response that ultimately leads to nearly complete recovery of the tissue in few days. Thus, this model presented the features in term of possibility to study muscle degeneration and recovery that deemed it apt to study possible therapeutic effects of ASCs application.

5.2 Presynapses and postsynapses show a different sensitivity and recovery rate after glycerol-induced muscle damage

As the NMJ recovery has never been studied in a glycerol-induced muscle damage model, its disruption and recovery were investigated. This showed that the pre- and postsynaptic compartments responded differently to the glycerol treatment. The postsynapses, while suffering a non-significant reduction over the investigated time period, showed a good degree of resilience against the effect of glycerol injection. A limited reduction in the number of AChR+ sites respect to the ones detected in the controls was observed only eleven days after the treatment. Conversely, while the percentage positive sites for VACHT among those positive for AChR (and then indicating the presence of co-localized presynapses at postsynaptic sites) was around 97% in the controls, it was significantly reduced in the glycerol treated muscles between three and eleven days after the glycerol injection. Indeed, VACHT was missing in around 60% of postsynaptic regions at three days post-injection, but then showed a continued partial recovery during the experimental period. Notably, postsynaptic sites were detected also in highly necrotic areas where the muscle was heavily damaged. This study cannot present formal proof that such sites were subsequently reinnervated, but the rather constant amounts of postsynapses detected throughout the experiment argue against a massive phase of ectopic synapse formation. Depending on the type of muscle damage model, different methods can target or affect different muscle compartments. Models based on mechanical, freeze or ischemic injury disrupted the plasma membrane effectively, but their effect on other elements was limited, as, for example, they left the extracellular matrix component intact for the most part (McMahan, Edgington, and Kuffler 1980; Slater and Schiaffino 2008; Anderson et al. 2017). In contrast, glycerol can lead to an extensive damage to the extracellular matrix (Mahdy et al. 2015; Hardy et al. 2016; Mahdy 2018). Since an intact extracellular matrix was previously described as an important prerequisite for both, postsynaptic preservation and guidance of motor axons to original synaptic sites (McMahan, Edgington, and Kuffler 1980), it was an interesting of this study that the loss of the extracellular matrix did apparently not strongly affect AChR postsynaptic maintenance, but resulted in a specific loss of presynaptic terminals.

This effect could be ascribed to a partial matching between the pre- and postsynapse, resulting in an impaired synapse recovery. Such effect was reported when studying the role of laminins

in regards to basal lamina perturbation and their effect of NMJs (Rogers and Nishimune 2017).

Although recovery of the presynapses was incomplete in our paradigm, it appeared to be faster than reported upon tourniquet (Tu et al. 2017) or nerve injury (Zainul et al. 2018). In both cases, complete presynaptic recovery was observed several weeks after the injury. One might speculate that the low amount of glycerol applied in the present study acted only locally, allowing a faster regrowth of motor neuron axons. Along with the characterization of muscle degeneration and regeneration, the glycerol model proved interesting also as a tool for studying synapse destruction and recovery.

5.3 Adipose-derived mesenchymal stem cell systemic application as beneficial, although transient, effect on skeletal muscle and NMJ recovery

The successful establishment of a glycerol-based muscle degeneration/regeneration model combined with its phenomenological characterization of muscle and NMJ behavior under these conditions, prompted to use this model for further investigation of possible therapeutic approaches. Adipose-derived stem cells (ASCs) were found to be interesting for possible clinical applications due to their differentiation capability (Timper et al. 2006; Radtke et al. 2009; Deshpande, Grayson, and Spector 2015), their beneficial effects on other cell types involved in tissue regeneration, and their immunomodulatory properties. In this study, it was observed that systemic administration of ASCs in mice led to major differences in the muscle recovery profiles compared to mice treated with glycerol only. Firstly, in the presence of ASCs the levels of mIgG and collagen I in the glycerol-injected muscles were less affected than in the absence of ASCs, indicating a reduced severity of the initial degeneration. Also, the early detection of eMHC and diminished loss of presynaptic sites indicated an overall milder damage was present at three days post-injection. Secondly, however, the amount of mIgG, tissue fibrosis and center-nucleated myofibers were found to rise at eleven days after the treatment, suggesting the presence of a secondary damage or a differing regenerative phase. Fitting to this, also presynaptic NMJ recovery, which appeared to be faster at early time points upon ASCs treatment, was reduced eleven days after the treatment, were VACHT+ postsynaptic sites were reduced from around 80% at five days post-injection to around 57%. Although there is currently no formal proof, the observed alterations in the presence of ASCs could altogether be due to an immune cell mobilization in the muscle. Initially, immune cells could have dampened the disruptive effect of glycerol on the muscle fiber, thereby reducing myofiber necrosis and the intensity of inflammation. Subsequently, they could have affected muscle recovery via, for instance, an IL-6 dependent mechanism: Indeed, direct injection of mesenchymal/stromal cells was found to increase IL-6 levels by promoting the switch from M1 to M2 macrophages, thus also stimulating muscle stem cell activity (Arnold et al. 2007; Saclier, Yacoub-Youssef, et al. 2013; Mahdy 2018). Moreover, macrophage-secreted IL-6 has been shown to improve muscle regeneration (Meng et al. 2014). ASCs could also directly affect muscle tissue remodeling and muscle cell maturation by

actively migrating to affected muscles (Vieira et al. 2012). In this way, ASCs could enhance muscle regeneration (Rodriguez et al. 2005; Rybalko et al. 2017). Further, ASCs could influence muscle recovery through the release of paracrine factors which are involved in the modulation of the immune response and degeneration-regeneration processes. Recent studies on ASCs secretome therapeutic effect on an ischemic muscle damage model favor this hypothesis describing it as principal therapeutic mechanism (Mitchell et al. 2019; Figliolini et al. 2020). Figliolini, in particular, demonstrated how ASC-derived exosomes were able to promote vascular growth and tissue regeneration. Interestingly, the effect of adipose stem cell-derived extracellular vesicles in an ischemic model of muscle damage resulted in a less severe damage and in an increase in the expression of myogenic transcription factors, such as *MyoD*, *myogenin* and *Myf5*, along with *Pax7*. In support of a paracrine action of ASCs it has to be noted that we could not find ASCs in the treated muscles, thus excluding the possibility that ASCs had exerted their beneficial effects directly.

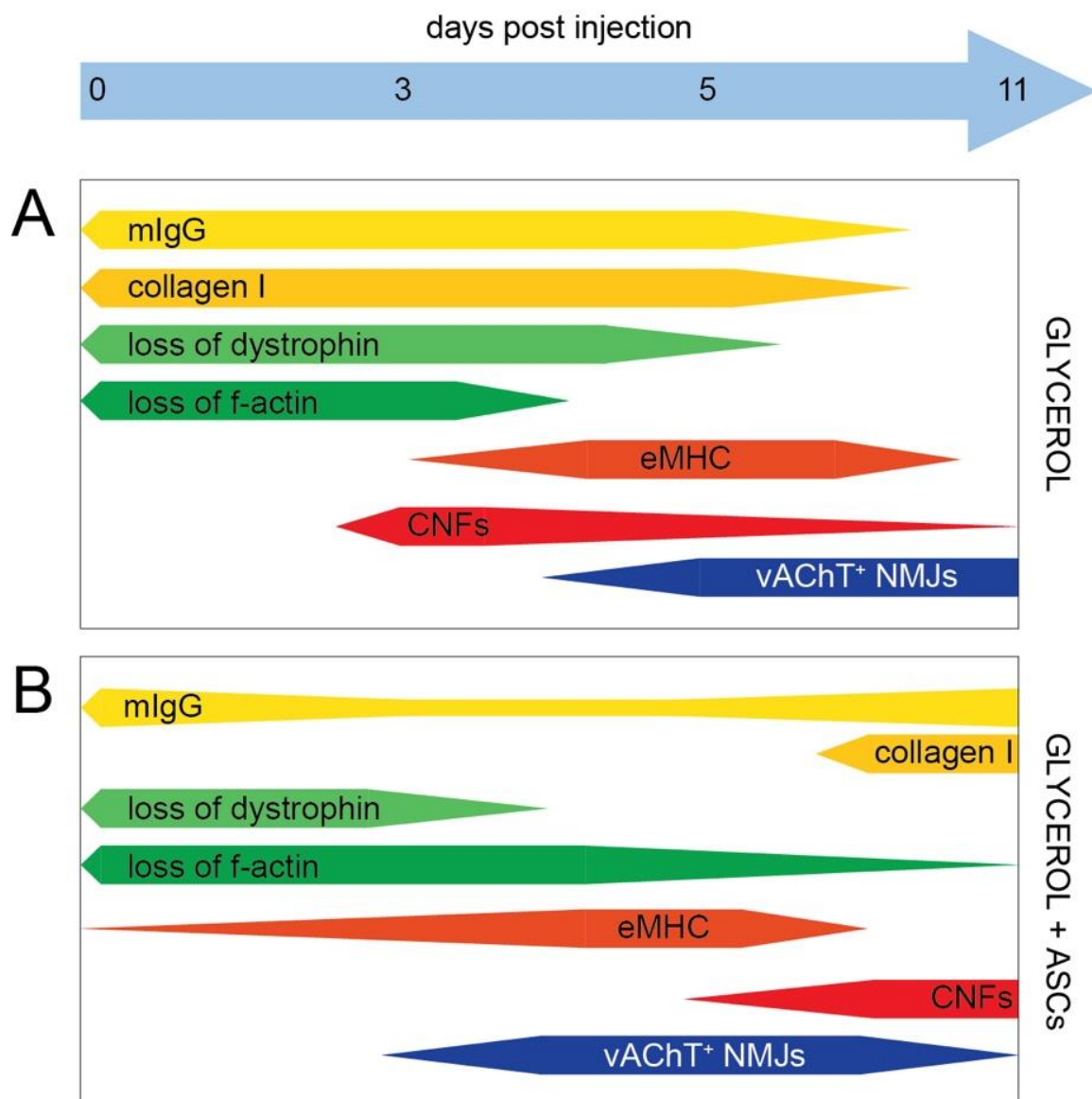


Figure 30- Schematic summary of glycerol injection with or without ASCs systemic application on skeletal muscle tissue. The bars indicate the presence of markers as labeled, with the bar width indicating the amount. mIgG was used to quantify muscle necrosis and inflammation, while collagen I to quantify fibrotic tissue

deposition. The number of VAcHT+ NMJs is referred to the percentage of colocalized VAcHT signals on the total of the AChR+ signals detected.

5.4 MYOCLEAR tissue clearing protocol proved to be promising for the three-dimensional investigation of neuromuscular junction structure and regeneration of glycerol-treated muscles.

As already stated, three-dimensional investigation of samples can shed a new light on many biological processes. While, in principle, also classical two-dimensional analysis could provide the kind of data that can lead to a tri-dimensional reconstruction, tissue clearing and confocal microscopy can provide images that directly relate to biological information, in particular those regarding to localization, shape and size of definite structure. Further, by avoiding the virtual three-dimensional reconstruction phase from bi-dimensional images, optical tissue clearing strongly reduces possible mistakes or misinterpretation that might arise during the data processing phase. Yet, optical tissue clearing must tackle important challenges, particularly to find a compromise between reducing the natural opaqueness of biological tissue and preserving tissue-specific arrangement of markers and fluorescence of dyes. Thus, past and present protocols need to pay particular attention to (Richardson and Lichtman 2015; Silvestri et al. 2016):

- i) the biological questions posed and the methods chosen in order to answer them. This is linked to the fact that epitopes or structures of interest can be marked in different ways, with fluorophore-coupled toxins, dyes or using a combination of primary and secondary antibody. Not every tissue clearing method has the same effectiveness, and some are just not compatible with one or more staining protocols.
- ii) the kind of sample that need to be cleared. Tissues react differently based on their composition to clearing methods, and suitable protocols for the clearing of brain tissue could be completely ineffective when applied to a muscle. Moreover, the size of the sample has to be taken in account, as some techniques present limitations regarding the volume, as well as some microscopes.
- iii) technical limitations, as some tissue clearing protocols (in particular those based on active clearing) could require specific machinery or reagents not readily available. Also, while some methods can achieve optimal results in a matter of hours, other can require weeks to reach the stage where the sample is ready for imaging.

Considering these three main factors, a custom-made method was developed starting from CLARITY in order to effectively locate and image NMJs in muscle tissue. This protocol,

termed MYOCLEAR, was successfully applied and tested, resulting in a complete segmentation (mostly automated, with only few additional signals that needed to be hand-segmented) of the NMJs of murine *extensor digitorum longus* (EDL) muscles. It considered and solved the above-mentioned main issues of optical clearing protocols as follows:

- i) MYOCLEAR has been specifically designed to achieve the visualization of NMJs in the murine muscle with the use of fluorophore-coupled toxins (in this specific case, bungarotoxin).
- ii) it was tailored for its use on skeletal muscle, although its applicability to other organs or tissues is likely.
- iii) it uses mostly readily available materials and machinery, with also the possibility to build some of them “in-house”.

Therefore, MYOCLEAR proved to possess several advantages respect to previous hydrogel-based tissue clearing protocol. While other CLARITY-derived protocols showed a loss of fluorescence when using fluorophore-coupled α BGT (Milgroom and Ralston 2016; Zhang et al. 2018), MYOCLEAR was compatible with this dye, leading to a precise and defined localization and evaluation of NMJs within muscle tissue, allowing a precise quantification of the NMJ number along the whole EDL, by hand or semi-automated segmentation of whole mount images. Indeed, a murine EDL is normally composed of muscle fiber numbers ranging from 758 to 1435 (White et al. 2010; Bloemberg and Quadrilatero 2012). When counted from cryosections of our samples, the number of muscle fibers amounted to 1052 ± 42 (mean \pm standard deviation). Considering that each muscle fiber in an adult muscle is exclusively innervated by one NMJ (Krause 1863), the number of NMJ that was assumed to be present in the muscle analyzed was assumed to be in the same range as the one obtained from the muscle fibers count. Since MYOCLEAR revealed an average of $1082.3 \pm 29.5 \pm 42$ (mean \pm standard deviation), it proved to detect next to all NMJs present in a murine EDL. Moreover, the quality of the signal allowed a morphological evaluation of NMJs structure, as conducted using a subset of parameters from those listed by Jones et al. (Jones et al. 2016). NMJs in muscles dissected from wild type and dystrophic (*mdx*) mice were analyzed measuring their area, perimeter, size (measured as the diagonal of the bounding rectangle) and fragmentation index. One interesting finding when those parameters were evaluated is that they significantly changed depending on the region of the tissue considered, particularly in regards of the fragmentation index in *mdx* muscles (Williams et al. 2019). Further, MYOCLEAR proved also to be applicable in combination with other dyes as well as primary and secondary antibodies, showing a considerable degree of flexibility that is not always granted by other tissue clearing protocols. In particular, immunostaining using antibodies for presynapses (VACHT), sarcomere (troponin I), sarcolemma (dystrophin) and extracellular matrix (collagen I) was demonstrated in this context. However, it has to be noted that only VACHT was visible beyond 500 μ m within the tissue, while the other markers were detected only on a more

superficial level, for about 200-300 μm . A possible improvement to achieve a better antibody penetration could arise from the use of additional techniques to grant a better penetration of the antibodies, such as stochastic electrotransport (S. Y. Kim et al. 2015; Nehrhoff et al. 2016). A further limitation that was evident in MYOCLEAR was a strong autofluorescence in the blue to red fluorescence range, which was probably due to PFA-fixation induced chromophore formation (Baschong, Suetterlin, and Hubert Laeng 2001), limiting the possible options in matter of wavelengths available. Although that could be consider an issue, it can also prove useful since it allows to track individual muscle fibers. Moreover, it can be utilized to analyze some pathophysiological parameter, such as the presence of center-nucleated muscle cells, atrophic fibers, fiber splitting and other structural information. In order to detect at least two stained structures in the muscle, the dyes AlexaFluor647 and Draq5 were applied, since there is a slight shift in their emission wavelengths, in combination with spectral unmixing in the data-processing phase (Zimmermann et al. 2002). To avoid the occurrence of autofluorescence, it would be necessary to apply a different fixation protocol than the PFA incubation. In summary, MYOCLEAR is an advancement from previous CLARITY-based protocols, that is particularly tuned to permit the quantitative analysis of NMJ-related features in murine muscle whole mounts.

With respect to the present study, MYOCLEAR was used to address fragmentation of NMJs upon glycerol as well as the correlation between loss of synapses and muscle damage. Although the experimental replicates were not enough to guarantee a satisfactory degree of certainty, some qualitative observations were made regarding muscle and postsynapse regeneration in the glycerol-induced muscle damage model. In particular, eMHC-positive muscle fibers and neuromuscular junction presence were investigated. Although a complete imaging of the whole *tibialis anterior* muscles was not achieved due to their size, a penetration of $\sim 500 \mu\text{m}$ was observed. MYOCLEAR allowed to obtain some preliminary results on NMJ status and regenerating muscle fiber.

First, regarding endplate regeneration, postsynapse fragmentation in the glycerol-treated muscles was not observed at the tested time-points, suggesting that postsynapse loss in glycerol-injected muscles occurred in an “all or nothing” mechanism: those synapses who were affected by the injection were completely disrupted and quickly eliminated from the tissue, while the remnants were unaffected, conserving their typical “pretzel-shaped” structure. Another possibility is the “upstream” hypothesis: glycerol effects could be severely detrimental to the nerve, hence causing the presynapses to disrupt, while any effect on the postsynapses would be more directly linked to the condition of the muscle tissue itself. When considering the distribution of the signal corresponding to eMHC presence, three points were made:

- i) eMHC antibody worked well when combined with MYOCLEAR, resulting in the efficient localization of regenerating muscle fibers.

- ii) eMHC signal was not ubiquitous along the entire muscle fiber, suggesting that muscle regeneration in this model shows a certain degree of heterogeneity within the muscle.

- iii) Regenerating areas positive for eMHC did not present the autofluorescence in the blue to red wavelengths.

Where detected, eMHC did not seem to be expressed along the entire fiber, suggesting that regeneration did not involve the entire myofiber at the same time, but was more localized or it occurred in a “wave-like” manner.

Finally, it was interesting to observe that the autofluorescence in the range of the blue-red wavelengths was pronounced in regenerating fibers compared to those negative for eMHC. Although in need of further confirmation, this suggests that the autofluorescence was present only in adult and/or undamaged myofibers. That could indicate that this phenomenon is linked to the interaction between PFA and one or more components present in the adult muscle tissue that are absent during the regeneration phase. Since muscle recovery is a multi-factorial complex process involving several muscle compartments (Tedesco, F. S., Dellavalle, A., Diaz-Manera, J., Messina, G., & Cossu 2010; Mahdy, Warita, and Hosaka 2016; Mahdy 2018) from the cell nuclei with the expression of myogenic transcription factors to the extracellular space with the ECM remodeling, the identification of factors cause the PFA-induced autofluorescence would need further studies and experiments. Though, their identification would prove desirable in order to avoid the PFA-induced autofluorescence and then increasing the wavelength availability in MYOCLEAR.

6. Summary

Skeletal muscle is an important tissue in the organism, critical for movement and thermoregulation. Muscle tissue has a remarkable ability to regenerate, provided mainly by a subpopulation of muscle cells, referred to as satellite cells. A better knowledge of this recovery mechanism could help researchers and medical practitioners to develop therapeutic approaches to treat muscle-related diseases by pharmacological or stem-cell based means. Besides muscle cells and structure, also efficient neural transmission is critical for the organ function. This is provided by the neuromuscular junctions (NMJs), which are formed by the alignment of a motor neuronal pre-synaptic compartment and its muscular post-synaptic counterpart. In this thesis a glycerol-induced muscle degeneration/regeneration model was characterized and applied to address the regeneration of muscle and NMJs in the absence and presence of mesenchymal stem cells derived from adipose tissue (ASCs). In the absence of ASCs, glycerol injection led to early fiber necrosis, fibrotic tissue deposition and loss of actin and dystrophin. Between five and eight days after the glycerol injections, regeneration became evident with center-nucleated fibers and the expression of eMHC. Regarding the NMJs, their amount was diminished throughout the entire observation time of eleven days, with a slight recovery at five days post-injection. Notably, presynapses appeared to be more susceptible to glycerol damage than postsynapses and a complete recovery was not achieved within the observation window. In the presence of ASCs, the initial glycerol-induced damage was reduced compared to the glycerol-only model, but a recurrent inflammation and fibrosis was detected eleven days after the injection and the amount of regenerating fibers was higher. Further, in the presence of ASCs, early NMJs recovery was increased, but this was followed by a deterioration eleven days after the treatment. Those findings suggest that, while ASCs exert a beneficial effect in the first days after the treatment, a later inflammatory phase inflicts secondary muscle and NMJ degeneration. Since ASCs could not be detected in the affected muscles, it is likely that their effects on this tissue were rather due to release of signaling molecules than to direct engraftment in the muscle.

In conclusion, a glycerol-based regeneration/degeneration paradigm was successfully established that allows to test properties of skeletal muscle and NMJs in the absence and presence of therapeutic means. This showed a differential sensitivity of pre- and postsynaptic portions to glycerol, as well as transient beneficial and latent inflammatory effects of systemic ASC application on skeletal muscle.

7. References

- Akiyama, C, S Kobayashi, and I Nonaka. 1992. "Comparison of Behavior in Muscle Fiber Regeneration after Bupivacaine Hydrochloride- and Acid." *Acta Neuropathologica* 83: 584–89.
- Allen, Philip G., C. B. Shuster, J. Käs, C. Chaponnier, P. A. Janmey, and I. M. Herman. 1996. "Phalloidin Binding and Rheological Differences among Actin Isoforms." *Biochemistry* 35 (45): 14062–69. <https://doi.org/10.1021/bi961326g>.
- Anderson, Judy E, Mai-khoi Q Do, Nasibeh Daneshvar, Takahiro Suzuki, Junio Dort, Wataru Mizunoya, and Ryuichi Tatsumi. 2017. "The Role of Semaphorin3A in Myogenic Regeneration and the Formation of Functional Neuromuscular Junctions on New Fibres." *Biol. Rev.* 92: 1389–1405. <https://doi.org/10.1111/brv.12286>.
- Apel, Elizabeth D, David J Glass, Lisa M Moscoso, George D Yancopoulos, and Joshua R Sanes. 1997. "Rapsyn Is Required for MuSK Signaling and Recruits Synaptic Components to a MuSK-Containing Scaffold." *Neuron* 18: 623–35.
- Arecco, N., C. J. Clarke, F. K. Jones, D. M. Simpson, D. Mason, R. J. Beynon, and A. Pisconti. 2016. "Elastase Levels and Activity Are Increased in Dystrophic Muscle and Impair Myoblast Cell Survival, Proliferation and Differentiation." *Scientific Reports* 6 (April): 1–20. <https://doi.org/10.1038/srep24708>.
- Arnold, Ludovic, Adeline Henry, Françoise Poron, Yasmine Baba-Amer, Nico Van Rooijen, Anne Plonquet, Romain K. Gherardi, and Bénédicte Chazaud. 2007. "Inflammatory Monocytes Recruited after Skeletal Muscle Injury Switch into Antiinflammatory Macrophages to Support Myogenesis." *Journal of Experimental Medicine* 204 (5): 1057–69. <https://doi.org/10.1084/jem.20070075>.
- Arsic, Nikola, Serena Zacchigna, Lorena Zentilin, Genaro Ramirez-Correa, Lucia Pattarini, Alessandro Salvi, Gianfranco Sinagra, and Mauro Giacca. 2004. "Vascular Endothelial Growth Factor Stimulates Skeletal Muscle Regeneration in Vivo." *Molecular Therapy* 10 (5): 844–54. <https://doi.org/10.1016/j.ymthe.2004.08.007>.
- Aulehla, Alexander, and Olivier Pourquié. 2010. "Signaling Gradients during Paraxial Mesoderm Development." *Cold Spring Harbor Perspectives in Biology* 2 (2): 1–18. <https://doi.org/10.1101/cshperspect.a000869>.
- Bakkar, Nadine, Jingxin Wang, Katherine J Ladner, Huating Wang, Jason M Dahlman, Micheal Carathers, Swarnali Acharyya, Michael A Rudnicki, Andrew D Hollenbach, and Denis C Guttridge. 2008. "IKK/NF- κ B Regulates Skeletal Myogenesis via a Signaling Switch to Inhibit Differentiation and Promote Mitochondrial Biogenesis." *Journal of Cell Biology* 180 (4): 787–802. <https://doi.org/10.1083/jcb.200707179>.
- Baschong, Werner, Rosmarie Suetterlin, and R. Hubert Laeng. 2001. "Control of Autofluorescence of Archival Formaldehyde-Fixed, Paraffin-Embedded Tissue in Confocal Laser Scanning Microscopy (CLSM)." *Journal of Histochemistry and Cytochemistry* 49 (12): 1565–71. <https://doi.org/10.1177/002215540104901210>.
- Belizário, José E, Cibely C Fontes Oliveira, Janaina Padua Borges, Janete Akemi Kashiabara, and Edouard Vannier. 2016. "Skeletal Muscle Wasting and Renewal : A Pivotal Role of Myokine IL - 6." *SpringerPlus*. <https://doi.org/10.1186/s40064-016-2197-2>.
- Bentzinger, C. Florian, Yu Xin Wang, and Michael A. Rudnicki. 2012. "Building Muscle: Molecular Regulation of Myogenesis." *Cold Spring Harb Persp Biol* 94 (July): 32. <https://doi.org/4:a008342>.
- Bieback, Karen, Andrea Hecker, Tanja Schlechter, Ilse Hofmann, Nikos Brousos, Torben Redmer, Daniel Besser, Harald Klter, Albrecht M. Mller, and Matthias Becker. 2012. "Replicative Aging and Differentiation Potential of Human Adipose Tissue-Derived

- Mesenchymal Stromal Cells Expanded in Pooled Human or Fetal Bovine Serum.” *Cytotherapy* 14 (5): 570–83. <https://doi.org/10.3109/14653249.2011.652809>.
- Biral, Donatella, A. Jakubiec-Puka, Iwona Ciechomska, Marco Sandri, Katia Rossini, Ugo Carraro, and Romeo Betto. 2000. “Loss of Dystrophin and Some Dystrophin-Associated Proteins with Concomitant Signs of Apoptosis in Rat Leg Muscle Overworked in Extension.” *Acta Neuropathologica* 100 (6): 618–26. <https://doi.org/10.1007/s004010000231>.
- Bloemberg, Darin, and Joe Quadrilatero. 2012. “Rapid Determination of Myosin Heavy Chain Expression in Rat, Mouse, and Human Skeletal Muscle Using Multicolor Immunofluorescence Analysis.” *PLoS ONE* 7 (4). <https://doi.org/10.1371/journal.pone.0035273>.
- Boldyreva, Maria A., Evgeny K. Shevchenko, Yuliya D. Molokotina, Pavel I. Makarevich, Irina B. Beloglazova, Ekaterina S. Zubkova, Konstantin V. Dergilev, et al. 2019. “Transplantation of Adipose Stromal Cell Sheet Producing Hepatocyte Growth Factor Induces Pleiotropic Effect in Ischemic Skeletal Muscle.” *International Journal of Molecular Sciences* 20 (12). <https://doi.org/10.3390/ijms20123088>.
- Bongers, Kale S, Daniel K Fox, Scott M Ebert, Steven D Kunkel, Michael C Dyle, Steven A Bullard, Jason M Dierdorff, and Christopher M Adams. 2013. “Skeletal Muscle Denervation Causes Skeletal Muscle Atrophy through a Pathway That Involves Both Gadd45a and HDAC4.” *Am J Physiol Endocrinol Metab* 305: 907–15. <https://doi.org/10.1152/ajpendo.00380.2013>.
- Braithwaite, A. W., and A. J. Harris. 1979. “Neural Influence on Acetylcholine Receptor Clusters in Embryonic Development of Skeletal Muscles.” *Nature* 279 (June): 549–51.
- Brennan, T. J., D. G. Edmondson, L. Li, and E. N. Olson. 1991. “Transforming Growth Factor β Represses the Actions of Myogenin through a Mechanism Independent of DNA Binding.” *Proceedings of the National Academy of Sciences of the United States of America* 88 (9): 3822–26. <https://doi.org/10.1073/pnas.88.9.3822>.
- Buckingham, Margaret, Lola Bajard, Ted Chang, Philippe Daubas, Juliette Hadchouel, Sigolène Meilhac, Didier Montarras, Didier Rocancourt, and Frédéric Relaix. 2003. “The Formation of Skeletal Muscle: From Somite to Limb.” *Journal of Anatomy* 202 (1): 59–68. <https://doi.org/10.1046/j.1469-7580.2003.00139.x>.
- Burden, Steven J. 2011. “SnapShot : Neuromuscular Junction.” *Cell* 144 (5): 826-826.e1. <https://doi.org/10.1016/j.cell.2011.02.037>.
- Campanari, Maria Letizia, María Salud García-Ayllón, Sorana Ciura, Javier Sáez-Valero, and Edoardo Kabashi. 2016. “Neuromuscular Junction Impairment in Amyotrophic Lateral Sclerosis: Reassessing the Role of Acetylcholinesterase.” *Frontiers in Molecular Neuroscience* 9 (DEC2016): 1–8. <https://doi.org/10.3389/fnmol.2016.00160>.
- Cantini, M, E Giurisato, C Radu, S Tiozzo, F Pampinella, D Zaniolo, G Senigaglia, F Vitiello, and L Mazzoleni. 2002. “Macrophage-Secreted Myogenic Factors : A Promising Tool for Greatly Enhancing the Proliferative Capacity of Myoblasts in Vitro and in Vivo.” *Neurol Sci* 23: 189–94.
- Carlson, B. 2008. “Muscle Regeneration in Animal Models.” In *Skeletal Muscle Repair and Regeneration*, 163–80. Springer Netherlands.
- Carlson, Bruce M. 2014. “The Biology of Long-Term Denervated Skeletal Muscle.” *Eur J Transl Myol* 24 (1): 5–11.
- Chargé, Sophie B.P., and Michael A. Rudnicki. 2004. “Cellular and Molecular Regulation of Muscle Regeneration.” *Physiological Reviews* 84 (1): 209–38. <https://doi.org/10.1152/physrev.00019.2003>.
- Chazaud, Bénédicte. 2016. “Inflammation during Skeletal Muscle Regeneration and Tissue Remodeling: Application to Exercise-Induced Muscle Damage Management.” *Immunology and Cell Biology* 94 (2): 140–45. <https://doi.org/10.1038/icb.2015.97>.

- Chung, Kwanghun, Jenelle Wallace, Sung-yon Kim, Sandhiya Kalyanasundaram, Aaron S Andalman, Thomas J Davidson, Julie J Mirzabekov, et al. 2013. "Structural and Molecular Interrogation of Intact Biological Systems." *Nature* 497 (7449): 332–37. <https://doi.org/10.1038/nature12107>.
- Czerwinska, Areta M., Wladyslawa Streminska, Maria A. Ciemerych, and Iwona Grabowska. 2012. "Mouse Gastrocnemius Muscle Regeneration after Mechanical or Cardiotoxin Injury." *Folia Histochemica et Cytobiologica* 50 (1): 144–53. <https://doi.org/10.5603/FHC.2012.0021>.
- Deguisse, Marc-olivier, Yves De Repentigny, Alexandra Tierney, Ariane Beauvais, Jean Michaud, Lucia Chehade, Mohamed Thabet, et al. 2020. "Motor Transmission Defects with Sex Differences in a New Mouse Model of Mild Spinal Muscular Atrophy." *EBoMedicine* 55. <https://doi.org/10.1016/j.ebiom.2020.102750>.
- Delaney, Kamila, Paulina Kasprzycka, Maria Anna Ciemerych, and Malgorzata Zimowska. 2017. "The Role of TGF- β 1 during Skeletal Muscle Regeneration." *Cell Biology International* 41 (7): 706–15. <https://doi.org/10.1002/cbin.10725>.
- Demonbreun, Alexis R., Mattia Quattrocelli, David Y. Barefield, Madison V. Allen, Kaitlin E. Swanson, and Elizabeth M. McNally. 2016. "An Actin-Dependent Annexin Complex Mediates Plasma Membrane Repair in Muscle." *Journal of Cell Biology* 213 (6): 705–18. <https://doi.org/10.1083/jcb.201512022>.
- Demonbreun, Alexis R., Ann E. Rossi, Manuel G. Alvarez, Kaitlin E. Swanson, H. Kieran Deveaux, Judy U. Earley, Michele Hadhazy, et al. 2014. "Dysferlin and Myoferlin Regulate Transverse Tubule Formation and Glycerol Sensitivity." *American Journal of Pathology* 184 (1): 248–59. <https://doi.org/10.1016/j.ajpath.2013.09.009>.
- Deshpande, Rajiv S, Warren L Grayson, and Alexander A Spector. 2015. "A Modeling Insight into Adipose-Derived Stem Cell Myogenesis." *PLoS ONE* 10 (9): 1–17. <https://doi.org/10.1371/journal.pone.0137918>.
- Dodt, Hans Ulrich, Ulrich Leischner, Anja Schierloh, Nina Jährling, Christoph Peter Mauch, Katrin Deininger, Jan Michael Deussing, Matthias Eder, Walter Zieglgänsberger, and Klaus Becker. 2007. "Ultramicroscopy: Three-Dimensional Visualization of Neuronal Networks in the Whole Mouse Brain." *Nature Methods* 4 (4): 331–36. <https://doi.org/10.1038/nmeth1036>.
- Dumont, Nicolas A., C. Florian Bentzinger, Marie Claude Sincennes, and Michael A. Rudnicki. 2015. "Satellite Cells and Skeletal Muscle Regeneration." *Comprehensive Physiology* 5 (3): 1027–59. <https://doi.org/10.1002/cphy.c140068>.
- Duregotti, Elisa, Giulia Zanetti, Michele Scorzeto, Aram Megighian, Cesare Montecucco, Marco Pirazzini, and Michela Rigoni. 2015. "Snake and Spider Toxins Induce a Rapid Recovery of Function of Botulinum Neurotoxin Paralyzed Neuromuscular Junction." *Toxins* 7 (12): 5322–36. <https://doi.org/10.3390/toxins7124887>.
- Ertürk, Ali, Klaus Becker, Nina Jährling, Christoph P. Mauch, Caroline D. Hojer, Jackson G. Egen, Farida Hellal, Frank Bradke, Morgan Sheng, and Hans Ulrich Dodt. 2012. "Three-Dimensional Imaging of Solvent-Cleared Organs Using 3DISCO." *Nature Protocols* 7 (11): 1983–95. <https://doi.org/10.1038/nprot.2012.119>.
- Erturk, Ali, Chenchen Pan, Ruiyao Cai, Francesca Paola Quacquarelli, Alireza Gasemigharagoz, and Ali Erturk. 2016. "Whole Organ and Organism Tissue Clearing by UDISCO." *Protocol Exchange*, 1–11. <https://doi.org/10.1038/protex.2016.055>.
- Feng, Fei, Jing-xiu Deng, Ling-li Luo, and Qi-shun Huang. 2019. "Role of the Notch Signaling Pathway in Fibrosis of Denervated Skeletal Muscle." *Current Medical Science* 39 (3): 419–25.
- Fex, S, B Sonesson, S Thesleff, and J Zelena. 1966. "Nerve Implants in Botulinum Poisoned Mammalian Muscle." *J. Physiol.* 184: 872–82.
- Figliolini, Federico, Andrea Ranghino, Cristina Grange, Massimo Cedrino, Marta Tapparo,

- Claudia Cavallari, Andrea Rossi, et al. 2020. "Extracellular Vesicles From Adipose Stem Cells Prevent Muscle Damage and Inflammation in a Mouse Model of Hind Limb Ischemia: Role of Neuregulin-1." *Arterioscler Thromb Vasc Biol*, no. 40: 239–54. <https://doi.org/10.1161/ATVBAHA.119.313506>.
- Flucher, B E, and M P Daniels. 1989. "Distribution of Na⁺ Channels and Ankyrin in Neuromuscular Junctions Is Complementary to That of Acetylcholine Receptors and the 43 Kd Protein." *Neuron* 3 (2): 163–75. [https://doi.org/10.1016/0896-6273\(89\)90029-9](https://doi.org/10.1016/0896-6273(89)90029-9).
- Garg, Koyal, Benjamin T. Corona, and Thomas J. Walters. 2015. "Therapeutic Strategies for Preventing Skeletal Muscle Fibrosis after Injury." *Frontiers in Pharmacology* 6 (APR). <https://doi.org/10.3389/fphar.2015.00087>.
- Gautam, Medha, Peter G Noakes, Lisa Moscoso, Fabio Rupp, Richard H Scheller, John P Merlie, and Joshua R Sanes. 1996. "Defective Neuromuscular Synaptogenesis in Agrin-Deficient Mutant Mice." *Cell* 85: 525–35.
- Gillies, Allison R, and Richard L Lieber. 2011. "Structure and Function of the Skeletal Muscle Extracellular Matrix." *Muscle Nerve* 44 (3): 318–31. <https://doi.org/10.1002/mus.22094.Structure>.
- Gois Beghini, Daniela, Samuel Iwao Horita, Liana Monteiro da Fonseca Cardoso, Luiz Anastacio Alves, Kanneboyina Nagaraju, and Andrea Henriques-Pons. 2019. "A Promising Future for Stem-Cell-Based Therapies in Muscular Dystrophies-In Vitro and In Vivo Treatments to Boost Cellular Engraftment." *International Journal of Molecular Sciences* 20 (21). <https://doi.org/10.3390/ijms20215433>.
- Gokhin, David S., and Velia M. Fowler. 2011. "Cytoplasmic γ -Actin and Tropomodulin Isoforms Link to the Sarcoplasmic Reticulum in Skeletal Muscle Fibers." *Journal of Cell Biology* 194 (1): 105–20. <https://doi.org/10.1083/jcb.201011128>.
- Gorecka, Agata, Souzan Salemi, Deana Haralampieva, Federica Moalli, Deborah Stroka, Daniel Candinas, Daniel Eberli, and Lukas Brügger. 2018. "Autologous Transplantation of Adipose-Derived Stem Cells Improves Functional Recovery of Skeletal Muscle without Direct Participation in New Myofiber Formation." *Stem Cell Research and Therapy* 9 (1): 1–12. <https://doi.org/10.1186/s13287-018-0922-1>.
- Gwyn, D. G., and J T Aitken. 1966. "The Formation of New Motor Endplates in Mammalian Skeletal Muscle." *J. Anat.* 100 (1): 111–26.
- Haddix, Seth G., Young Il Lee, Joe N. Kornegay, and Wesley J. Thompson. 2018. "Cycles of Myofiber Degeneration and Regeneration Lead to Remodeling of the Neuromuscular Junction in Two Mammalian Models of Duchenne Muscular Dystrophy." *PLoS ONE* 13 (10): 1–24. <https://doi.org/10.1371/journal.pone.0205926>.
- Hardy, David, Aurore Besnard, Mathilde Latil, Grégory Jouvion, David Briand, Cédric Thépenier, Quentin Pascal, et al. 2016. "Comparative Study of Injury Models for Studying Muscle Regeneration in Mice." *PloS One* 11 (1): e0147198. <https://doi.org/10.1371/journal.pone.0147198>.
- Hou, Bing, Dan Zhang, Shan Zhao, Mengping Wei, Zaifu Yang, Shaoxia Wang, Jiarui Wang, et al. 2015. "Scalable and DiI-Compatible Optical Clearance of the Mammalian Brain." *Frontiers in Neuroanatomy* 9 (FEB): 1–11. <https://doi.org/10.3389/fnana.2015.00019>.
- Huang, Rongshuang, Min Shi, Fan Guo, Yuying Feng, Yanhuan Feng, and Jing Liu. 2018. "Pharmacological Inhibition of Fatty Protects Against Rhabdomyolysis-Induced Acute Kidney Injury." *Front. Pharmacol.* 9 (August): 1–9. <https://doi.org/10.3389/fphar.2018.00917>.
- Huebner, Kyla D., Davinder S. Jassal, Orna Halevy, Mark Pines, and Judy E. Anderson. 2008. "Functional Resolution of Fibrosis in Mdx Mouse Dystrophic Heart and Skeletal Muscle by Halofuginone." *American Journal of Physiology - Heart and Circulatory Physiology* 294 (4): 1550–61. <https://doi.org/10.1152/ajpheart.01253.2007>.
- Iwata, Yuko, Osamu Suzuki, and Shigeo Wakabayashi. 2013. "Decreased Surface Sialic Acid

- Content Is a Sensitive Indicator of Muscle Damage.” *Muscle and Nerve* 47 (3): 372–78. <https://doi.org/10.1002/mus.23632>.
- Jones, Ross A, Caitlan D Reich, Kosala N Dissanayake, Fanney Kristmundsdottir, Gordon S Findlater, Richard R Ribchester, Martin W Simmen, and Thomas H Gillingwater. 2016. “NMJ-Morph Reveals Principal Components of Synaptic Morphology Influencing Structure – Function Relationships at the Neuromuscular Junction.” *Open Biol.* 6 (160240).
- Judson, Robert N., Stuart R. Gray, Claire Walker, Andrew M. Carroll, Cecile Itzstein, Arimantas Lionikas, Peter S. Zammit, Cosimo De Bari, and Henning Wackerhage. 2013. “Constitutive Expression of Yes-Associated Protein (Yap) in Adult Skeletal Muscle Fibres Induces Muscle Atrophy and Myopathy.” *PLoS ONE* 8 (3): 1–12. <https://doi.org/10.1371/journal.pone.0059622>.
- Kastenschmidt, Jenna M., Kyle L. Ellefsen, Ali H. Mannaa, Jesse J. Giebel, Rayan Yahia, Rachel E. Ayer, Phillip Pham, et al. 2019. “QuantiMus: A Machine Learning-Based Approach for High Precision Analysis of Skeletal Muscle Morphology.” *Frontiers in Physiology* 10 (November). <https://doi.org/10.3389/fphys.2019.01416>.
- Kawai, H., H. Nishino, K. Kusaka, T. Naruo, Y. Tamaki, and M. Iwasa. 1990. “Experimental Glycerol Myopathy: A Histological Study.” *Acta Neuropathologica* 80 (2): 192–97. <https://doi.org/10.1007/BF00308923>.
- Ke, Meng-tsen, Satoshi Fujimoto, and Takeshi Imai. 2013. “SeeDB : A Simple and Morphology-Preserving Optical Clearing Agent for Neuronal Circuit Reconstruction.” *Nature Neuroscience* 16 (8). <https://doi.org/10.1038/nn.3447>.
- Kern, Susanne, Hermann Eichler, Johannes Stoeve, Harald Klüter, and Karen Bieback. 2006. “Comparative Analysis of Mesenchymal Stem Cells from Bone Marrow, Umbilical Cord Blood, or Adipose Tissue.” *Stem Cells* 24 (5): 1294–1301. <https://doi.org/10.1634/stemcells.2005-0342>.
- Kiefer, J C, and S D Hauschka. 2001. “Myf-5 Is Transiently Expressed in Nonmuscle Mesoderm and Exhibits Dynamic Regional Changes within the Presegmented Mesoderm and Somites I-IV.” *Developmental Biology* 232 (1): 77–90. <https://doi.org/10.1006/dbio.2000.0114>.
- Kim, Natalie, and Steven J Burden. 2008. “MuSK Controls Where Motor Axons Grow and Form Synapses.” *Nat Neurosci* 11 (1): 19–27. <https://doi.org/10.1038/jid.2014.371>.
- Kim, Sung Yon, Jae Hun Cho, Evan Murray, Naveed Bakh, Heejin Choi, Kimberly Ohn, Luzdary Ruelas, et al. 2015. “Stochastic Electrotransport Selectively Enhances the Transport of Highly Electromobile Molecules.” *Proceedings of the National Academy of Sciences of the United States of America* 112 (46): E6274–83. <https://doi.org/10.1073/pnas.1510133112>.
- Kim, Sung Yon, Kwanghun Chung, and Karl Deisseroth. 2013. “Light Microscopy Mapping of Connections in the Intact Brain.” *Trends in Cognitive Sciences* 17 (12): 596–99. <https://doi.org/10.1016/j.tics.2013.10.005>.
- Koike, Manabu, Takeo Awaji, Masakazu Kataoka, Gozoh Tsujimoto, Tonja Kartasova, and Aki Koike. 1999. “Differential Subcellular Localization of DNA-Dependent Protein Kinase Components Ku and DNA-PKcs during Mitosis.” *Journal of Cell Science* 112: 4031–39.
- Komatsu, Masatoshi, Tsutomu Nakada, Hiroyuki Kawagishi, Hiroyuki Kato, and Mitsuhiro Yamada. 2018. “Increase in Phospholamban Content in Mouse Skeletal Muscle after Denervation.” *Journal of Muscle Research and Cell Motility* 39 (5–6): 163–73. <https://doi.org/10.1007/s10974-019-09504-2>.
- Korrapati, Midhun C., Brooke E. Shaner, and Rick G. Schnellmann. 2012. “Recovery from Glycerol-Induced Acute Kidney Injury Is Accelerated by Suramin.” *Journal of Pharmacology and Experimental Therapeutics* 341 (1): 126–36.

- <https://doi.org/10.1124/jpet.111.190249>.
- Krause, W. 1863. "Über Die Endigung Der Muskelnerven. Zweiter Artikel." *Zeitschrift. Rat. Med* 20: 1–18.
- Kummer, Terrance T, Thomas Misgeld, Jeff W Lichtman, and Joshua R Sanes. 2004. "Nerve-Independent Formation of a Topologically Complex Postsynaptic Apparatus." *The Journal of Cell Biology* 164 (7): 1077–87. <https://doi.org/10.1083/jcb.200401115>.
- Kummer, Terrance T, Thomas Misgeld, and Joshua R Sanes. 2006. "Assembly of the Postsynaptic Membrane at the Neuromuscular Junction : Paradigm Lost." *Current Opinion in Neurobiology* 16: 74–82. <https://doi.org/10.1016/j.conb.2005.12.003>.
- Laumonier, Thomas, and Jacques Menetrey. 2016. "Muscle Injuries and Strategies for Improving Their Repair." *Journal of Experimental Orthopaedics* 3 (1). <https://doi.org/10.1186/s40634-016-0051-7>.
- Law, Sujata, and Samaresh Chaudhuri. 2013. "Mesenchymal Stem Cell and Regenerative Medicine: Regeneration versus Immunomodulatory Challenges." *American Journal of Stem Cells* 2 (1): 22–38.
- Liu, Dong, Brian L. Black, and Rik Derynck. 2001. "TGF- β Inhibits Muscle Differentiation through Functional Repression of Myogenic Transcription Factors by Smad3." *Genes and Development* 15 (22): 2950–66. <https://doi.org/10.1101/gad.925901>.
- Liu, Haiming, and Ladora V. Thompson. 2019. "Skeletal Muscle Denervation Investigations: Selecting an Experimental Control Wisely." *American Journal of Physiology - Cell Physiology* 316 (3): C456–61. <https://doi.org/10.1152/ajpcell.00441.2018>.
- Lluís, Frederic, Josep Roma, Mònica Suelves, Maribel Parra, Gloria Anierte, Eduard Gallardo, Isabel Illa, et al. 2001. "Urokinase-Dependent Plasminogen Activation Is Required for Efficient Skeletal Muscle Regeneration in Vivo." *Blood* 97 (6): 1703–11. <https://doi.org/10.1182/blood.V97.6.1703>.
- Mahdy, Mohamed A.A. 2018. "Glycerol-Induced Injury as a New Model of Muscle Regeneration." *Cell and Tissue Research* 374 (2): 233–41. <https://doi.org/10.1007/s00441-018-2846-6>.
- Mahdy, Mohamed A A, Hsiao Yin Lei, Jun-ichi Wakamatsu, Yoshinao Z Hosaka, and Takanori Nishimura. 2015. "Comparative Study of Muscle Regeneration Following Cardiotoxin and Glycerol Injury." *Annals of Anatomy* 202: 18–27. <https://doi.org/10.1016/j.aanat.2015.07.002>.
- Mahdy, Mohamed A A, Katsuhiko Warita, and Yoshinao Z Hosaka. 2016. "Early Ultrastructural Events of Skeletal Muscle Damage Following Cardiotoxin-Induced Injury and Glycerol-Induced Injury." *Micron* 91: 29–40. <https://doi.org/10.1016/j.micron.2016.09.009>.
- Mann, Christopher J., Eusebio Perdiguero, Yacine Kharraz, Susana Aguilar, Patrizia Pessina, Antonio L. Serrano, and Pura Muñoz-Cánoves. 2011. "Aberrant Repair and Fibrosis Development in Skeletal Muscle." *Skeletal Muscle* 1 (1): 21. <https://doi.org/10.1186/2044-5040-1-21>.
- Martineau, Eric, Adriana Di Polo, Christine Vande Velde, and Richard Robitaille. 2018. "Dynamic Neuromuscular Remodeling Precedes Motor-Unit Loss in a Mouse Model of ALS." *ELife* 7: 1–19.
- Massimino, M L, E Rapizzi, M Cantini, L Dalla Libera, F Mazzoleni, P Arslan, and U Carraro. 1997. "ED2 / Macrophages Increase Selectively Myoblast Proliferation in Muscle Cultures." *Biochemical and Biophysical Research Communications* 759 (235): 754–59.
- Mauro, Alexander. 1961. "Satellite Cell of Skeletal Muscle Fibers." *The Journal of Biophysical and Biochemical Cytology* 9: 493–95. <https://doi.org/10.1083/jcb.9.2.493>.
- McCarthy, John J., Jyothi Mula, Mitsunori Miyazaki, Rod Erfani, Kelcye Garrison, Amreen B. Farooqui, Ratchakrit Srikuea, et al. 2011. "Effective Fiber Hypertrophy in Satellite

- Cell-Depleted Skeletal Muscle.” *Development* 138 (17): 3657–66.
<https://doi.org/10.1242/dev.068858>.
- McDonald, Abby A., Sadie L. Hebert, Matthew D. Kunz, Steven J. Ralles, and Linda K. McLoon. 2015. “Disease Course in Mdx:Utrophin+/- Mice: Comparison of Three Mouse Models of Duchenne Muscular Dystrophy.” *Physiological Reports* 3 (4): 1–22.
<https://doi.org/10.14814/phy2.12391>.
- McMahan, U. J. 1990. “The Agrin Hypothesis.” *Cold Spring Harb Symp Quant Biol* 55: 407–18.
- McMahan, U. J., D R Edgington, and D P Kuffler. 1980. “Factors That Influence Regeneration of the Neuromuscular Junction.” *Journal of Experimental Biology*.
- Meng, Jiao, Xiaoting Zou, Rimao Wu, Ran Zhong, Dahai Zhu, and Yong Zhang. 2014. “Accelerated Regeneration of the Skeletal Muscle in RNF13-Knockout Mice Is Mediated by Macrophage-Secreted IL-4/IL-6.” *Protein and Cell* 5 (3): 235–47.
<https://doi.org/10.1007/s13238-014-0025-4>.
- Milgroom, Andrew, and Evelyn Ralston. 2016. “Clearing Skeletal Muscle with CLARITY for Light Microscopy Imaging.” *Cell Biol Int* 40 (4): 478–83.
<https://doi.org/doi:10.1002/cbin.10578>.
- Mitchell, Robert, Ben Mellows, Jonathan Sheard, Manuela Antonioli, Oliver Kretz, David Chambers, Marie Theres Zeuner, et al. 2019. “Secretome of Adipose-Derived Mesenchymal Stem Cells Promotes Skeletal Muscle Regeneration through Synergistic Action of Extracellular Vesicle Cargo and Soluble Proteins.” *Stem Cell Research and Therapy* 10 (1): 1–19. <https://doi.org/10.1186/s13287-019-1213-1>.
- Morgan, Jennifer E., and Terence A. Partridge. 2003. “Muscle Satellite Cells.” *International Journal of Biochemistry and Cell Biology* 35 (8): 1151–56.
[https://doi.org/10.1016/S1357-2725\(03\)00042-6](https://doi.org/10.1016/S1357-2725(03)00042-6).
- Murphy, Malea M., Jennifer A. Lawson, Sam J. Mathew, David A. Hutcheson, and Gabrielle Kardon. 2011. “Satellite Cells, Connective Tissue Fibroblasts and Their Interactions Are Crucial for Muscle Regeneration.” *Development* 138 (17): 3625–37.
<https://doi.org/10.1242/dev.064162>.
- Nehrhoff, Imke, Diana Bocancea, Javier Vaquero, Juan José Vaquero, Jorge Ripoll, Manuel Desco, and María Victoria Gómez-Gaviro. 2016. “3D Imaging in CUBIC-Cleared Mouse Heart Tissue: Going Deeper.” *Biomedical Optics Express* 7 (9): 3716.
<https://doi.org/10.1364/boe.7.003716>.
- Ogle, Molly E., Claire E. Segar, Sraeyes Sridhar, and Edward A. Botchwey. 2016. “Monocytes and Macrophages in Tissue Repair: Implications for Immunoregenerative Biomaterial Design.” *Experimental Biology and Medicine* 241 (10): 1084–97.
<https://doi.org/10.1177/1535370216650293>.
- Pisani, Didier F., Cynthia D.K. Bottema, Catherine Butori, Christian Dani, and Claude A. Dechesne. 2010. “Mouse Model of Skeletal Muscle Adiposity: A Glycerol Treatment Approach.” *Biochemical and Biophysical Research Communications* 396 (3): 767–73.
<https://doi.org/10.1016/j.bbrc.2010.05.021>.
- Politi, Panorea K, Sophia Havaki, Panagiota Manta, and George Lyritis. 2006. “Bupivacaine-Induced Regeneration of Rat Soleus Bupivacaine-Induced Regeneration of Rat Soleus Muscle : Ultrastructural and Immunohistochemical Aspects.” *Ultrastructural Pathology* 30 (6): 461–69. <https://doi.org/10.1080/01913120600854434>.
- Pratt, S J, S B Shah, C W Ward, M P Inacio, J P Stains, and R M Lovering. 2013. “Effects of in Vivo Injury on the Neuromuscular Junction in Healthy and Dystrophic Muscles.” *Journal of Physiology* 591: 559–70. <https://doi.org/10.1113/jphysiol.2012.241679>.
- Pratt, Stephen J.P., Sameer B. Shah, Christopher W. Ward, Jaclyn P. Kerr, Joseph P. Stains, and Richard M. Lovering. 2014. “Recovery of Altered Neuromuscular Junction Morphology and Muscle Function in Mdx Mice after Injury.” *Cellular and Molecular*

- Life Sciences* 72 (1): 153–64. <https://doi.org/10.1007/s00018-014-1663-7>.
- Pratt, Stephen J.P., Ana P. Valencia, Gloribel K. Le, Sameer B. Shah, and Richard M. Lovering. 2015. “Pre- and Postsynaptic Changes in the Neuromuscular Junction in Dystrophic Mice.” *Frontiers in Physiology* 6 (SEP). <https://doi.org/10.3389/fphys.2015.00252>.
- Prochniewicz Nakayama, E., T. Yanagida, and F. Oosawa. 1983. “Studies on Conformation of F-Actin in Muscle Fibers in the Relaxed State, Rigor, and during Contraction Using Fluorescent Phalloidin.” *Journal of Cell Biology* 97 (6): 1663–67. <https://doi.org/10.1083/jcb.97.6.1663>.
- Proto, J. D., Y. Tang, A. Lu, W. C.W. Chen, E. Stahl, M. Poddar, S. A. Beckman, et al. 2015. “NF- κ B Inhibition Reveals a Novel Role for HGF during Skeletal Muscle Repair.” *Cell Death and Disease* 6 (4). <https://doi.org/10.1038/cddis.2015.66>.
- Qi, Yisong, Tingting Yu, Jianyi Xu, Peng Wan, Yilin Ma, Jingtian Zhu, Yusha Li, Hui Gong, Qingming Luo, and Dan Zhu. 2019. “FDISCO: Advanced Solvent-Based Clearing Method for Imaging Whole Organs.” *Science Advances* 5: 1–14. <https://doi.org/10.1126/sciadv.aau8355>.
- Radtke, C, B Schmitz, M Spies, J D Kocsis, and P M Vogt. 2009. “Peripheral Glial Cell Differentiation from Neurospheres Derived from Adipose Mesenchymal Stem Cells.” *International Journal of Developmental Neuroscience* 27: 817–23. <https://doi.org/10.1016/j.ijdevneu.2009.08.006>.
- Reis, Natany Garcia, Heloísa Della, Coletta Francescat, Lucas Ferreira De Almeida, Cleonice Giovanini, Roberto Silva Costa, and Terezila Machado Coimbra. 2019. “Protective Effect of Calcitriol on Rhabdomyolysis-Induced Acute Kidney Injury in Rats.” *Scientific Reports*, no. April: 1–10. <https://doi.org/10.1038/s41598-019-43564-1>.
- Renier, Nicolas, Zhuhao Wu, David J. Simon, Jing Yang, Pablo Ariel, and Marc Tessier-Lavigne. 2014. “IDISCO: A Simple, Rapid Method to Immunolabel Large Tissue Samples for Volume Imaging.” *Cell* 159 (4): 896–910. <https://doi.org/10.1016/j.cell.2014.10.010>.
- Richardson, Douglas S., and Jeff W. Lichtman. 2015. “Clarifying Tissue Clearing.” *Cell* 162 (2): 246–57. <https://doi.org/10.1016/j.physbeh.2017.03.040>.
- Rizzuto, E, S Pisu, A Musarò, and Z Del Prete. 2015. “Measuring Neuromuscular Junction Functionality in the SOD1 G93A Animal Model of Amyotrophic Lateral Sclerosis.” *Annals of Biomedical Engineering* 43 (9): 2196–2206. <https://doi.org/10.1007/s10439-015-1259-x>.
- Röder, Ira Verena, Siegfried Strack, Markus Reischl, Oliver Dahley, Muzamil Majid Khan, Olivier Kassel, Manuela Zaccolo, and Rüdiger Rudolf. 2012. “Participation of Myosin Va and Pka Type I in the Regeneration of Neuromuscular Junctions.” *PLoS ONE* 7 (7). <https://doi.org/10.1371/journal.pone.0040860>.
- Rodrigues, Merryl, Yusuke Echigoya, Rika Maruyama, Kenji Rowel Q. Lim, So Ichiro Fukada, and Toshifumi Yokota. 2016. “Impaired Regenerative Capacity and Lower Revertant Fibre Expansion in Dystrophin-Deficient Mdx Muscles on DBA/2 Background.” *Scientific Reports* 6 (December 2017). <https://doi.org/10.1038/srep38371>.
- Rodriguez, Anne Marie, Didier Pisani, Claude A. Dechesne, Caude Turc-Carel, Jean Yves Kurzenne, Brigitte Wdziekonski, Albert Villageois, et al. 2005. “Transplantation of a Multipotent Cell Population from Human Adipose Tissue Induces Dystrophin Expression in the Immunocompetent Mdx Mouse.” *Journal of Experimental Medicine* 201 (9): 1397–1405. <https://doi.org/10.1084/jem.20042224>.
- Rogers, Robert S., and Hiroshi Nishimune. 2017. “The Role of Laminins in the Organization and Function of Neuromuscular Junctions.” *Matrix Biology* 57–58: 86–105. <https://doi.org/10.1016/j.matbio.2016.08.008>.
- Rudolf, Rüdiger, Michael R. Deschenes, and Marco Sandri. 2016. “Neuromuscular Junction

- Degeneration In Muscle Wasting.” *Curr Opin Clin Nutr Metab Care* 19 (3): 177–81. <https://doi.org/10.1097/MCO.0000000000000267>. Neuromuscular.
- Rudolf, Rüdiger, Muzamil Majid Khan, Siegfried Labeit, and Michael R. Deschenes. 2014. “Degeneration of Neuromuscular Junction in Age and Dystrophy.” *Frontiers in Aging Neuroscience* 6 (MAY): 1–11. <https://doi.org/10.3389/fnagi.2014.00099>.
- Rybalko, Viktoriya, Pei Ling Hsieh, Laura M. Ricles, Eunna Chung, Roger P. Farrar, and Laura J. Suggs. 2017. “Therapeutic Potential of Adipose-Derived Stem Cells and Macrophages for Ischemic Skeletal Muscle Repair.” *Regenerative Medicine* 12 (2): 153–67. <https://doi.org/10.2217/rme-2016-0094>.
- Saclier, Marielle, Sylvain Cuvellier, Mélanie Magnan, Rémi Mounier, and Bénédicte Chazaud. 2013. “Monocyte/Macrophage Interactions with Myogenic Precursor Cells during Skeletal Muscle Regeneration.” *FEBS Journal* 280 (17): 4118–30. <https://doi.org/10.1111/febs.12166>.
- Saclier, Marielle, Houda Yacoub-Youssef, Abigail L. Mackey, Ludovic Arnold, Hamida Ardjoune, Melanie Magnan, Frederic Sailhan, et al. 2013. “Differentially Activated Macrophages Orchestrate Myogenic Precursor Cell Fate during Human Skeletal Muscle Regeneration.” *Stem Cells* 31 (2): 384–96. <https://doi.org/10.1002/stem.1288>.
- Sanes, Joshua R., and Jeff W. Lichtman. 1999. “Development of the Vertebrate Neuromuscular Junction.” *Annu. Rev. Neurosci.*, no. 22: 389–442. https://doi.org/10.1007/978-0-387-92708-4_3.
- Sanes, Joshua R., and Jeff W Lichtman. 2001. “Induction, Assembly, Maturation and Maintenance of a Postsynaptic Apparatus.” *Nature Reviews* 2 (November): 791–805.
- Schiaffino, S., L. Gorza, S. Sartore, L. Saggin, and M. Carli. 1986. “Embryonic Myosin Heavy Chain as a Differentiation Marker of Developing Human Skeletal Muscle and Rhabdomyosarcoma. A Monoclonal Antibody Study.” *Experimental Cell Research* 163 (1): 211–20. [https://doi.org/10.1016/0014-4827\(86\)90574-4](https://doi.org/10.1016/0014-4827(86)90574-4).
- Schwarz, Martin K., Annemarie Scherbarth, Rolf Sprengel, Johann Engelhardt, Patrick Theer, and Guenter Giese. 2015. “Fluorescent-Protein Stabilization and High-Resolution Imaging of Cleared, Intact Mouse Brains.” *PLoS ONE* 10 (5): 1–26. <https://doi.org/10.1371/journal.pone.0124650>.
- Serrano, Antonio L., and Pura Muñoz-Cánoves. 2010. “Regulation and Dysregulation of Fibrosis in Skeletal Muscle.” *Experimental Cell Research* 316 (18): 3050–58. <https://doi.org/10.1016/j.yexcr.2010.05.035>.
- Si, Zizhen, Xue Wang, Changhui Sun, Yuchun Kang, Jiakun Xu, Xidi Wang, and Yang Hui. 2019. “Adipose-Derived Stem Cells : Sources , Potency , and Implications for Regenerative Therapies.” *Biomedicine & Pharmacotherapy* 114: 108765. <https://doi.org/10.1016/j.biopha.2019.108765>.
- Silvestri, Ludovico, Irene Costantini, Leonardo Sacconi, and Francesco Saverio Pavone. 2016. “Clearing of Fixed Tissue: A Review from a Microscopist’s Perspective.” *Journal of Biomedical Optics* 21 (8): 081205. <https://doi.org/10.1117/1.jbo.21.8.081205>.
- Slater, Clarke R, and Stefano Schiaffino. 2008. “Innervation of Regenerating Muscle.” In *Skeletal Muscle Repair and Regeneration*, vol. 3, 303–34. Springer, Dordrecht.
- Spalteholz, Werner. 1914. *Über das Durchsichtigmachen von menschlichen und tierischen Präparaten und seine theoretischen Bedingungen, nebst Anhang: Über Knochenfärbung*. Leipzig: S. Hirzel.
- Sugita, Satoshi, Leland L. Fleming, Caleb Wood, Sydney K. Vaughan, Matheus P.S.M. Gomes, Wallace Camargo, Ligia A. Naves, et al. 2016. “VAcHT Overexpression Increases Acetylcholine at the Synaptic Cleft and Accelerates Aging of Neuromuscular Junctions.” *Skeletal Muscle* 6 (1): 1–17. <https://doi.org/10.1186/s13395-016-0105-7>.
- Taetzsch, Thomas, Gregorio Valdez, and Virginia Tech. 2019. “NMJ Maintenance and Repair

- in Aging.” *Curr Opin Physiol* 4: 57–64.
<https://doi.org/10.1016/j.cophys.2018.05.007.NMJ>.
- Tajbakhsh, S. 2009. “Skeletal Muscle Stem Cells in Developmental versus Regenerative Myogenesis.” *Journal of Internal Medicine* 266 (4): 372–89.
<https://doi.org/10.1111/j.1365-2796.2009.02158.x>.
- Tedesco, F. S., Dellavalle, A., Diaz-Manera, J., Messina, G., & Cossu, G. 2010. “Repairing Skeletal Muscle: Regenerative Potential of Skeletal Muscle Stem Cells.” *J Clin Invest*. 120 (January): 11–19. <https://doi.org/10.1172/JCI40373.and>.
- Tidball, James G. 2005. “Inflammatory Processes in Muscle Injury and Repair.” *American Journal of Physiology - Regulatory Integrative and Comparative Physiology* 288 (2 57-2): 345–53. <https://doi.org/10.1152/ajpregu.00454.2004>.
- Tidball, James G., and S. Armando Villalta. 2010. “Regulatory Interactions between Muscle and the Immune System during Muscle Regeneration.” *American Journal of Physiology - Regulatory Integrative and Comparative Physiology* 298 (5).
<https://doi.org/10.1152/ajpregu.00735.2009>.
- Timper, Katharina, Dalma Seboek, Michael Eberhardt, Philippe Linscheid, Mirjam Christcrain, Ulrich Keller, Beat Mu, and Henryk Zulewski. 2006. “Human Adipose Tissue-Derived Mesenchymal Stem Cells Differentiate into Insulin, Somatostatin, and Glucagon Expressing Cells.” *Biochemical and Biophysical Research Communications* 341: 1135–40. <https://doi.org/10.1016/j.bbrc.2006.01.072>.
- Tintignac, Lionel A, Hans-rudolf Brenner, and Markus A Rüegg. 2015. “Mechanisms Regulating Neuromuscular Junction Development and Function and Causes of Muscle Wasting.” *Physiological Reviews* 95: 809–52.
<https://doi.org/10.1152/physrev.00033.2014>.
- Tiryakioglu, Osman, Kamuran Erkoç, Bulent Tunerir, Onur Uysal, H. Firat Altin, Tevfik Gunes, and Selim Aydin. 2015. “The Effect of Iloprost and N-Acetylcysteine on Skeletal Muscle Injury in an Acute Aortic Ischemia-Reperfusion Model: An Experimental Study.” *BioMed Research International* 2015. <https://doi.org/10.1155/2015/453748>.
- Tomer, Raju, Li Ye, Brian Hsueh, and Karl Deisseroth. 2014. “Advanced CLARITY for Rapid and High-Resolution Imaging of Intact Tissues.” *Nature Protocols* 9 (7): 1682–97.
<https://doi.org/10.1038/nprot.2014.123>.
- Torres-Torrillas, Marta, Monica Rubio, Elena Damia, Belen Cuervo, Ayla Del Romero, Pau Peláez, Deborah Chicharro, Laura Miguel, and Joaquin J. Sopena. 2019. “Adipose-Derived Mesenchymal Stem Cells: A Promising Tool in the Treatment of Musculoskeletal Diseases.” *International Journal of Molecular Sciences* 20 (12).
<https://doi.org/10.3390/ijms20123105>.
- Tremblay, Elsa, Éric Martineau, and Richard Robitaille. 2017. “Opposite Synaptic Alterations at the Neuromuscular Junction in an ALS Mouse Model: When Motor Units Matter.” *Journal of Neuroscience* 37 (37): 8901–18. <https://doi.org/10.1523/JNEUROSCI.3090-16.2017>.
- Tu, Huiyin, Dongze Zhang, Ryan M Corrick, Robert L Muellemann, Michael C Wadman, and Yu Long Li. 2017. “Morphological Regeneration and Functional Recovery of Neuromuscular Junctions after Tourniquet-Induced Injuries in Mouse Hindlimb.” *Frontiers in Physiology* 8 (APR): 1–9. <https://doi.org/10.3389/fphys.2017.00207>.
- Vieira, N. M., M. Valadares, E. Zucconi, M. Secco, C. R. Bueno Junior, V. Brandalise, A. Assoni, et al. 2012. “Human Adipose-Derived Mesenchymal Stromal Cells Injected Systemically Into GRMD Dogs without Immunosuppression Are Able to Reach the Host Muscle and Express Human Dystrophin.” *Cell Transplantation* 21 (7): 1407–17.
<https://doi.org/10.3727/096368911X>.
- Vignaud, A., C. Hourde, F. Medja, O. Agbulut, G. Butler-Browne, and A. Ferry. 2010. “Impaired Skeletal Muscle Repair after Ischemia-Reperfusion Injury in Mice.” *Journal*

- of Biomedicine and Biotechnology* 2010: 1–10. <https://doi.org/10.1155/2010/724914>.
- Webster, Micah T, Uri Manor, Jennifer Lippincott-Schwartz, and Chen-Ming Fan. 2016. “Intravital Imaging Reveals Ghost Fibers as Architectural Units Guiding Myogenic Progenitors During Regeneration.” *Cell Stem Cell* 18 (2): 243–52. <https://doi.org/10.1016/j.stem.2015.11.005>.
- Webster, Micah T, Uri Manor, Jennifer Lippincott-Schwartz, and Chen Ming Fan. 2015. “Intravital Imaging Reveals Ghost Fibers as Architectural Units Guiding Myogenic Progenitors during Regeneration.” *Cell Stem Cell*, 2015. <https://doi.org/10.1016/j.stem.2015.11.005>.
- White, Robert B, Anne-sophie Biérinx, Viola F Gnocchi, and Peter S Zammit. 2010. “Dynamics of Muscle Fibre Growth during Postnatal Mouse Development ,White, Biérinx, Gnocchi, Zammit.Pdf.” *BMC Developmental Biology* 10 (21).
- Williams, Marion Patrick Ivey, Matteo Rigon, Tatjana Straka, Sarah Janice Hörner, Manfred Thiel, Norbert Gretz, Mathias Hafner, Markus Reischl, and Rüdiger Rudolf. 2019. “A Novel Optical Tissue Clearing Protocol for Mouse Skeletal Muscle to Visualize Endplates in Their Tissue Context.” *Frontiers in Cellular Neuroscience* 13 (February): 1–12. <https://doi.org/10.3389/fncel.2019.00049>.
- Wu, Yongkang, Martin J. Hoogduijn, Carla C. Baan, Sander S. Korevaar, Ronella De Kuiper, Lin Yan, Lanlan Wang, and Nicole M. Van Besouw. 2017. “Adipose Tissue-Derived Mesenchymal Stem Cells Have a Heterogenic Cytokine Secretion Profile.” *Stem Cells International* 2017. <https://doi.org/10.1155/2017/4960831>.
- Wynn, Thomas A, and Kevin M Vannella. 2016. “Macrophages in Tissue Repair, Regeneration, and Fibrosis.” *Immunity* 44 (3): 450–62. <https://doi.org/10.1016/j.physbeh.2017.03.040>.
- Zainul, Zarin, Anne Heikkinen, Hennariikka Koivisto, Iina Rautalahti, Mika Kallio, Shuo Lin, Heli Härönen, et al. 2018. “Collagen XIII Is Required for Neuromuscular Synapse Regeneration and Functional Recovery after Peripheral Nerve Injury.” *Journal of Neuroscience* 38 (17): 4243–58. <https://doi.org/10.1523/JNEUROSCI.3119-17.2018>.
- Zanotti, S., S. Saredi, A. Ruggieri, M. Fabbri, F. Blasevich, S. Romaggi, L. Morandi, and M. Mora. 2007. “Altered Extracellular Matrix Transcript Expression and Protein Modulation in Primary Duchenne Muscular Dystrophy Myotubes.” *Matrix Biology* 26 (8): 615–24. <https://doi.org/10.1016/j.matbio.2007.06.004>.
- Zhang, Wenli, Shaohua Liu, Weichen Zhang, Wei Hu, Min Jiang, Amin Tamadon, and Yi Feng. 2018. “Skeletal Muscle CLARITY: A Preliminary Study of Imaging the Three-Dimensional Architecture of Blood Vessels and Neurons.” *Cell Journal* 20 (2): 132–37. <https://doi.org/10.22074/cellj.2018.5266>.
- Zimmermann, Timo, Jens Rietdorf, Andreas Girod, Virginie Georget, and Rainer Pepperkok. 2002. “Spectral Imaging and Linear Un-Mixing Enables Improved FRET Efficiency with a Novel GFP2-YFP FRET Pair.” *FEBS Letters* 531 (2): 245–49. [https://doi.org/10.1016/S0014-5793\(02\)03508-1](https://doi.org/10.1016/S0014-5793(02)03508-1).

8. Appendix

List of the figures

Figure 1- Satellite cells activation upon injury. Satellite cells are subjected to asymmetric cell division, differentiation towards myocytes and subsequent fusion and further differentiation. They are responsible to muscle fiber turnover and recovery. At different stages different transcription factors regulate the differentiation towards new mature myofibers (from Tedesco et al., 2010). For a more detailed description of 1

Figure 2- Transcription factor hierarchy in myogenesis. A strict regulation of the expression of specific transcription factors guarantees the successful formation of myofibers. This process is partially recapitulated during muscle regeneration. Figure from Bentzinger, 2012 (Bentzinger, Wang, and Rudnicki 2012)..... 3

Figure 3- Schematic representation of the different phases of skeletal muscle regeneration. Following injury, inflammatory cells will be recruited to the damaged region. This first phase is characterized by myofiber necrosis and tissue inflammation, as well as initial fibrosis. Satellite cells will start to proliferate at the beginning of the regeneration phase, while M2 (anti-inflammatory) macrophages will promote their differentiation. Other cell types as fibroblasts and fibro-adipogenic progenitors (FAPs) will start to remodel a temporary extra-cellular matrix (ECM) that will be subjected to further refinement during the remodelling phase by the action of metalloproteinases (MMPs) (Figure from Mahdy 2018) (Mahdy 2018)..... 4

Figure 4- Hematoxylin-eosin (HE) staining of uninjured, cardiotoxin or glycerol-damaged tibialis anterior (TA) muscle cross-sections. In this figure the structural changes between an uninjured, a cardiotoxin (CTX, B, D, F, H) and glycerol-treated (C, E, G, H) muscle are shown. To note the infiltration of monocytes at day 4 (evident in the CTX model, B) and the presence of center-nucleated fibers (arrows) in both models at day seven, ten and fourteen after the damage procedure was administered. Scale bar: 50 μ m (figure from Mahdy, 2014)..... 6

Figure 5- Schematic representation of a regenerating skeletal muscle fiber. (A) Normal muscle fiber with myonuclei (dark) and satellite stem cells (grey nuclei, white cytosol). Upon sensing damage to the muscle fiber (B), satellite cells proliferate and migrate in the interested area. At this stage they will start their differentiation. After they align along the direction of the future muscle fiber (C) they will further differentiate into myotubes, who will present transiently center-positioned nuclei (D) (figure from Morgan and Partridge, 2003) (Morgan and Partridge 2003)..... 8

Figure 6- NMJ tripartite structure and the proteins involved in its development and maintenance. In (A) a scheme depicting the NMJ structure is shown, in (B) the different proteins leading to NMJ maturation, organization and maintenance are listed and show in respect to their association to each other. Figure from Campanari et al. (Campanari et al. 2016)..... 12

Figure 7- Transmission of the neural stimuli ending in muscle contraction. Acetylcholine (ACh) released in the synaptic cleft from the nerve terminal binds to its receptor (AChR),

triggering the transient opening of the cation channel of the receptor (1) and the influx of small cations, that gives rise to a synaptic potential. This localized change in membrane potential leads to the activation of voltage-gated sodium channels, eliciting an action potential (2) that propagates along the myofiber. Once this stimulus reaches the T-tubules (transverse tubules, extensions of the muscle fiber membrane containing a large number of ion channels that reach into the center of the myofiber), voltage-dependent calcium channels open and trigger ryanodine receptors in the sarcoplasmic reticulum (SR) to release calcium ions (3). Calcium then binds to troponin (4), leading to the exposition of binding sites for myosin on the actin filament. Myosin is bound by adenosine diphosphate (ADP) and phosphate (Pi) and forms cross-bridges with actin. The subsequent release of ADP and Pi will generate the stroke that causes the sliding of the thin filament past the thick filament, resulting in muscle contraction (5). 13

Figure 8- Scheme depicting NMJ development. In (A) is showed how the motoneuron, approaching the muscle iber, leads to NMJ formation, in particular (B) by promoting AChR accumulation at the future postsynaptic site. In (C) the effect of agrin is schematized: upon its binding to MuSK it promotes MuSK phosphorylation, leading to its association with rapsyn and AChR accumulation. Figure modified from Sanes and Lichtman (Sanes and Lichtman 2001). 15

Figure 9- NMJ fragmentation in a wild type (WT) and in a mdx mouse. The motoneuron is detected using an antibody against neurofilament (purple), the presynapse with one against synaptophysin (green) and the postsynapse by using a BTX coupled with a fluorophore. Is clear how the NMJ in the mdx mouse is fragmented respect to the healthy ones in the wild type. Scale bar: 10 μ m. Figure from Pratt et al. (S. J. P. Pratt et al. 2015). 17

Figure 10- Classification of clearing protocols. The most common taxonomy divides the different methods for tissue clearing in four groups, depending on which mechanism they applied to obtain tissue transparency. Figure from Silvestri, 2016 (Silvestri et al. 2016). 18

Figure 11- Representative figures of the results obtained with organic solvent-based tissue clearing protocols. Results on mouse brain transparency achieved with different organic solvent based methods (A, different methods as indicated in figure) and in the fluorescent signal preservation (B) of FDISCO respect to 3DISCO protocol (B, methods as indicated in figure, EYFP as endogenous yellow fluorescent protein). Figure adapted from Qi et al., 2019. 19

Figure 12- CLARITY pipeline for a mouse brain. The tissue sample is perfused with a formaldehyde and acrylamide solution containing the thermal initiator as well. After the polymerization, the sample will be embedded in a meshwork of fibers preserving its structural and biological identity. A membrane lipid removal phase (passive or with the use of an electrophoretic chamber, ETC) follows to achieve tissue transparency. The resulting sample will be then labelled and imaged with light microscopy. To note that the data analysis and management phase as to be taken into account, as the volume of sheer data obtained can go from few Gb to ~1 Tb: a dedicated virtual infrastructure for data handling, segmentation and storage could be necessary. Image from Tomer et al. (Tomer et al. 2014). 20

Figure 13- Results on NMJs visualization and segmentation in a murine EDL muscle with MYOCLEAR. EDL muscles from wild type (wt) and mdx mice were cleared using the MYOCLEAR protocol and then stained with BGT linked to a fluorophore to study postsynapse number, position, shape and structure. NMJs were successfully identified through the entire EDL (A,B) and their structure was clearly conserved, with mdx NMJs presenting

the fragmentation as expected (A', B'). When parameters describing NMJs structure were measured from different areas of the same muscle, and heterogeneity was found (C, E). Figure modified from Williams et al. (Williams et al. 2019)..... 22

Figure 14- Scheme showing the different cell types that could be obtained by adipose-derived mesenchymal stem cells. Figure from Si, 2019 (Si et al. 2019). 23

Figure 15-Successful glycerol injection in the tibialis anterior leads hindlimb contraction. In the upper panel (A), mice hindlimbs are showed before the treatment, in the lower panel (B) the same mice are showed less than a minute after 50% glycerol solution (right hindlimb) or saline (left hindlimb) injection. The contraction in the glycerol-treated limb is evident. 27

Figure 16- Scheme of the experimental design for the glycerol-induced muscle damage model. The days indicated start from the glycerol injection day (Day 0). 20 µl of 50% glycerol solution in saline solution were injected intra-muscle (i.m.). When adipose-derived stem cells (ASCs) treatment was applied, 1×10^6 cells resuspended in 100 µl of sterile PBS were systemically applied via tail vein (t. v.) soon after the glycerol injection was performed. Following dissection (Sample collection), TA muscles were snap-frozen in liquid nitrogen and embedded in OCT. Soon after cryosections from those muscles were obtained and subjected to immunofluorescence (IF) analysis in order to quantify both muscle damage and its recovery, along with the status of the endplates. When glycerol injection without the stem cell treatment was analyzed, samples were collected three, five, eight and eleven days after the injection. Where ASCs were applied, the days considered for sample collection were three, five and eleven days after the injection. 28

Figure 17- Scheme representing the different phases of the MYOCLEAR protocol. Hydrogel embedding phase last from day 2 to day 7, staining from day 8 to day 15, RI matching from day 16 to 17. It has to be considered that, where needed, a second washing step and dye incubation step are needed if primary and secondary antibodies are used, increasing the procedure time by 7 days. 31

Figure 18- Glycerol injection leads to structural damage to muscle fibers within 18 hours from the treatment. After either glycerol or saline solution injection, TA muscles were harvested 18 hours after the treatment and snap-frozen. Subsequently, cryosections were obtained and stained with mouse immunoglobulin G antibody, phalloidin (both coupled with a fluorophore) and anti-dystrophin antibody. Treated muscles (18 hrs p.i., on the right) show serum proteins uptake (mIgG) in the cytosolic space, indicating necrosis, along with loss of dystrophin and actin respect to the contralateral muscles (CTRL, on the left). Scale bar: 100µm..... **Error! Bookmark not defined.**

Figure 19- Glycerol induced muscle damage is characterized by necrosis and loss of dystrophin and actin, followed by a transient expression of eMHC and the increase in center-nucleated fibers. Representative optical sections of fluorescent signals as indicated (A), nuclear DAPI staining always shown in blue, mIgG in yellow, collagen I and eMHC in red, dystrophin in green, actin in grey. CTRL indicates muscle injected with saline three days post-injection, while the other panels show TA sections at three, five and eleven days after glycerol treatment. (B) Quantitative analysis of section areas positive for fluorescence signals of either mIgG, collagen I, dystrophin, or actin, or number of eMHC-positive fibers, as a function of days p.i. Box-Whisker plots show all individual data points as dots, the extensions of upper and lower quartiles in the boxes, the medians as horizontal lines in the boxes, and

maxima and minima as whiskers. * $p \leq 0.05$, ** $p \leq 0.01$, *** $p \leq 0.001$. (C-D) Quantitative analysis of fibers per muscle slice (C) or center-nucleated fibers (% of fiber number, D) as a function of days p.i. Box-Whisker plots show all individual data points as dots, the extensions of upper and lower quartiles in the boxes, the medians as horizontal lines in the boxes, and maxima and minima as whiskers. ** $p \leq 0.01$, *** $p \leq 0.001$. Scale bar: 100 μm 35

Figure 20- Glycerol induced muscle damage is characterized by necrosis and loss of dystrophin and actin, followed by a transient expression of eMHC and the increase in center-nucleated fibers. Representative optical sections of fluorescent signals as indicated, nuclear DAPI staining always shown in blue, mIgG in yellow, collagen I and eMHC in red, dystrophin in green, actin in grey. CTRL indicates muscle injected with saline three days post-injection, while the other panels show TA sections at three, five and eleven days after glycerol treatment. Scale bar: 500 μm 39

Figure 21-Glycerol treatment affects differently pre- and postsynapses. Representative images of the localization of AChR (in green) and VACHT (in red) and their overlay in TA muscle cross section (A) at different timepoints (The sham procedure three days after the injection indicated as sham, the other timepoints as in the amount of days post-injection (p.i.)). Scale bar: 100 μm . Quantitative analysis of AChR+ sites (B) present per cryosection and percentage of how many of them were positive for VACHT as well (C). Shown is mean \pm SEM (n = 3 muscles). * $p \leq 0.05$, ** $p \leq 0.01$ 41

Figure 22- AChR+ VACHT- sites were identified in highly necrotic areas as well as in unaffected regions. Postsynaptic sites were found in necrotic areas of the muscle. When considered if that could be the reason they were negative for VACHT, negative postsynaptic sites for presynapses presence were also observed in non-necrotic areas. Scale bar: 50 μm .. 43

Figure 23- ASCs systemic application leads to mIgG infiltration, enhanced eMHC basal expression and increase in the center-nucleated fibers. Representative optical sections of fluorescent signals as indicated (A), nuclear DAPI staining always shown in blue, mIgG in yellow, collagen I and eMHC in red, dystrophin in green, actin in grey. CTRL indicates muscle injected with saline three days post-injection, while the other panels show TA sections at three, five and eleven days after glycerol treatment. (B) Quantitative analysis of section areas positive for fluorescence signals of either mIgG, collagen I, dystrophin, or actin, or number of eMHC-positive fibers, as a function of days p.i. Box-Whisker plots show all individual data points as dots, the extensions of upper and lower quartiles in the boxes, the medians as horizontal lines in the boxes, and maxima and minima as whiskers. * $p \leq 0.05$, ** $p \leq 0.01$, *** $p \leq 0.001$. (C-D) Quantitative analysis of fibers per muscle slice (C) or center-nucleated fibers (% of fiber number, D) as a function of days p.i. Box-Whisker plots show all individual data points as dots, the extensions of upper and lower quartiles in the boxes, the medians as horizontal lines in the boxes, and maxima and minima as whiskers. ** $p \leq 0.01$, *** $p \leq 0.001$. Scale bar: 100 μm 44

Figure 24- ASCs systemic application leads to mIgG infiltration, enhanced eMHC basal expression and increase in the center-nucleated fibers. Representative optical sections of fluorescent signals as indicated (A), nuclear DAPI staining always shown in blue, mIgG in yellow, collagen I and eMHC in red, dystrophin in green, actin in grey. CTRL indicates muscle injected with saline three days post-injection, while the other panels show TA sections at three, five and eleven days after glycerol treatment. Scale bar: 500 μm 46

Figure 25- ASCs enhance recovery of presynapses at early stages, but such effect is not present at late time point. As soon as TA muscles were injected with either saline or 50% glycerol solution, mice were injected via tail-vein with ASCs. TA muscles were then harvested and immediately snap-frozen three, five or eleven days after the injection (days p.i.). After cryosectioning, muscle sections were stained with α BGT (marking AChR) and antibodies against VAcHT to label post- and presynaptic portions of NMJs, respectively. Cryosections were then analyzed with confocal microscopy. (A) Representative images of fluorescence signals as indicated, AChR in green, VAcHT in red, in overlay images yellow indicates the colocalization of both signals. Saline-injected muscles at 3 days p.i. indicated as CTRL, while the other panels show representative images from glycerol-injected muscles at three, five and eleven days post-injection. Scale bar: 100 μ m. (B-C) Quantitative analysis of AChR+ post-synaptic sites present per section (B) and of VAcHT+ NMJs (as percentage of VAcHT+ structure, C) as a function of days after the treatment. Shown is mean \pm SEM (n = 3 muscles). * p \leq 0.05, ** p \leq 0.01. 48

Figure 26-Integration of systemically injected ASC into muscle is not detectable by immunofluorescence. Isolated human ASC and mouse TA muscle sections taken five days post injection of either saline or glycerol (indicated) were stained with DAPI and an anti-human Ku80 antibody against DNA and human nuclei, respectively. (A) Representative confocal micrographs showing fluorescence signals of DAPI and human Ku80 in blue and green, respectively. (B) Quantitative analysis of the percentage of human Ku80+ signals found in DAPI+ nuclei. 50

Figure 27- eMHC is not present in saline-injected muscles and postsynaptic structure is preserved. Five days after saline injection, TA muscle was dissected and cleared using the MYOCLEAR procedure and then immunostained with anti-eMHC antibody (subsequently coupled with a fluorophore-conjugated secondary antibody) and a fluorophore-conjugated α -BGT. (A) 3D images of saline-injected TAs. Autofluorescent background (Autofluo) signal in the 488 nm channel was used to highlight the muscle structure and is shown in green, eMHC in red and presence of AChR in white. No constitutive expression of eMHC was observed in this sample. Scale bar: 1 mm. (B) Magnification of the postsynaptic structures showed the preservation of their classical pretzel-like shape, without any sign of fragmentation. 52

Figure 28- eMHC expression in glycerol-injected TA, postsynaptic structure is preserved. Five days after glycerol injection, TA muscle was dissected and cleared using the MYOCLEAR procedure and then immunostained with anti-eMHC antibody (subsequently coupled with a fluorophore-conjugated secondary antibody) and a fluorophore-conjugated α -BGT. (A) 3D images of saline-injected TAs. Autofluorescent background (Autofluo) signal in the 488nm channel was used to highlight the muscle structure and is shown in green, eMHC in red and presence of AChR in white. Strong presence of eMHC was observed in this sample. Scale bar: 1mm. (B) Magnification of the postsynaptic structures showed the preservation of their classical pretzel-like shape, without any sign of fragmentation. 53

Figure 29- Post-synapses structure is conserved in the glycerol-treated muscles three days after the injection. Three days after glycerol injection, TA muscles were dissected and cleared using the MYOCLEAR procedure and then immunostained with an anti-mouse mIgG antibody fluorophore-conjugated secondary antibody (mIgG, in green) and a fluorophore-conjugated α -BGT (AChR, in red) together with a DAPI to detect cell nuclei (in blue). Confocal tile-scans were then taken and analyzed. (A) 3D images of TA muscle injected with saline, in the magnification is possible to appreciate the post-synapse pretzel-shaped structure. (B) 3D images of TA muscle injected with glycerol, in the magnification is possible to

appreciate a similar post-synaptic structure as the one detected in the control. Scale bar: 100 μ m..... 54

Figure 30- Schematic summary of glycerol injection with or without ASCs systemic application on skeletal muscle tissue. The bars indicate the presence of markers as labeled, with the bar width indicating the amount. mIgG was used to quantify muscle necrosis and inflammation, while collagen I to quantify fibrotic tissue deposition. The number of VAcHT+ NMJs is referred to the percentage of colocalized VAcHT signals on the total of the AChR+ signals detected. 58

List of publications



Effects of ASC Application on Endplate Regeneration Upon Glycerol-Induced Muscle Damage

Matteo Rigon¹, Sarah Janice Hörner¹, Tatjana Straka¹, Karen Bieback², Norbert Gretz^{3,4}, Mathias Hafner^{1,4} and Rüdiger Rudolf^{1,4,5*}

¹Institute of Molecular and Cell Biology, Mannheim University of Applied Sciences, Mannheim, Germany, ²Institute of Transfusion Medicine and Immunology, Medical Faculty Mannheim, Heidelberg University, Mannheim, Germany, ³Medical Research Center, Medical Faculty Mannheim, Heidelberg University, Mannheim, Germany, ⁴Institute of Medical Technology, Medical Faculty Mannheim, Mannheim University of Applied Sciences, Mannheim, Germany, ⁵Interdisciplinary Center for Neurosciences, Heidelberg University, Heidelberg, Germany

OPEN ACCESS

Edited by:

Hanns Lochmüller,
University of Ottawa, Canada

Reviewed by:

Claire Legay,
Université Paris Descartes, France
Mohammed Akaaboune,
University of Michigan, United States

*Correspondence:

Rüdiger Rudolf
r.rudolf@hs-mannheim.de

Received: 25 January 2020

Accepted: 20 May 2020

Published: 23 June 2020

Citation:

Rigon M, Hörner SJ, Straka T, Bieback K, Gretz N, Hafner M and Rudolf R (2020) Effects of ASC Application on Endplate Regeneration Upon Glycerol-Induced Muscle Damage. *Front. Mol. Neurosci.* 13:107. doi: 10.3389/fnmol.2020.00107

Amongst other approaches, adipose-derived stromal cells (ASCs) have recently been tested with respect to their regenerative capacity for treatment of neuromuscular disorders. While beneficial effects of ASCs on muscle recovery were observed previously, their impact on regeneration of neuromuscular junctions (NMJs) is unclear. Here, we used a murine glycerol damage model to study disruption and regeneration of NMJs and to evaluate the effects of systemic application of ASCs on muscle and NMJ recovery. In mice that were not treated with ASCs, a differential response of NMJ pre- and post-synapses to glycerol-induced damage was observed. While post-synapses were still present in regions that were necrotic and lacking actin and dystrophin, pre-synapses disappeared soon in those affected areas. Partial regeneration of NMJs occurred within 11 days after damage. ASC treatment slightly enhanced NMJ recovery and reduced the loss of presynaptic sites, but also led to a late phase of muscle necrosis and fibrosis. In summary, the results suggest a differential sensitivity of NMJ pre- and post-synapses to glycerol-induced muscle damage and that the use of ASC for the treatment of neuromuscular disorders needs further careful evaluation.

Keywords: glycerol, skeletal muscle, NMJ, ASC, regeneration

INTRODUCTION

Despite decades of research and numerous trials, the treatment options for most neuromuscular disorders are still disappointing. While the number of drugs approved or in clinical trials has strongly risen in the past decade (Cowling and Thielemans, 2020) the development of stem-cell based therapies is another important line of activity in this context. The hope is, that stem cells might enable direct tissue regeneration *in vivo* (Gois et al., 2019). At present, different stem cell sources are being tested, including autologous or heterologous muscle-derived stem

cells, mesangioblasts, muscle-derived progenitors, interstitial cells, and mesenchymal stromal/stem cells (Gois et al., 2019). The latter group includes adipose-derived stromal cells (ASCs), that are interesting as a source of stem cells, because besides being immune-privileged they are readily accessible from lipoaspirates and can be easily isolated and expanded in vitro (Kern et al., 2006; Torres-Torrillas et al., 2019). It remains open whether their local or systemic application might be more beneficial for the treatment of neuromuscular disorders. While local injection might come with a higher potential for targeted cell integration, it is difficult to achieve for diseases where different organs or large parts of the body are affected, as it is true for most neuromuscular disorders (Gois et al., 2019). On the other hand, while systemic application might have a drawback in the entrapment of most injected cells in organs such as lungs and liver (Gois et al., 2019) recent studies suggest that a principal function of stem cell therapies relies in their modulatory activities on cellular signaling rather than direct cell engraftment (Gorecka et al., 2018; Boldyreva et al., 2019; Mitchell et al., 2019; Torres-Torrillas et al., 2019). Although in different animal models and clinical applications beneficial effects of stem cell grafts on recovery of muscle tissue were reported (Forcales, 2015; Torres-Torrillas et al., 2019), little emphasis has been put on their impact at the level of the neuromuscular junction (NMJ).

In order to study skeletal muscle recovery mechanisms, several muscle damage models have been developed (Arnold et al., 2007; McCarthy et al., 2011; Czerwinska et al., 2012; Iwata et al., 2013; Tiryakioglu et al., 2015; Hardy et al., 2016; Mahdy, 2018). Those models differ in the injury mechanism and in the type of harm caused, affecting the degrees of degeneration and regeneration capabilities of the muscle. Among those, glycerol was reported to cause a damage by osmotic shock, affecting not only myofibers but also other muscle elements, including the basal lamina (Kawai et al., 1990; Pisani et al., 2010; Mahdy et al., 2015). This leads to an impaired regeneration with ectopic infiltration of adipocytes and fibrosis (Lluís et al., 2001; Mahdy et al., 2015, 2016; Hardy et al., 2016) and deprives the regenerating muscle cells of the interaction with extracellular matrix (ECM) elements that can enhance tissue recovery (Murphy et al., 2011; Iwata et al., 2013; Webster et al., 2015). Although characterized by a severe initial destruction, muscles treated with intra-muscular glycerol injection are able to recover anyway (Arsic et al., 2004; Mahdy et al., 2015, 2016). This suggested that glycerol injection might be a model well suited for the study of muscle regeneration. Accordingly, to investigate de- and regeneration of NMJs in the absence and presence of systemic ASC administration, a glycerol-induced muscle damage model was chosen. Upon toxin- or chemical-induced injury, muscle necrosis and fibrosis take place. Necrotic muscle cells, due to their compromised plasma membrane, allow the uptake of serum proteins, including immunoglobulins, into the cytosol (Iwata et al., 2013; Judson et al., 2013; Proto et al., 2015; Arecco et al., 2016; Rodrigues et al., 2016), rendering immunofluorescence against immunoglobulin G (mIgG) useful to identify necrotic areas. Necrotic leakage and linked degradative processes can also lead to the loss of dominant cytosolic skeletal

muscle proteins, such as f-actin (Huang and Gopalakrishnakone, 1996) and dystrophin (Biral et al., 2000). Muscle fibrosis is characterized by deposition of collagen type I (Gibertini et al., 2014), one of the major components of ECM (Huebner et al., 2008; Serrano and Muñoz-Cánoves, 2010; Gillies and Lieber, 2011; Feng et al., 2019). Following muscle degeneration, muscle recovery involves detection of regenerating myofibers, which are characterized by the expression of embryonic myosin heavy chain (eMHC, also known as myosin 3) (Schiaffino et al., 1986; Murphy et al., 2011; Judson et al., 2013; McDonald et al., 2015; Kastenschmidt et al., 2019) and by nuclei in central position (in the following, referred to as center-nucleated fibers, CNFs) (Judson et al., 2013; McDonald et al., 2015; Arecco et al., 2016; Kastenschmidt et al., 2019). In order to monitor NMJ degradation and recovery, markers for pre- and post-synapses were analyzed. While vesicular acetylcholine transporter (VACHT) is localized to small synaptic vesicles at the endplate terminal (Maeda et al., 2004; Sugita et al., 2016), acetylcholine receptor (AChR) is highly enriched at the postsynaptic membrane of NMJs (Fambrough et al., 1979).

The present study aimed at developing and characterizing a reliable glycerol-based de/regeneration model and to apply this for the analysis of potential effects of ASCs on regeneration of muscle and NMJs. Using the glycerol damage paradigm, we obtained differential profiles for pre- and postsynaptic destruction and recovery. While post-synapses appeared to remain relatively stable even upon heavy muscle fiber damage and loss of internal structures, presynaptic contacts were severely affected upon glycerol injection and needed to recover over a couple of days. Treatment with ASCs led to a slightly reduced loss of post-synapses and improvement of pre- to postsynapse match upon glycerol treatment, but these intermediate effects were reverted during a second phase of inflammation.

MATERIALS AND METHODS

Glycerol and Stem Cell Injection

All animal experiments were conducted in accordance with the German Animal Protection Law and approved by the local authority (Regierungspräsidium Nordbaden, Karlsruhe/Germany in agreement with EU guideline 2010/63/EU; license G-139/18). In order to induce muscle damage, 20 μ l of a 50% glycerol solution diluted in physiological saline were injected into the tibialis anterior (TA) muscle of anesthetized 2 months old C57BL6 female mice. The decision to use female arose from two observations: first, females are experimentally easier to handle, since animals should preferentially be kept in groups for social interactions, but males under these circumstances often bite each other and this can lead to damage of muscles that is not due to the experimental protocol. Second, females seem to possess a slightly better regenerative capability (Deasy et al., 2007; Kitajima and Ono, 2016). The same volume of saline solution was injected contralaterally as a sham. The animals were then euthanized by cervical dislocation after 18 h or 3, 5, 8, or 11 days following the procedure and the

muscles were dissected. Where ASCs were applied, one million cells diluted in 100 μ l of sterile PBS were injected via tail vein directly after glycerol treatment. In this case, animals were euthanized by cervical dislocation and dissected 3, 5, and 11 days after the injection. At least three animals for each timepoint and condition (glycerol and ASC with glycerol) were analyzed.

Human Adipose-Derived Mesenchymal Stem Cells

Adipose-derived stromal cells were isolated from adult adipose tissue obtained from lipoaspirates of healthy donors, after obtained informed consent (Mannheim Ethics Commission II vote numbers 2010-262 N-MA, 2009-210 N-MA, 49/05 and 48/05), as described before (Bieback et al., 2012). Briefly, the lipoaspirate was washed with sterile PBS to remove cellular debris and red blood cells and digested with 0.15% w/v collagenase type I (Sigma-Aldrich, Munich, Germany), for 45 min at 37°C. After washing, the pellet was resuspended in medium (DMEM low glucose, 10% human AB serum, 100 U/ml penicillin, 0.1 mg/ml streptomycin and 4 mM L-glutamine), plated and incubated overnight at 37°C, 5% CO₂. After 1 day, the non-adherent and red blood cells were removed. Expanded cells were characterized regarding their proliferation capacity, immune phenotype, and adipo- and osteogenic differentiation potential, as described previously (Bieback et al., 2012). Before injection, ASCs were seeded at 750 ASC/cm² and expanded. On injection days, ASCs were trypsinized for 5 min at 37°C and washed once with medium. The ASC pellet was then resuspended in sterile PBS at a concentration of 1×10^7 cells/ml shortly before the injection.

Immunofluorescence Analysis

Freshly after dissection, TA muscles were covered with a thin layer of Frozen Section Compound (Leica) and frozen on

liquid nitrogen. Transverse cryosections of 15–20 μ m thickness were cut using a Leica CM1950 cryostat, carefully positioned on glass microscope slides (Thermo Fisher Scientific) and then immunostained for epitope detection. Cryosections were permeabilized with 0.1% TritonX-100/PBS for 10 min at room temperature and, after three washing steps in PBS (5 min each), incubated with 2% BSA/PBS for 2 h to avoid unspecific binding of primary antibodies. The sections were then incubated overnight at +4°C with primary antibodies diluted in 2% BSA/PBS. After three washing steps in 2% BSA/PBS, sections were incubated with the secondary antibodies/dyes/toxins in 2% BSA/PBS for 3 h at room temperature and in the darkness. Antibodies, dyes, and dilution rates are listed in Table 1. Subsequently, after 15 min incubation with DAPI (Sigma) in 2% BSA/PBS and three more washing steps with PBS, glass slides were left to briefly dry and then mounted in Mowiol. The samples were then analyzed at the confocal microscope the day after. Images were taken using a Leica TCS SP8 microscope equipped with 405, 488, 555, and 633 nm lasers, and Leica HC PLAN APO 20 \times /0.75 IMM CORR CS2 objective and at z-steps of 3 μ m. For every sample, three to five entire cryosections from the central portion of the muscle at an intersection interval of roughly 200 μ m were visualized. Staining of ASCs used a slightly modified protocol as follows. Cells on Eppendorf 8 chamber cell imaging slides were briefly fixed with 2% PFA/PBS and then permeabilized with 0.1% TritonX-100/PBS for 5 min at room temperature and, after three washing steps in PBS (5 min each), incubated with 2% BSA/PBS for 1 h. Subsequently, cells were incubated overnight at 4°C with primary antibody diluted in 2% BSA/PBS. After three washing steps in 2% BSA/PBS, cells were incubated with the secondary antibody and DAPI diluted in 2% BSA/PBS for 45 min and in the darkness. After three more washing steps with PBS and one with ddH₂O, the slides were mounted in Mowiol and analyzed using the same microscope and objective used for the muscle

TABLE 1 | List of used antibodies and dyes.

| | Company | Catalog number | Lot number | Dilution rate |
|--|--------------------------|-----------------|------------|---------------|
| Primary antibody | | | | |
| Anti-Dystrophin antibody | Invitrogen | PA 1-21011 | TK2665551J | 1:200 |
| Anti-Myosin 3 antibody | Biorbyt | orb395438 | RBQ34 | 1:100 |
| Anti-VACHT antibody | Synaptic Systems | 139 103 | 2-44 | 1:500 |
| Anti-Collagen type I antibody | Rockland | 600-401-103-0.1 | 40681 | 1:500 |
| Recombinant anti-Ku80 antibody (EPR3468) | Abcam | GR3216586-3 | ab80592 | 1:300 |
| Secondary antibody/marked toxins/dyes | | | | |
| Donkey anti-Rabbit IgG (H + L) Highly Cross-Adsorbed Secondary Antibody, Alexa Fluor 488 | Thermo Fisher Scientific | A-21206 | 176375 | 1:500 |
| Donkey anti-Rabbit IgG (H + L) Highly Cross-Adsorbed Secondary Antibody, Alexa Fluor 488 | Thermo Fisher Scientific | A-21206 | 176375 | 1:500 |
| Goat anti-Rabbit IgG (H + L) Cross-Adsorbed ReadyProbes Secondary Antibody, Alexa Fluor 594 | Thermo Fisher Scientific | R37117 | 1875978 | 1:500 |
| F(ab') ₂ -Goat anti-Rabbit IgG (H+L) Cross-Adsorbed Secondary Antibody, Alexa Fluor 647 | Thermo Fisher Scientific | A-21246 | 55002A | 1:500 |
| Goat anti-Mouse IgG (H + L) Highly Cross-Adsorbed Secondary Antibody, Alexa Fluor 555 | Thermo Fisher Scientific | A-21424 | 1802436 | 1:500 |
| Goat anti-Mouse IgG (H + L) Cross-Adsorbed Secondary Antibody, Alexa Fluor 488 | Thermo Fisher Scientific | A-11001 | 1834337 | 1:500 |
| α -Bungarotoxin, Alexa Fluor 488 conjugate | Thermo Fisher Scientific | B13422 | 1750294 | 1:500 |
| α -Bungarotoxin, Alexa Fluor 555 conjugate | Thermo Fisher Scientific | B35451 | 1880574 | 1:500 |
| Alexa Fluor 555 Phalloidin | Thermo Fisher Scientific | A34055 | 1780358 | 1:500 |
| DAPI | Sigma-Aldrich | D9542 | 28114320 | 1:1000 |

cryosections. Antibodies, dyes, and dilution rates are listed in **Table 1**.

Semi-Automated Quantification

Confocal images obtained from muscles cryosections were processed and analyzed using ImageJ (Fiji version). From maximum projections of the images, areas which showed the presence of mIgG, collagen I, or actin were manually thresholded, areas selected and measured. The entire area of the cryosection was contoured by hand using the background signal. The areas where dystrophin-outlined cells were present were obtained from maximum projected confocal images to which a median filter was applied and then thresholded. Subsequently the “analyze particles” function of ImageJ was used (selecting 20 μm as lowest value and including holes). The image obtained was then measured. Muscle fibers, CNFs, and eMHC+ fibers were counted manually. For each sample, a minimum of three cryosections was processed and analyzed. NMJs, identified by AChR and VAcHT expression together with their shape and/or position with respect to muscle fibers, were analyzed and quantified manually. Where indicated, the areas positive for AChR and/or VAcHT (per endplate) were thresholded, segmented and measured. Numbers of analyzed synapses are given in **Supplementary Table S1**. Signals for pre- and post-synapses obtained from three different cryosections per sample were analyzed. For the Ku80 detection, DAPI signals corresponding to cell nuclei were thresholded and segmented. A selection created from those signals was then used to hand-segment the Ku80+ signals, selecting those areas where it was colocalizing within cell nuclei.

Statistical Analysis and Figure Compilation

For statistical analysis, data were first screened for normality and homoscedasticity using Kolmogorov–Smirnov test and F-test. Mean and SD/SEM were calculated. Then, significance was assessed with Student's *t*-test or Welch test. Data compilation was done in Microsoft Excel for Mac, plots were made using either Microsoft Excel for Mac or Graph Pad Prism. Figures were prepared in Adobe Photoshop and then compiled in Adobe Illustrator.

RESULTS

Glycerol Injection Leads to Robust Muscle Necrosis With Fast Regeneration

To understand the effects of glycerol injection on muscle integrity and regeneration, a panel of markers for muscle necrosis, function, and regeneration was analyzed. Therefore, TA muscles were injected with 20 μl of either saline (control) or glycerol and then muscles were harvested after 18 h and 3, 5, 8, and 11 days. Sliced muscles were co-stained with DAPI for nuclei and antibodies against mouse IgG, collagen I, dystrophin, or eMHC to assess the status of necrosis, fibrosis, muscle fiber integrity, and regeneration. Co-staining with phalloidin served to visualize the presence of f-actin. Confocal images of these sections

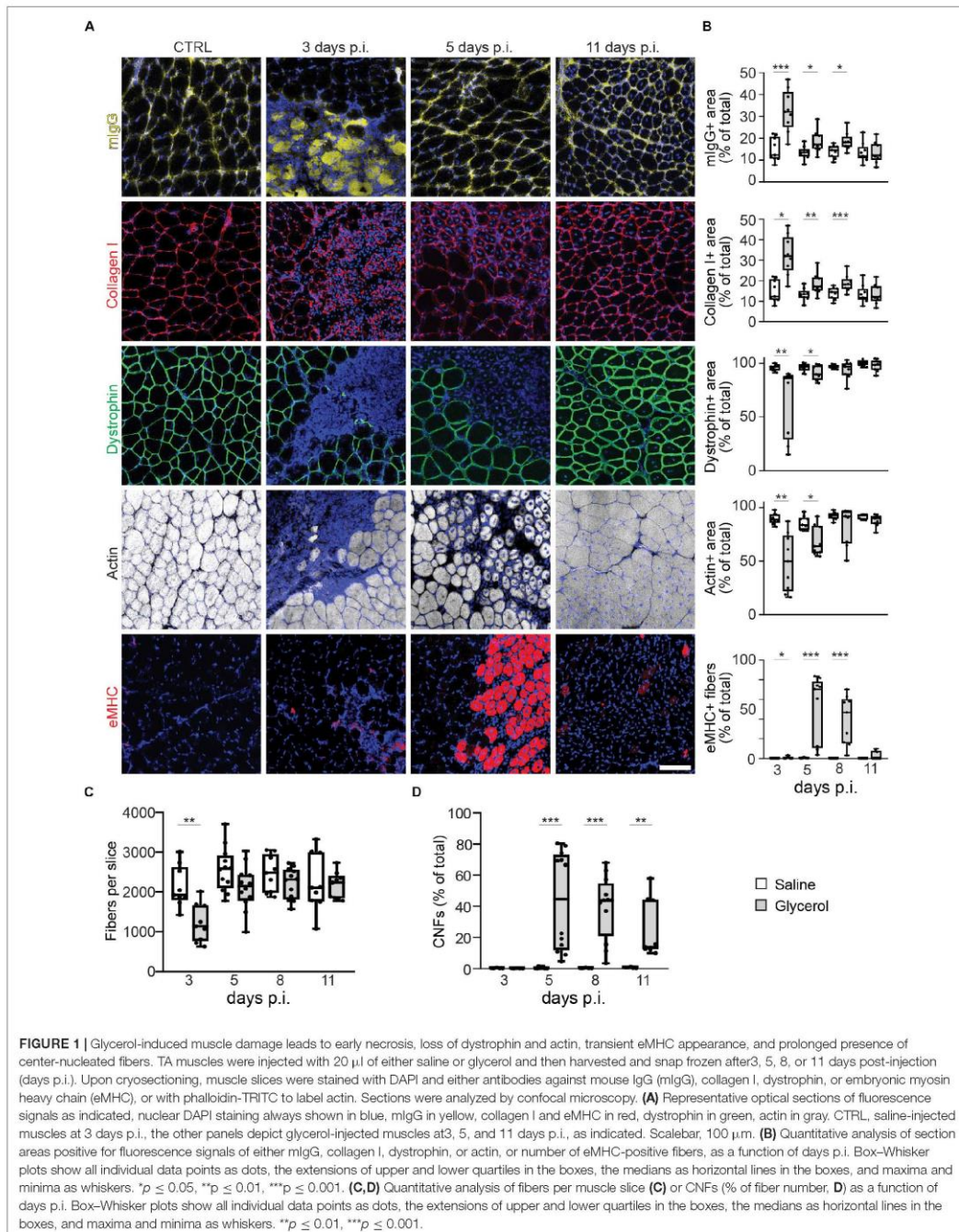
revealed a massive muscle damage already after 18 h of glycerol injection (**Supplementary Figure S1**). As shown in **Figure 1** and **Supplementary Figure S2**, after 3 days of injury due to glycerol injection involved large parts of muscles and was characterized by passage of immunoglobulins through sarcolemma, enhanced accumulation of collagen I, and loss of the functional markers, dystrophin and f-actin. Subsequently, these signs of muscle damage progressively decreased and were followed by a wave of eMHC expression, principally between days 5 and 8 after glycerol injection. On day 11 after glycerol treatment, muscles had largely reassumed their normal appearance lacking degeneration and regeneration markers and showing regular distribution of dystrophin and f-actin. Also, numbers of muscle fibers, that were significantly decreased on day 3 post glycerol injection, were comparable to saline-treated muscles at day 11 (**Figure 1C**). Cross-sectional areas of remaining fibers did not vary between the different experimental groups (**Supplementary Table S2**). The only clear sign of ongoing muscle regeneration at 11 days post injection was the presence of CNFs that rose from less than 1% in control conditions to around 40% on days 5 and 8 after glycerol injection and decreased to roughly 25% on day 11. In summary, the glycerol injection paradigm displayed a simple, regular, and controlled sequence of muscle damage and regeneration. In the following, we used this model to address NMJ degeneration and regeneration.

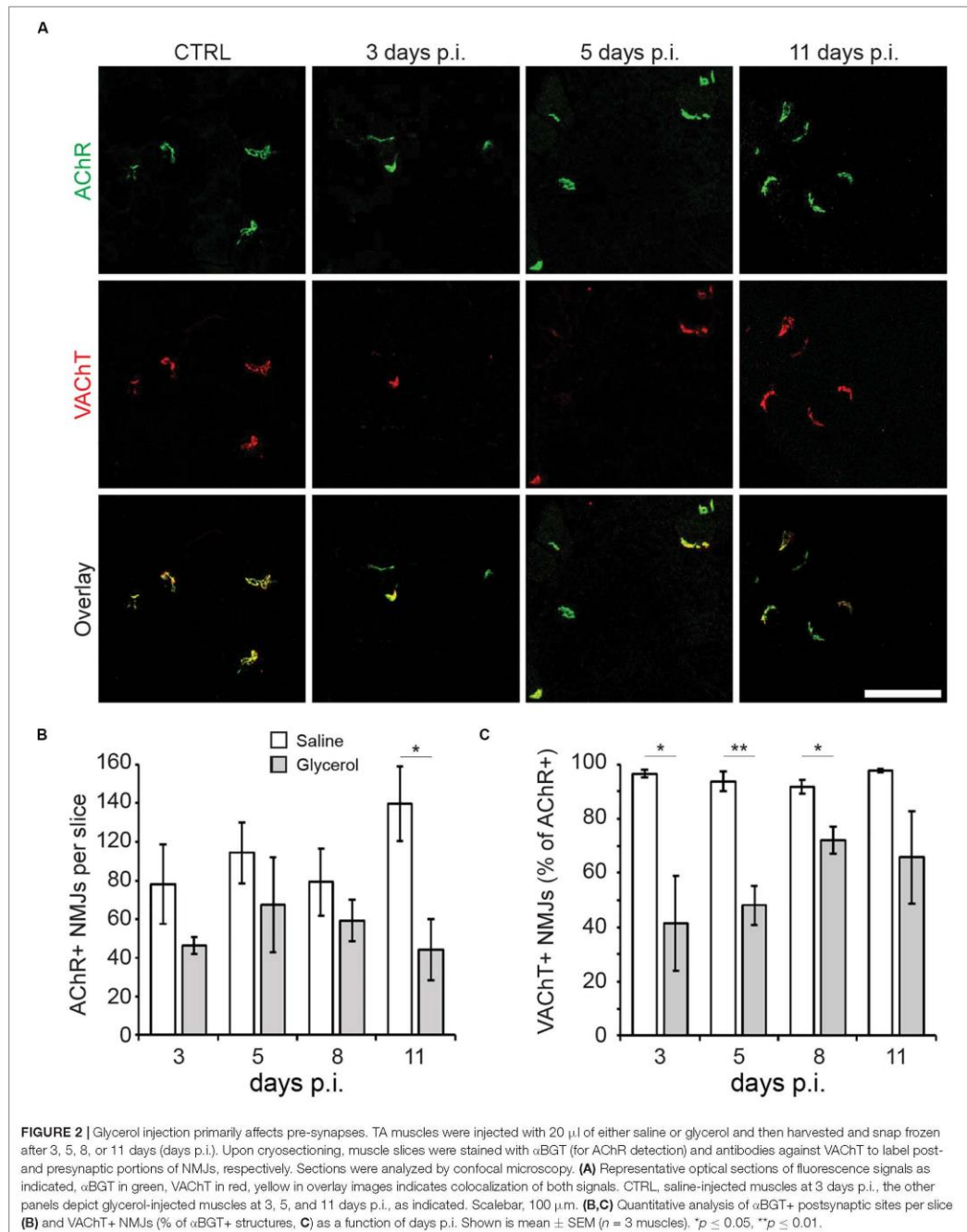
Glycerol Injection Induces a Transient Loss of Pre-synapses

To visualize the effect of glycerol injection on NMJs, TA muscles injected with either glycerol or saline (control) were taken at days 3, 5, 8, and 11 after injection. Slices were stained against postsynaptic nicotinic AChR and presynaptic VAcHT with fluorescent α -bungarotoxin (α BGT) and anti-VAcHT antibody, respectively. Confocal microscopy analysis of these samples revealed that while AChR+ sites were present at all timepoints, many of these were negative for VAcHT at 3, 5, and 8 days post glycerol injection (**Figure 2A**). Quantitative analysis confirmed that in glycerol-treated muscles, the number of AChR+ sites per sample was slightly but not significantly reduced (**Figure 2B**) compared to saline-treated controls. The size of synaptic regions was unaltered (**Supplementary Table S3**). The only exception was at 11 days post injection, where a higher amount of post-synapses was detected in the control samples than at the other timepoints. With respect to VAcHT- and AChR-double positive synapses, glycerol-treated muscles showed significantly lower values between days 3 and 8 post injection as compared to saline samples (**Figure 2C**). These data suggest that glycerol, although affecting both pre- and postsynaptic sites, had a more detrimental impact on the presynaptic component.

Kinetics of Glycerol-Induced Muscle Damage and Regeneration Are Altered by ASCs

The second goal of this study was to address the effect of ASCs on muscle and NMJ regeneration. Thus, directly after intra-muscular application of either saline or glycerol,





ASCs were administered systemically via the tail vein. Then, microscopic analysis was performed to evaluate the consequences of ASC treatment on muscle de- and regeneration. Therefore, muscles were harvested at days 3, 5, and 11 post injection and then sliced. Sections were stained for nuclei and mouse IgG, collagen I, dystrophin, eMHC, or f-actin. While fiber numbers, dystrophin and f-actin results were similar to the samples not treated with ASCs, the data for mIgG, collagen I, eMHC, and CNFs showed interesting differences (Figure 3 and Supplementary Figure S3). Indeed, mIgG and collagen I signals came up at 11 days post glycerol injection and the staining of eMHC showed a basal expression of this regeneration marker in saline-treated muscles. Finally, in glycerol plus ASC-treated animals the number of CNFs continued to increase over time to around $71.4 \pm 15.8\%$ (mean \pm SEM, $n = 3$ muscles) at day 11 post injection, while it remained low in corresponding saline controls ($0.6 \pm 0.7\%$, mean \pm SEM, $n = 3$ muscles). In summary, these results suggested that ASC application induced a late-phase inflammatory response and basal regenerative processes.

ASC Transiently Mitigate Loss of Pre-synapses in the Glycerol Model

Finally, the effects of ASC treatment on NMJs were quantified. Therefore, muscle slices from animals treated with glycerol plus ASCs or saline plus ASCs were labeled for AChR and VAcHT and then analyzed with confocal microscopy (Figure 4A). Counting of AChR+ sites did not reveal any significant differences between glycerol and saline injected muscles (Figure 4B) although at day 3 a trend toward lower numbers of postsynaptic sites in glycerol samples was visible. Quantitative analysis of AChR and VAcHT double positive NMJs showed a good recovery at days 3 and 5 post injection. Indeed, while the fractions of double-positive NMJs in mice not treated with ASCs were low at these timepoints (day 3: $41.4 \pm 17.3\%$; day 5: $48.1 \pm 7.2\%$; mean \pm SEM, $n = 3$ muscles), they reached $65.1 \pm 10.3\%$ and $83.4 \pm 1.3\%$ (mean \pm SEM, $n = 3$ muscles) upon ASC injection. However, in ASC-treated mice, the numbers dropped at day 11 to a value of $57.3 \pm 3.7\%$ (mean \pm SEM, $n = 3$ muscles) (Figure 4C), instead of a further recovery as observed in ASC-untreated animals (day 11: $65.8 \pm 16.9\%$; mean \pm SEM, $n = 3$ muscles). Thus, although ASC treatment showed some beneficial effect on NMJ recovery at early timepoints, this effect did not persist.

DISCUSSION

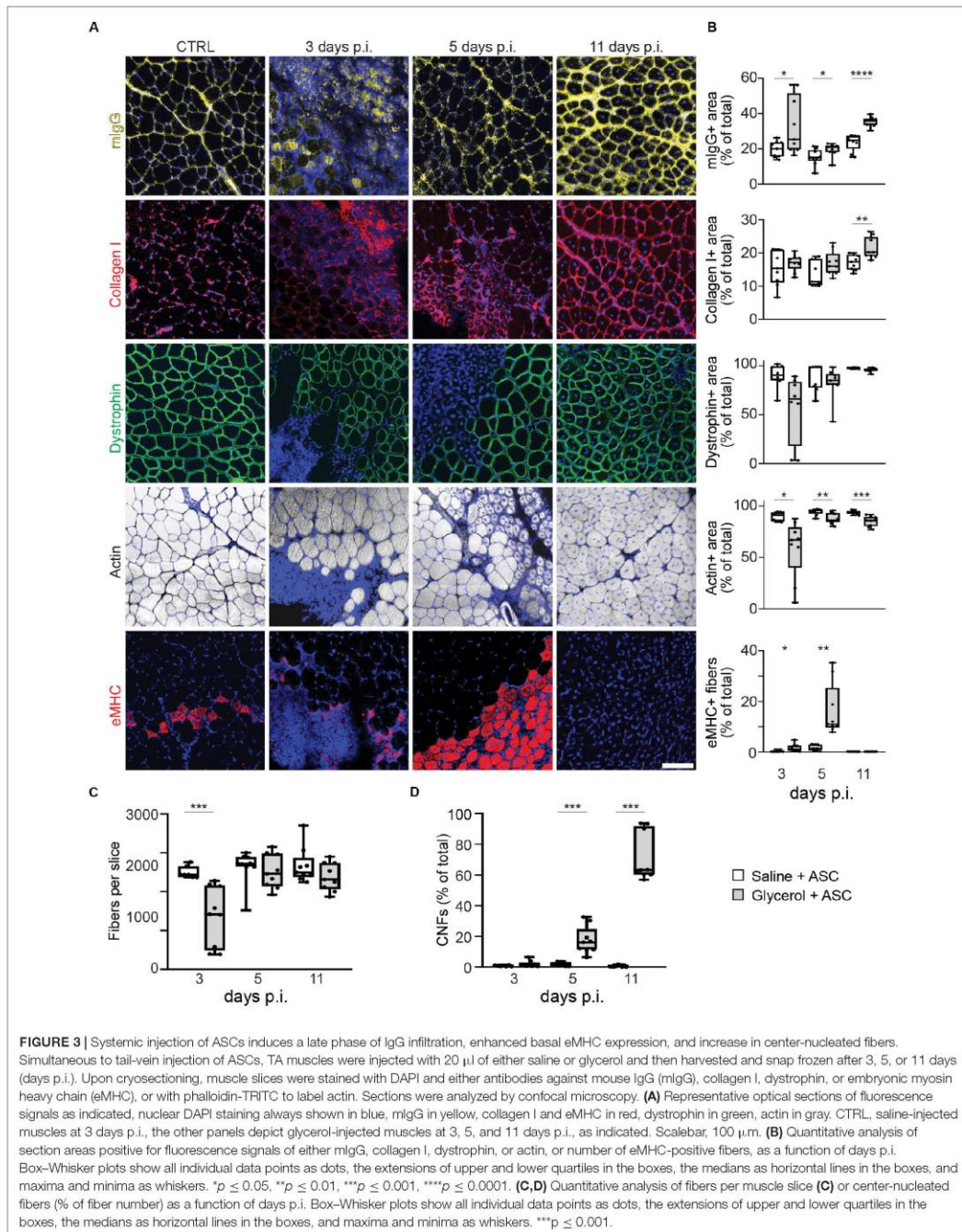
Stem cells have become a widely studied option to treat neuromuscular disorders. However, while their effects on the sarcomeric part of muscles have been investigated regularly, little is known on their regenerative capacity with respect to NMJs. In this study, a glycerol-based muscle damage model was employed to address three biological questions: (i) If a low dose of glycerol could trigger a degeneration – regeneration process, (ii) how this affected NMJs, and (iii) if and how a systemic treatment with ASCs could modulate muscle and synapse recovery.

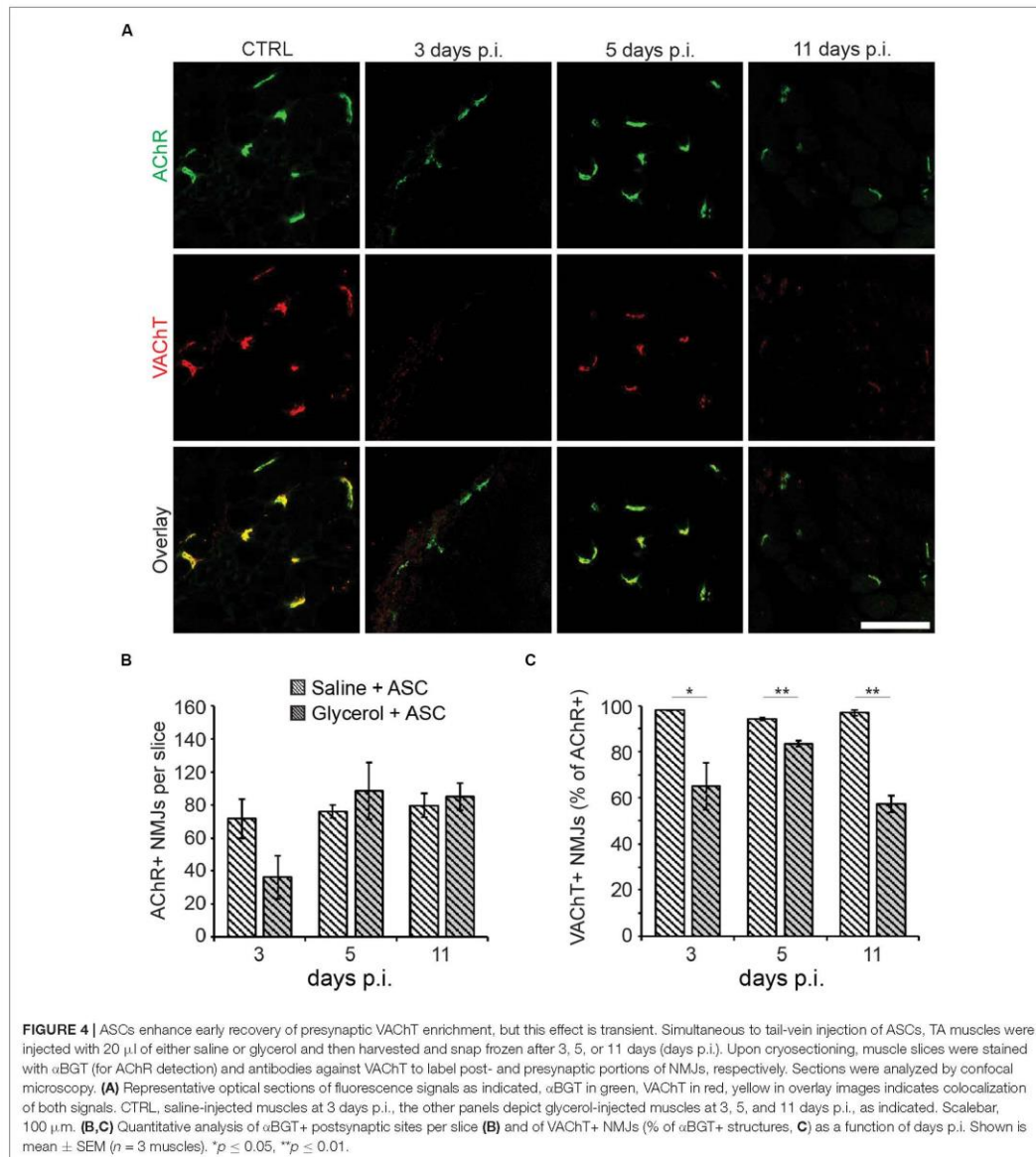
Low-Dose Application of Glycerol to Study Skeletal Muscle Degeneration-Regeneration

Most studies based on glycerol damage applied quantities of 50–100 μ l of glycerol per mouse TA muscle (Lluís et al., 2001; Mahdy et al., 2015; Mahdy, 2018). This protocol was also used to induce massive rhabdomyolysis, in particular for the investigation of acute kidney disease (Korrapati et al., 2012; Huang et al., 2018; Reis et al., 2019). However, since we were more interested in the effects of ASCs on muscle and NMJ regeneration, a milder protocol was sought. One group reported that a dose of 25 μ l of glycerol is able to cause a limited damage in mouse TA muscles including adipocyte infiltration, fibrosis, and necrosis (Arsic et al., 2004). In the present work, 20 μ l per TA muscle were injected and this led to a consistent profile of local muscle degeneration and regeneration (Figure 5A). Regularly, necrosis was evident at 3 days post injection with loss of plasma membrane integrity, dystrophin, and f-actin/contractile apparatus in the affected area. Thereafter, the regeneration marker, eMHC, appeared between days 5 and 8 post injection, and at day 11, all parameters returned to normal except a persisting presence of CNFs. Thus, this paradigm appeared apt for investigating effects of ASC injection on NMJ regeneration.

Effects of Glycerol on NMJ Degeneration-Regeneration

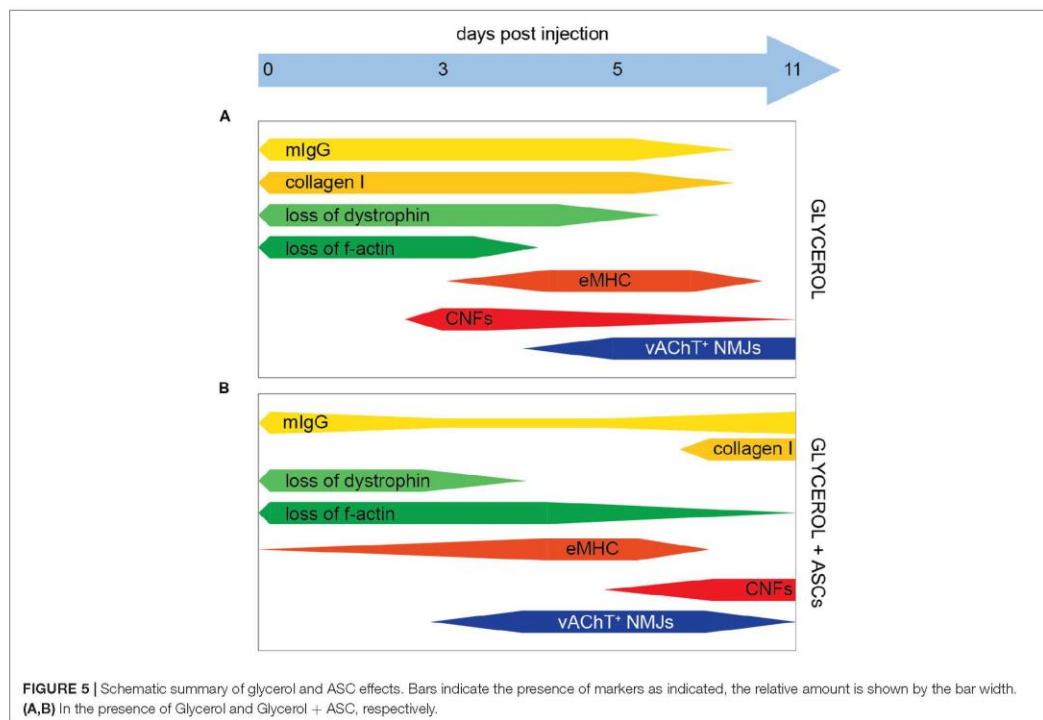
An analysis of post- and pre-synapses in the presence and absence of glycerol showed that the two synaptic compartments responded differently to the treatment: while a small but insignificant loss of post-synapses was detected over the entire experimental period, the pre-synapse marker VAcHT was missing in around 60% of postsynaptic regions at 3 days post glycerol injection and then steadily recovered at the later timepoints (Figure 5A). A more in-depth analysis showed that the distribution of VAcHT and AChR signal colocalization was similar between glycerol and saline injected muscles except for one trait: in the presence of glycerol, much more completely VAcHT-negative synapses were found (Supplementary Figure S4), suggesting that the loss and reestablishment of presynaptic signals was not gradual but occurred in a rather digital manner. However, presynaptic regeneration in all synapses was not obtained within 11 days post injection. It is unclear, why pre- and postsynapse showed a differential susceptibility to glycerol. One possible hypothesis is that the presynaptic terminal as such was more prone to glycerol-induced damage than the postsynaptic part. Another possibility could be due to the focal glycerol-induced damage: it could be that at these sites it led to damage of nerve bundles upstream of undamaged muscle regions. If these damaged bundles were innervating a muscle region unaffected by glycerol, this could, by axon degeneration, affect the presynaptic elements also in apparently unaffected muscle regions. Interestingly, post-synapses were often found also in the most heavily damaged areas in muscle fibers that were infiltrated by mIgG and had lost their dystrophin and f-actin expression. Conversely, VAcHT-positive NMJs were hardly detected in these areas. We have





no formal proof that these same postsynaptic sites were later on reinnervated, but at least the rather constant amounts of postsynaptic sites obtained throughout the experiment argue against a massive phase of ectopic synapse formation. Depending on the type of damage model, different parts of a skeletal muscle can be affected. For example, treatments like mechanical,

thermal, or ischemic injury induce a degeneration of cytoplasm and plasma membrane, but will leave the extracellular matrix largely intact (McMahan et al., 1980; Slater and Schiaffino, 2008; Anderson et al., 2017). Conversely, studies using glycerol showed that this kind of treatment leads to an extensive damage of the extracellular matrix (Hardy et al., 2016; Mahdy, 2018). Previously,



it was described that an intact extracellular matrix is important for postsynaptic preservation and that it can efficiently guide motor axons to original synaptic sites (McMahan et al., 1980). Instead, the present study suggests that the loss of extracellular matrix is not sufficient to disperse postsynaptic assembly of AChR, but it might result in an impaired synapse recovery and pre-postsynaptic matching (Warren et al., 2007; Vilmont et al., 2016; Rogers and Nishimune, 2017). Nonetheless, a partial recovery of pre-postsynaptic matching was found here to start around day 5 post glycerol injection (Figure 5A). Compared to previous reports using either tourniquet (Tu et al., 2017) or nerve injury (Zainul et al., 2018), recovery was apparently faster here. In both previous studies, presynaptic recovery took weeks to complete. One might speculate that the nerve damage was only local in the case of glycerol injection, while it was global in the other models, which could potentially explain the different time courses observed. Thus, having achieved a robust series of degeneration and regeneration processes, we continued in investigating effects of ASC injection on NMJ regeneration.

Effects of ASCs on De/Regeneration of Muscle and NMJs

Adipose-derived stromal cells were previously found to be interesting for clinical application due to their differentiation

capacity, their beneficial effects on other cell types involved in tissue regeneration, and their immunomodulatory properties. In the present work, systemic ASC injection plus local glycerol application led to two major differences in the muscle degeneration – regeneration profiles as compared to glycerol injection alone: First, the reduced amounts of mlgG and collagen I as well as the early detection of eMHC and presynapse regeneration jointly indicated a slightly less severe damage at day 3 post glycerol injection. Second, however, the increasing amounts of mlgG, fibrosis, and CNFs at day 11 post glycerol suggested a secondary damage or differing regeneration phase. The latter effect of ASC application might be due to a mobilization of immune and stem cells into the muscle, causing a stronger regeneration phase. Initially, ASC may dampen the initial degeneration and inflammation by reducing the degree of necrosis and consequently the intensity of neutrophil-induced inflammation. In the following, they may impact the repair and regeneration phase for instance by an IL-6 dependent mechanism, as direct injection of mesenchymal stem/stromal cells was found to increase muscle regeneration via promoting the switch from M1 to M2 macrophages, hence, stimulating muscle stem cell activity (Arnold et al., 2007; Saclier et al., 2013; Mahdy, 2018). Finally, they may affect the remodeling of the regenerating muscle and the maturation of muscle cells, perhaps by a direct effect of ASCs migrating to affected muscles

as reported previously (Vieira et al., 2012). Thus, ASCs could directly act on muscle recovery and enhance muscle regeneration (Rodriguez et al., 2005; Rybalko et al., 2017). By immunostaining of human nuclear marker Ku80 (Kolke et al., 1999; Allard et al., 2014), we addressed settlement of systemically applied ASCs in muscles (Supplementary Figure S5). This did not reveal any clear sign of substantial integration of ASCs in glycerol-treated muscle tissue, rather suggesting that paracrine factors released by ASCs were involved in the observed modulation of degeneration – regeneration processes and immune responses. Recent findings on the effects of ASC secretome injection upon ischemic muscle damage favor this as a principal therapeutic mechanism (Mitchell et al., 2019; Figliolini et al., 2020). Here, ASC-derived exosomes promoted vascular growth and tissue regeneration. With respect to NMJs, two principal differences between mice treated with or without ASC were noted. First, upon application of saline, a rise in the number of postsynaptic sites per muscle slice was observed at day 11 p.i. in the absence (Figure 2B) but not in the presence of ASCs (Figure 4B). At present, the reason for this discrepancy is unclear. Likely, this was not due to general effects of ASC treatment on muscle integrity, since all other measured parameters, i.e. presence of mlgG, collagen I, dystrophin, actin, eMHC, fiber number, and CNFs, were unchanged. This suggests, that the observed difference was due to either, experimental variability or a specific effect of the ASCs on NMJ regeneration that needs further investigation. Second, upon injection of glycerol, ASC administration led to a fast recovery of post-synapse numbers within 5 days post injection and by trend also to a higher and faster presynapse recovery than in the absence of ASCs. The latter aspect, though, was reverted, likely due to the late-phase degenerative response, as indicated by enhanced levels of mlgG and collagen I on day 11 p.i. (Figure 5).

CONCLUSION

In conclusion, although our data suggest a partially positive effect of ASCs on the recovery of NMJs in the early regenerative phase, a secondary degenerative or aberrant regenerative period reverted these benefits at a later stage. Due to the manifold effects of ASCs on various phases of de- and regeneration, which were likely involving muscle and neuronal cells, endothelial cells, but also all kind of immune cells, future studies need to further explore the mechanisms involved and work around late degenerative processes.

REFERENCES

- Allard, J., Li, K., Lopez, X., Blanchard, S., Barbot, P., Rorive, S., et al. (2014). Immunohistochemical toolkit for tracking and quantifying xenotransplanted human stem cells. *Regenerat. Med.* 9, 437–452. doi: 10.2217/rme.14.26. Immunohistochemical
- Anderson, J., Mai-khoi, Q., Daneshvar, T., Suzuki, J., Dort, W., Mizunoya, K., et al. (2017). The role of semaphorin3A in myogenic regeneration and the formation of functional neuromuscular junctions on new fibres. *Biol. Rev.* 92, 1389–1405. doi: 10.1111/brv.12286
- Arecco, N., Clarke, F. K., Jones, D. M., Simpson, D., Mason, R. J., Beynon, M., et al. (2016). Elastase levels and activity are increased in dystrophic muscle and impair myoblast cell survival, proliferation and differentiation. *Sci. Rep.* 6, 1–20. doi: 10.1038/srep24708
- Arnold, L., Henry, F., Poron, Y., Baba-Amer, Y., Van Rooijen, N., Plonquet, R., et al. (2007). Inflammatory monocytes recruited after skeletal muscle injury switch into antiinflammatory macrophages to support myogenesis. *J. Exp. Med.* 204, 1057–1069. doi: 10.1084/jem.20070075
- Arsic, N., Zaccagna, L., Zentilin, G., Ramirez-Correa, L., Salvi, G., Sinagra, U., et al. (2004). Vascular endothelial growth factor stimulates skeletal muscle regeneration in vivo. *Mol. Ther.* 10, 844–854. doi: 10.1016/j.yjme.2004.08.007

DATA AVAILABILITY STATEMENT

The raw data supporting the conclusions of this article will be made available by the authors, without undue reservation, to any qualified researcher.

ETHICS STATEMENT

The animal study was reviewed and approved by the Regierungspräsidium Karlsruhe.

AUTHOR CONTRIBUTIONS

NG and RR contributed to conception and design of the study. MR, SH, and TS performed the experiments and statistical analysis. MR and RR wrote the first draft of the manuscript. KB and MH contributed to resources and materials. All authors contributed to manuscript revision and, read and approved the submitted version.

FUNDING

This work was supported by the Cooperative Research Training Group: Tissue Analytics for Stem Cell based Diagnostics and Therapy (TASCDT). This work was funded by the German Federal Ministry of Education and Research (BMBF) as part of the Innovation Partnership M²Aind, project M²OGA (03FH8I02IA) within the framework Starke Fachhochschulen–Impuls für die Region (FH–Impuls).

ACKNOWLEDGMENTS

We are grateful to Viktoria Skude for technical assistance and to Adriana Torres Crigna and Daniela Nardozi for the precious insights and help regarding the use of ASCs.

SUPPLEMENTARY MATERIAL

The Supplementary Material for this article can be found online at: <https://www.frontiersin.org/articles/10.3389/fnmol.2020.00107/full#supplementary-material>

- Bieback, K., Hecker, T., Schlechter, T., Hofmann, N., Brouses, T., Redmer, D., et al. (2012). Replicative aging and differentiation potential of human adipose tissue-derived mesenchymal stromal cells expanded in pooled human or fetal bovine serum. *Cytotherapy* 14, 570–583. doi: 10.3109/14653249.2011.652809
- Biral, D., Jakubiec-Puka, I., Ciechomska, M., Sandri, K., Rossini, S., Carraro, U., et al. (2000). Loss of dystrophin and some dystrophin-associated proteins with concomitant signs of apoptosis in rat leg muscle overworked in extension. *Acta Neuropathol.* 100, 618–626. doi: 10.1007/s004010000231
- Boldyreva, M. A., Shevchenko, Y., Molokotina, P., Makarevich, I., Beloglazova, E., Zubkova, K., et al. (2019). Transplantation of adipose stromal cell sheet producing hepatocyte growth factor induces pleiotropic effect in ischemic skeletal muscle. *Int. J. Mol. Sci.* 20:3088. doi: 10.3390/ijms20123088
- Cowling, B. S., and Thielemans, L. (2020). Translational medicine in neuromuscular disorders: from academia to industry. *Dis. Models Mech.* 13, 1–6. doi: 10.1242/dmm.041434
- Czerwinska, A. M., Streminska, M., Ciemerych, M., and Grabowska, I. (2012). Mouse gastrocnemius muscle regeneration after mechanical or cardiotoxin injury. *Folia Histochem. Cytobiol.* 50, 144–153. doi: 10.5603/FHC.2012.0021
- Deasy, B. M., Lu, J., Tebbets, J., Feduska, R., Schugar, J., Pollett, B., et al. (2007). A role for cell sex in stem cell-mediated skeletal muscle regeneration: female cells have higher muscle regeneration efficiency. *J. Cell Biol.* 177, 73–86. doi: 10.1083/jcb.200612094
- Fambrough, D. M., Devreotes, P., Gardner, J. M., and Card, D. (1979). The life history of acetylcholine receptors. *Prog. Brain Res.* 49, 325–334. doi: 10.1016/S0079-6123(08)64644-0
- Feng, F., Deng, J., Luo, L., and Huang, Q. (2019). Role of the notch signaling pathway in fibrosis of denervated skeletal muscle. *Curr. Med. Sci.* 39, 419–425. doi: 10.1007/s11596-019-2053-z
- Figliolini, F., Ranghino, C., Grange, M., Cedrino, M., Tapparo, C., Cavallari, A., et al. (2020). Extracellular vesicles from adipose stem cells prevent muscle damage and inflammation in a mouse model of hind limb ischemia: role of neuregulin-1. *Arterioscler. Thromb. Vasc. Biol.* 40, 239–254. doi: 10.1161/ATVBAHA.119.313506
- Forcales, S. V. (2015). Potential of adipose-derived stem cells in muscular regenerative therapies. *Front. Aging Neurosci.* 7:123. doi: 10.3389/fnagi.2015.00123
- Gibertini, S., Zanotti, S., Savadori, M., Curcio, S., Saredi, F., Salerno, F., et al. (2014). Fibrosis and inflammation are greater in muscles of beta-sarcoglycan-null mouse than mdx mouse. *Cell Tissue Res.* 356, 427–443. doi: 10.1007/s00441-014-1854-4
- Gillies, A. R., and Lieber, R. L. (2011). Structure and function of the skeletal muscle extracellular matrix. *Muscle Nerve* 44, 318–331. doi: 10.1002/mus.22094
- Gois, B., Samuel, D., Horita, I., da Fonseca, M., Alves, L., Nagaraju, K., et al. (2019). A Promising future for stem-cell-based therapies in muscular dystrophies-in vitro and in vivo treatments to boost cellular engraftment. *Int. J. Mol. Sci.* 20, 5433. doi: 10.3390/ijms20215433
- Gorecka, A., Salemi, D., Haralampieva, F., Moalli, D., Stroka, D., Candinas, D., et al. (2018). Autologous transplantation of adipose-derived stem cells improves functional recovery of skeletal muscle without direct participation in new myofiber formation. *Stem Cell Res. Ther.* 9, 1–12. doi: 10.1186/s13287-018-0922-1
- Hardy, D., Besnard, M., Latil, G., Jouvin, D., Briand, C., Thépenier, G., et al. (2016). Comparative study of injury models for studying muscle regeneration in mice. *PLoS One* 11:e0147198. doi: 10.1371/journal.pone.0147198
- Huang, M. Z., and Gopalakrishnakone, P. (1996). Pathological changes induced by an acidic phospholipase A2 from ophiophagus hannah venom on heart and skeletal muscle of mice after systemic injection. *Toxicol.* 34, 201–211. doi: 10.1016/0041-0101(95)00128-X
- Huang, R., Shi, M., Guo, F., Feng, Y., Feng, Y., and Liu, J. (2018). Pharmacological inhibition of fatty protects against thabdomyolysis-induced acute kidney injury. *Front. Pharmacol.* 9:917. doi: 10.3389/fphar.2018.00917
- Huebner, K. D., Jassal, D., Halevy, O., Pines, M., and Anderson, J. (2008). Functional resolution of fibrosis in mdx mouse dystrophic heart and skeletal muscle by halofuginone. *Am. J. Physiol. Heart Circ. Physiol.* 294, 1550–1561. doi: 10.1152/ajpheart.01253.2007
- Iwata, Y., Suzuki, O., and Wakabayashi, S. (2013). Decreased surface sialic acid content is a sensitive indicator of muscle damage. *Muscle Nerve* 47, 372–378. doi: 10.1002/mus.23632
- Judson, R. N., Gray, C., Walker, A., Carroll, C., Itzstein, A., Lionikas, P., et al. (2013). Constitutive expression of yes-associated protein (Yap) in adult skeletal muscle fibres induces muscle atrophy and myopathy. *PLoS One* 8:e0059622. doi: 10.1371/journal.pone.0059622
- Kastenschmidt, J. M., Ellefsen, L., Manmaa, J., Giebel, R., Yahia, R., Ayer, P., et al. (2019). QuantiMus: a machine learning-based approach for high precision analysis of skeletal muscle morphology. *Front. Physiol.* 10:1116. doi: 10.3389/fphys.2019.01416
- Kawai, H., Nishino, K., Kusaka, T., Naruo, Y., Tamaki, Y., and Iwasa, M. (1990). Experimental glycerol myopathy: a histological study. *Acta Neuropathol.* 80, 192–197. doi: 10.1007/BF00308923
- Kern, S., Eichler, J., Stoeve, H., Klüter, Z., and Bieback, K. (2006). Comparative analysis of mesenchymal stem cells from bone marrow, umbilical cord blood, or adipose tissue. *Stem Cells* 24, 1294–1301. doi: 10.1634/stemcells.2005-0342
- Kitajima, Y., and Ono, Y. (2016). Estrogens maintain skeletal muscle and satellite cell functions. *J. Endocrinol.* 229, 267–275. doi: 10.1530/JOE-15-0476
- Koike, M., Awaji, M., Kataoka, G., Tsujimoto, T., Kartasova, Y. T., and Koike, A. (1999). Differential subcellular localization of DNA-dependent protein kinase components ku and dna-pkcs during mitosis. *J. Cell Sci.* 112, 4031–4039.
- Korrapati, M. C., Brooke, E., Shaner, R., and Schnellmann, R. G. (2012). Recovery from glycerol-induced acute kidney injury is accelerated by suramin. *J. Pharmacol. Exp. Ther.* 341, 126–136. doi: 10.1124/jpet.111.190249
- Lluis, F., Roma, M., Suelves, M., Parra, G., Anioarte, E., Gallardo, I., et al. (2001). Urokinase-dependent plasminogen activation is required for efficient skeletal muscle regeneration in vivo. *Blood* 97, 1703–1711. doi: 10.1182/blood.V97.6.1703
- Maeda, M., Ohba, S., Nakagomi, Y., Suzuki, S., Kiryu-Seo, K., Namikawa, K., et al. (2004). Vesicular acetylcholine transporter can be a morphological marker for the reinnervation to muscle of regenerating motor axons. *Neurosci. Res.* 48, 305–314. doi: 10.1016/j.neures.2003.11.008
- Mahdy, M. A., Warita, A., and Hosaka, Y. (2016). Early ultrastructural events of skeletal muscle damage following cardiotoxin-induced injury and glycerol-induced injury. *Micron* 91, 29–40. doi: 10.1016/j.micron.2016.09.009
- Mahdy, M. A. A. (2018). Glycerol-induced injury as a new model of muscle regeneration. *Cell Tissue Res* 374, 233–241. doi: 10.1007/s00441-018-2846-6
- Mahdy, M. A. A., Hsiao, A., Lei, Y., Wakamatsu, J., Hosaka, Y., and Nishimura, T. (2015). Comparative study of muscle regeneration following cardiotoxin and glycerol injury. *Ann. Anat.* 202, 18–27. doi: 10.1016/j.aanat.2015.07.002
- McCarthy, J., Mula, J., Miyazaki, M., Erfani, R., Garrison, M., Farooqui, A., et al. (2011). Effective fiber hypertrophy in satellite cell-depleted skeletal muscle. *Development* 138, 3657–3666. doi: 10.1242/dev.068858
- McDonald, A. A., Sadie, L., Kunz, S., Ralles, S., and McLoon, L. (2015). Disease course in Mdx:Utrophin^{+/−} mice: comparison of three mouse models of duchenne muscular dystrophy. *Physiol. Rep.* 3, 1–22. doi: 10.14814/phy2.12391
- McMahan, U. J., Edgington, D., and Kuffler, D. P. (1980). Factors that influence regeneration of the neuromuscular junction. *J. Exp. Biol.* 89, 31–42.
- Mitchell, R., Mellows, B., Sheard, J., Antoniolli, M., Kretz, O., and Chambers, D. (2019). Secretome of adipose-derived mesenchymal stem cells promotes skeletal muscle regeneration through synergistic action of extracellular vesicle cargo and soluble proteins. *Stem Cell Res. Ther.* 10, 1–19. doi: 10.1186/s13287-019-1213-1
- Murphy, M. M., Lawson, J., Mathew, S., David, A., Hutcheson, A., and Kardon, G. (2011). Satellite cells, connective tissue fibroblasts and their interactions are crucial for muscle regeneration. *Development* 138, 3625–3637. doi: 10.1242/dev.064162
- Pisani, D. F., Cynthia, D. K., Botterna, C., Butori, C., Dani, C., and Claude, A. (2010). Mouse model of skeletal muscle adiposity: a glycerol treatment approach. *Biochem. Biophys. Res. Commun.* 396, 767–773. doi: 10.1016/j.bbrc.2010.05.021
- Proto, J. D., Tang, A., Lu, W. C. W., Chen, E., Stahl, M., Poddar, S. A., et al. (2015). NF- κ B inhibition reveals a novel role for HGF during skeletal muscle repair. *Cell Death Dis.* 6:e1730. doi: 10.1038/cddis.2015.66

- Reis, N. G., Della, C., Francescat, L., De Almeida, F., Giovanini, R., Silva Costa, R. M., et al. (2019). Protective effect of calcitriol on rhabdomyolysis-induced acute kidney injury in rats. *Sci. Rep.* 9:7090. doi: 10.1038/s41598-019-43564-1
- Rodrigues, M., Echigoya, Y., Maruyama, R., Rowel, Q., Fukada, I., and Yokota, T. (2016). Impaired regenerative capacity and lower revertant fibre expansion in dystrophin-deficient mdx muscles on DBA/2 background. *Sci. Rep.* 6:38371. doi: 10.1038/srep38371
- Rodriguez, A. M., Pisani, C., Dechesne, C., Turc-Carel, J., Kurzenne, Y., Wdziekonski, B., et al. (2005). Transplantation of a multipotent cell population from human adipose tissue induces dystrophin expression in the immunocompetent mdx mouse. *J. Exp. Med.* 201, 1397–1405. doi: 10.1084/jem.20042224
- Rogers, R. S., and Nishimune, H. (2017). The role of laminins in the organization and function of neuromuscular junctions. *Matrix Biol.* 5, 86–105. doi: 10.1016/j.matbio.2016.08.008
- Rybalko, V., Hsieh, L., Ricles, M., Chung, E., Farrar, R., and Suggs, L. (2017). Therapeutic potential of adipose-derived stem cells and macrophages for ischemic skeletal muscle repair. *Regenerat. Med.* 12, 153–167. doi: 10.2217/rme-2016-0094
- Saclier, M., Yacoub-Youssef, A., Mackey, L., Arnold, H., Ardjoune, M., Magnan, M., et al. (2013). Differentially activated macrophages orchestrate myogenic precursor cell fate during human skeletal muscle regeneration. *Stem Cells* 31, 384–396. doi: 10.1002/stem.1288
- Schiaffino, S., Gorza, S., Sartore, L., Saggin, L., and Carli, M. (1986). Embryonic myosin heavy chain as a differentiation marker of developing human skeletal muscle and rhabdomyosarcoma. a monoclonal antibody study. *Exp. Cell Res.* 163, 211–220. doi: 10.1016/0014-4827(86)90574-4
- Serrano, A. L., and Muñoz-Cánoves, P. (2010). Regulation and dysregulation of fibrosis in skeletal muscle. *Exp. Cell Res.* 316, 3050–3058. doi: 10.1016/j.yexcr.2010.05.035
- Slater, C. R., and Schiaffino, S. (2008). "Innervation of regenerating muscle." in *Skeletal Muscle Repair and Regeneration*, Vol. 3, eds S. Schiaffino and T. Partridge (Dordrecht: Springer), 303–334. doi: 10.1007/978-1-4020-6768-6_14
- Sugita, S., Leland, L., Wood, S., Vaughan, M., Gomes, M., Camargo, L., et al. (2016). VACHT overexpression increases acetylcholine at the synaptic cleft and accelerates aging of neuromuscular junctions. *Skeletal Muscle* 6, 1–17. doi: 10.1186/s13395-016-0105-7
- Tiryakioglu, O., Erkok, B., Tunerit, O., Uysal, H., Altin, T., and Aydin, S. (2015). The effect of iloprost and N-Acetylcysteine on skeletal muscle injury in an acute aortic ischemia-reperfusion model: an experimental study. *BioMed Res. Int.* 2015:453748. doi: 10.1155/2015/453748
- Torres-Torrillas, M., Rubio, M., Damia, E., Cuervo, B., Romero, A., Peláez, P., et al. (2019). Adipose-derived mesenchymal stem cells: a promising tool in the treatment of musculoskeletal diseases. *Int. J. Mol. Sci.* 20:3105. doi: 10.3390/ijms20123105
- Tu, H., Zhang, D., Corrick, R. M., Muelleman, R. L., Wadman, M., and Li, Y. (2017). Morphological regeneration and functional recovery of neuromuscular junctions after tourniquet-induced injuries in mouse hindlimb. *Front. Physiol.* 8:207. doi: 10.3389/fphys.2017.00207
- Vieira, N. M., Valadares, E., Zucconi, M., Secco, C. R., Bueno Junior, V., Brandalise, A., et al. (2012). Human adipose-derived mesenchymal stromal cells injected systemically into grmd dogs without immunosuppression are able to reach the host muscle and express human dystrophin. *Cell Transplant.* 21, 1407–1417. doi: 10.3727/096368911X
- Vilmont, V., Cadot, B., Vezin, E., Le Grand, F., and Gomes, E. R. (2016). Dynein disruption perturbs post-synaptic components and contributes to impaired MuSK clustering at the NMJ: implication in ALS. *Sci. Rep.* 6, 1–13. doi: 10.1038/srep27804
- Warren, G. L., Summan, M., Gao, X., Chapman, R., Hulderman, T., and Simeonova, P. (2007). Mechanisms of skeletal muscle injury and repair revealed by gene expression studies in mouse models. *J. Physiol.* 582, 825–841. doi: 10.1113/jphysiol.2007.132373
- Webster, M. T., Manor, U., Lippincott-Schwartz, J., and Fan, C. M. (2015). Intravital imaging reveals ghost fibers as architectural units guiding myogenic progenitors during regeneration. *Cell Stem Cell* 18, 243–252. doi: 10.1016/j.stem.2015.11.005
- Zainul, Z., Heikkinen, A., Koivisto, H., Rautalahti, I., Kallio, M., Lin, S., et al. (2018). Collagen XIII is required for neuromuscular synapse regeneration and functional recovery after peripheral nerve injury. *J. Neurosci.* 38, 4243–4258. doi: 10.1523/JNEUROSCI.3119-17.2018

Conflict of Interest: The authors declare that the research was conducted in the absence of any commercial or financial relationships that could be construed as a potential conflict of interest.

Copyright © 2020 Rigon, Hörner, Sraka, Bieback, Gretz, Hafner and Rudolf. This is an open-access article distributed under the terms of the Creative Commons Attribution License (CC BY). The use, distribution or reproduction in other forums is permitted, provided the original author(s) and the copyright owner(s) are credited and that the original publication in this journal is cited, in accordance with accepted academic practice. No use, distribution or reproduction is permitted which does not comply with these terms.



A Novel Optical Tissue Clearing Protocol for Mouse Skeletal Muscle to Visualize Endplates in Their Tissue Context

Marion Patrick Ivey Williams¹, Matteo Rigon¹, Tatjana Straka^{1,2}, Sarah Janice Hörner^{1,2}, Manfred Thiel³, Norbert Gretz^{4,5}, Mathias Hafner^{1,5}, Markus Reischl⁶ and Rüdiger Rudolf^{1,2,5,7*}

¹Institute of Molecular and Cell Biology, Mannheim University of Applied Sciences, Mannheim, Germany, ²Interdisciplinary Center for Neurosciences, Heidelberg University, Heidelberg, Germany, ³Department of Anesthesiology and Surgical Intensive Care Medicine, Medical Faculty Mannheim, Heidelberg University, Mannheim, Germany, ⁴Medical Faculty Mannheim, Medical Research Center, Heidelberg University, Mannheim, Germany, ⁵Medical Faculty Mannheim, Institute of Medical Technology, Mannheim University of Applied Sciences, Mannheim, Germany, ⁶Institute for Automation and Applied Informatics, Karlsruhe Institute of Technology, Eggenstein-Leopoldshafen, Germany, ⁷Institute of Toxicology and Genetics, Karlsruhe Institute of Technology, Eggenstein-Leopoldshafen, Germany

OPEN ACCESS

Edited by:

Thomas Fath,
Macquarie University, Australia

Reviewed by:

Frederic A. Meunier,
The University of Queensland,
Australia
Leonardo Sacconi,
Università degli Studi di Firenze, Italy

*Correspondence:

Rüdiger Rudolf
r.rudolf@hs-mannheim.de

Received: 12 October 2018

Accepted: 01 February 2019

Published: 27 February 2019

Citation:

Williams MPI, Rigon M, Straka T, Hörner SJ, Thiel M, Gretz N, Hafner M, Reischl M and Rudolf R (2019) A Novel Optical Tissue Clearing Protocol for Mouse Skeletal Muscle to Visualize Endplates in Their Tissue Context. *Front. Cell. Neurosci.* 13:49. doi: 10.3389/fncel.2019.00049

Neuromuscular junctions (NMJs) mediate skeletal muscle contractions and play an important role in several neuromuscular disorders when their morphology and function are compromised. However, due to their small size and sparse distribution throughout the comparatively large, inherently opaque muscle tissue the analysis of NMJ morphology has been limited to teased fiber preparations, longitudinal muscle sections, and flat muscles. Consequently, whole mount analyses of NMJ morphology, numbers, their distribution, and assignment to a given muscle fiber have also been impossible to determine in muscle types that are frequently used in experimental paradigms. This impossibility is exacerbated by the lack of optical tissue clearing techniques that are compatible with clear and persistent NMJ stains. Here, we present MYOCLEAR, a novel and highly reproducible muscle tissue clearing protocol. Based on hydrogel-based tissue clearing methods, this protocol permits the labeling and detection of all NMJs in adult hindleg extensor digitorum longus muscles from wildtype and diseased mice. The method is also applicable to adult mouse diaphragm muscles and can be used for different staining agents, including toxins, lectins, antibodies, and nuclear dyes. It will be useful in understanding the distribution, morphological features, and muscle tissue context of NMJs in hindleg muscle whole mounts for biomedical and basic research.

Keywords: acetylcholine receptor, hydrogel embedding, NMJ, optical tissue clearing, skeletal muscle

INTRODUCTION

Vertebrate NMJs are the synapses between cholinergic motor neurons and skeletal muscle fibers that mediate voluntary muscle contraction. They are embedded in a complex of many different cellular tissue components, with their pre- and postsynaptic apparatuses juxtaposed onto each other. Depending on the species, NMJs are about 10–50 μm in diameter and come in varying forms, such as grape-, plaque-, or pretzel-shaped structures (Lu and Lichtman, 2007). The latter

design is of particular interest as it is prevalent in rodent NMJs and is often used as an indicator for neuromuscular disorders or other disease states when fragmentation, simplification, growth, shrinkage, and other such deviations occur (Lyons and Slater, 1991; Valdez et al., 2010; Carnio et al., 2014; Rudolf et al., 2014). In healthy adult mouse muscle, each syncytial fiber is roughly 50 μm in diameter and up to 4 cm in length; it contains thousands of myonuclei and is precisely innervated by one NMJ (Krause, 1863). This is different during embryonic development and the perinatal stages, where most muscle fibers are contacted by more than one neuron (Lee et al., 2017). This sort of poly-innervation is corrected within the first 2 to 3 postnatal weeks. Nevertheless, it can reappear during denervation—reinnervation cycles and other non-physiological conditions that frequently occur in genetic, acquired, and aging muscle diseases (Gorio et al., 1983). Previous and more recent studies increasingly suggest important feed forward and feedback mechanisms between the different cell types that mutually affect cell behavior (Carnio et al., 2014; Wu et al., 2015; Khan et al., 2016; Lee et al., 2017; Dobrowolny et al., 2018). So far, synoptic consideration of pathophysiological processes on the entire musculoskeletal organ has been severely hampered by two main factors. First, the mentioned mono-innervation of muscle fibers in combination with the extreme discrepancy between small NMJ size and large muscle fiber dimensions leads to an unequal distribution of these components in the organ; therefore, effects seen in one part of the muscle might not occur in others. Second, from a technical point of view, optical tissue clearing methods that would allow for such analysis of NMJs in their whole mount context have been lacking so far.

Introduced by Chung et al., CLARITY (Clear Lipid-exchanged Acrylamide-hybridized Rigid Imaging/Immunostaining/*in situ* hybridization-compatible Tissue-hydrogel) is one of the many new tissue clearing methods available and has gained a great deal of attention due to its robustness and compatibility with many different stainings (Chung and Deisseroth, 2013; Chung et al., 2013). This protocol and its variations (Lee et al., 2014; Tomer et al., 2014; Yang et al., 2014; Kim et al., 2015; Kleffel et al., 2016; Greenbaum et al., 2017; Du et al., 2018; Wang et al., 2018) address Refractive Index (RI) heterogeneity by first embedding the tissue in an acrylamide/bis-acrylamide based hydrogel. In addition to increasing tissue stability and porosity, this stabilizes the RI across the tissue from the estimated $n = 1.50$ of dry tissue to $n = 1.457$. Lipids are then drawn out of the embedded samples via active clearing in an electrophoresis chamber that applies a current and a continual stream of SDS over the tissue. This process increases the homogeneity of the RI throughout the sample even further, since lipids tend to have varying RIs and can increase light scattering when imaging deep into tissue. Even though this is a very promising method, Milgroom et al found it was incompatible with α -bungarotoxin (BGT) (Milgroom and Ralston, 2016), the most widely used postsynaptic NMJ marker, which labels nicotinic acetylcholine receptors (AChRs) with unmatched specificity. Their hypothesis was that the additional cross-linking and fixation prevented access of the toxin to the acetylcholine receptors (AChR). This incompatibility was further validated by Zhang et al., who found

that even a modified passive CLARITY method resulted in the absence of BGT signals and appears to be very sensitive to standard optical clearing procedures (Zhang et al., 2018). Another study did report the presence of BGT fluorescence signals with the use of *in vivo* injected BGT in combination with a modified organic-solvent clearing protocol based on 3DISCO (Chen et al., 2016). Nonetheless, the combination of fluorophore compatibility/stability, tissue shrinkage, and the fact that *in vivo* injection of BGT hampers *post-hoc* stainings make this protocol and other organic solvent-based methods less than ideal for most applications.

Here, we address many of these issues by introducing a new optical tissue clearing protocol that is based on aldehyde fixation and hydrogel embedding. This robust protocol enables transparency of samples with a thickness $>700 \mu\text{m}$ and is compatible with mouse diaphragm as well as EDL muscles. Additionally, it presents long-term fluorophore stability of NMJ staining in mouse skeletal muscle whole mounts.

MATERIALS AND METHODS

Animals and Sample Preparation

In the current study, adult C57BL/10J, and BL10/JMDX mice were used. Animals were maintained in a local animal facility and their use and care were approved by German authorities according to EC directive 2010/63. For all experiments, adult mice were euthanized by cervical dislocation. Either whole hind limbs or just EDL muscles as well as diaphragm muscles were freshly dissected. Samples were then immediately immersed in 4% PFA/1x PBS and incubated for a minimum of 24 h on a roller mixer at 4°C.

MYOCLEAR

A detailed protocol including reagent and equipment lists, photos of custom-made devices, and troubleshooting can be found in the **Supplementary Methods** section. Briefly, muscles were either freshly dissected or taken from PFA fixed mouse muscles. However, we recommend dissecting muscles from PFA fixed specimens since this tends to drastically reduce accidental damage to the tissue. Then, 100 mg of VA-044 initiator (final concentration 0.25%) and 40 ml of freshly prepared hydrogel monomer solution (A4P0) were added to 50 ml light resistant Falcon tubes, briefly hand mixed, and kept on ice to prevent premature polymerization. One muscle was then placed in each falcon tube and incubated on a roller mixer for 5 days at 4°C. After, muscles were degassed for 1 h via a custom-built degassing apparatus which allowed nitrogen to bubble over the samples (see **Supplementary Methods** section for photograph). The caps of the Falcon tubes were then loosely placed back on and the tubes transferred to an air tight desiccator where they were vacuumed under a 90 kPa negative pressure for an additional hour in order to purge any remaining oxygen from the sample. The desiccator was then flushed with nitrogen, Falcon tube caps tightened, and placed in a hot water bath at 37°C for 4 h with shaking for polymerization. Samples were then removed from the Falcon tube and excess hydrogel removed by washing samples with 1x PTW overnight on a roller mixer at room temperature. It is

important to note that in lieu of using a desiccator and hot water bath, we found that using Life Canvas's EasyGel system resulted in comparable results and made sample handling simpler and easier. However, the custom-built nitrogen bubbling apparatus was still needed to ensure uniform hydrogel polymerization.

For NMJ plus nuclei labeling, samples were stained as follows, inspired by the iDISCO staining protocol (Renier et al., 2014): Samples were washed in 1x PTwH with solution changes every hour for 2 h. After washing, samples were incubated in blocking and permeabilization solution (BnP) with shaking at 37°C for 48 h. Then, the BnP solution was replaced with 1 ml of fresh BnP solution, the dyes added [BGT-AF647 (1:200), BGT-AF555 (1:200), and/or DRAQ5 (1:300)], and allowed to incubate for 5 days at 37°C with shaking. After, samples were thoroughly washed in 1x PTwH with solution changes every 10 min, 15 min, 30 min, 1 h, and then every 2 h for a minimum of 2 days. The detergent was then removed by washing samples in distilled water for 4–8 h with frequent solution changes. Lastly, samples were incubated in 88% glycerol at room temperature for a minimum of 24 h for RI matching and long-term storage. Additionally, it was found that samples were stable for many months when stored in this manner. For indirect immunofluorescence staining, samples were processed as described above, with modifications as detailed in the **Supplementary Methods**. A list of primary and secondary antibodies and their dilutions can also be found there.

X-CLARITY

For all samples stained after active clearing, a Biozym X-CLARITY protocol was followed, excluding the perfusion step. This is available for download from their website, <https://www.biozym.com/>. Briefly, EDL muscles were dissected from PFA fixed hind limbs and washed for 3 h in PBS at 4°C. Samples were then transferred to 50 ml light resistant falcon tubes containing 40 ml of freshly prepared 4% PFA/A4P0 monomer solution and 100 mg of VA-044 initiator, followed by a 5-day incubation on a roller mixer at 4°C. Then, samples were degassed via partial vacuum for 1 h, flushed with nitrogen, and incubated at 37°C for 3 h in a hot water bath to induce polymerization. Afterwards, samples were washed for 1–2 h in 1x PBS on a roller mixer at RT to remove excess hydrogel, transferred to an X-Clarity brain slice tissue holder, and lowered into the X-Clarity ETC chamber, where they were cleared for 3 h with 4% SDS buffer at a flow rate of 30 rpm; temperature: 37°C; current: 1.5 A. After, samples were thoroughly washed in PBST at 37°C for 24 h, then stored at 4°C in 1x PBS. For staining, samples were processed following the immunostaining section described in the Biozym protocol, with a dilution factor of 1:200 and 1:500 for BGT-AF647 and Wheat Germ Agglutinin CF488 conjugate (WGA-488; Biotium), respectively. Lastly, prepared samples were kept in 88% glycerol for storage and imaging.

Active and Passive CLARITY

EDL muscles were processed following the MYOCLEAR protocol described above, followed by either active or passive clearing for 24 h in the X-CLARITY ETC tissue clearing system. Here, a steady flow of 4% SDS at a rate of 30 rpm was applied to the samples and the current either left off for passive

clearing or adjusted according to the experiment for active clearing, with the maximum temperature recorded at the end of each run, see **Supplementary Methods** section. For experiments that addressed the effect refixation would have on preserving BGT fluorescence, samples were stained, incubated in 4% PFA for 24 h at 4°C, and then cleared. Lastly, all samples were stored and mounted in 88% Glycerol for imaging and kept at room temperature.

Microscopy

Single stack acquisitions were imaged using a Leica Microsystems TCS SP2 equipped with a Leica Microsystems HC PL AP0 20x/0.75 IMM CORE CS2 objective, Leica confocal software version 2.61, a KrAr laser (488 nm, 514 nm), a diode-pumped laser (561 nm), and a HeNe laser (633 nm). For tile scans, an upright Leica Microsystems TCS SP8 equipped with LAS X software, a 488 nm laser, a 561 nm laser, a 633 nm laser, and Leica Microsystems clarity objective HC FLUOTAR L 25x/1.00 IMM ($ne = 1.457$) was used. 3D imaging of whole mount muscle samples was performed in 88% glycerol immersion using 6-cm round plastic dishes. Muscles were fixed by surgical thread knotted around the distal and proximal tendons. Visualization worked best after at least 24 h of temperature adjustment of the sample in the microscope room. During this period, the sample was kept in the dark.

Fiber Number and Image Analysis, Figure Preparation, and Statistics

Transversal EDL cryo-sections (15- μ m thick) from C57BL/10J mice were stained with WGA-488 (1:1,000 dilution in 2% BSA/PBS) for 15 min at RT to outline muscle fibers. After washing and embedding in Mowiol, sections were imaged with an inverted Leica SP8 microscope. After acquisition, all images were electronically processed using either Leica Microsystems LAS X core or ImageJ software. Signal-to-Noise-Ratio (SNR) measurements were done in ImageJ. Here, NMJs were segmented and mean intensities of the NMJs and standard deviation (SD) of adjacent fiber background regions were measured. The ratio of NMJ intensities vs. background SD was determined as SNR for each synapse. Numbers displayed in the text indicate the average of several SNR values per sample. For quantitative analysis of NMJ and fiber numbers, position of all observed NMJs / fibers was completed using the multi-point tool of ImageJ. This determined the xyz-position of the center of each NMJ / fiber. For analysis of critical morphological parameters of NMJs according to Jones et al. (2016), five square ROIs, each 500 \times 500 μ m, were selected per muscle. Then, all en face NMJs per ROI were manually thresholded and segmented using the magic wand tool in ImageJ. Then, area, perimeter and bounding rectangle diagonal were measured for every segmented NMJ. The number of AChR clusters per NMJs was counted manually. The diagonal of the bounding rectangle was calculated from the bounding rectangle sides while the fragmentation index was determined using the term: fragmentation index = $1 - [1 / (\text{number of AChR clusters})]$. Spectral un-mixing (Zimmermann et al., 2002) used the ImageJ plugin SpectralUnmixing (<https://imagej.nih.gov/ij/plugins/spectral-unmixing.html>). All figures were assembled

using Adobe Illustrator. Mean values and standard deviations were calculated in Microsoft Excel. Normal distribution and homo/heteroscedasticity of data were probed using Kolmogorov-Smirnov test and *F*-test, respectively. According to these results and the type of data, statistical significance was evaluated using either one-way Analysis of Variance (ANOVA) with Tukey's *post-hoc* test, unpaired two-tailed *t*-test, or Kruskal-Wallis test. Bar graphs are presented as mean \pm SD. *P*-values were indicated as * ($p < 0.05$), ** ($p \leq 0.01$), *** ($p \leq 0.001$), or **** ($p \leq 0.0001$). $P \geq 0.05$ was considered not significant.

RESULTS

An SDS-Free Hydrogel-Based Clearing Protocol Retains NMJ Staining

Previous attempts of optically clearing whole skeletal muscles using hydrogel-based, CLARITY-derived protocols yielded good tissue transparency but led to a quantitative loss of BGT fluorescence. To address possible reasons for this, we tested several variations of the procedure that was previously described by Milgroom and Ralston (2016). Samples were PFA fixed, embedded in hydrogel, and then stained with BGT-AF647 for NMJ labeling. Once stained, muscles were thoroughly washed for a minimum of 2 days, incubated in 88% glycerol overnight, and imaged to check for BGT-AF647 fluorescence. Notably, BGT-AF647 fluorescence was observed in all hydrogel-embedded samples (Supplementary Figure 1A, left panels). After initial imaging, glycerol was removed from the samples by washing for 24 h in PTwH at RT and were then actively cleared using an X-CLARITY tissue clearing system. A variety of settings, including different electrophoresis strengths, the addition of PFA fixation after BGT-AF647 staining, as well as a passive CLARITY protocol using a constant flow of SDS with no current, were tested. These modifications resulted in a reduced SNR of NMJ labeling in the cleared tissue (Supplementary Figure 1A, see lower left angles in panels for SNR values); samples that were post-fixed with PFA before clearing were less affected. However, also these re-fixed samples exhibited a large decrease in fluorescence intensity of the BGT-AF647 staining and were still far from acceptable quality. Thus, supporting the findings of previous studies which state the incompatibility of CLARITY-based protocols with BGT-NMJ staining.

The next step was to determine the effects of SDS on BGT staining: whether it washed out the membrane bound AChRs, simply quenched the fluorophore, or denatured the AChRs to the point BGT would not be able to bind. Samples were processed following the X-CLARITY protocol. Briefly, samples were PFA fixed, hydrogel embedded, actively cleared using an X-CLARITY machine, stained with either WGA-488 or BGT-AF647, and incubated in 88% glycerol for imaging. It was found here that staining the samples post-clearing with BGT-AF647 continued to result in an absence of NMJ signals, data not shown. However, NMJs in total were not destroyed by these techniques. Indeed, the lectin WGA could nicely identify the proteoglycan-rich ECM at the NMJs (Supplementary Figures 1B,C, see arrowheads in Supplementary Figure 1C for some examples of NMJs) besides

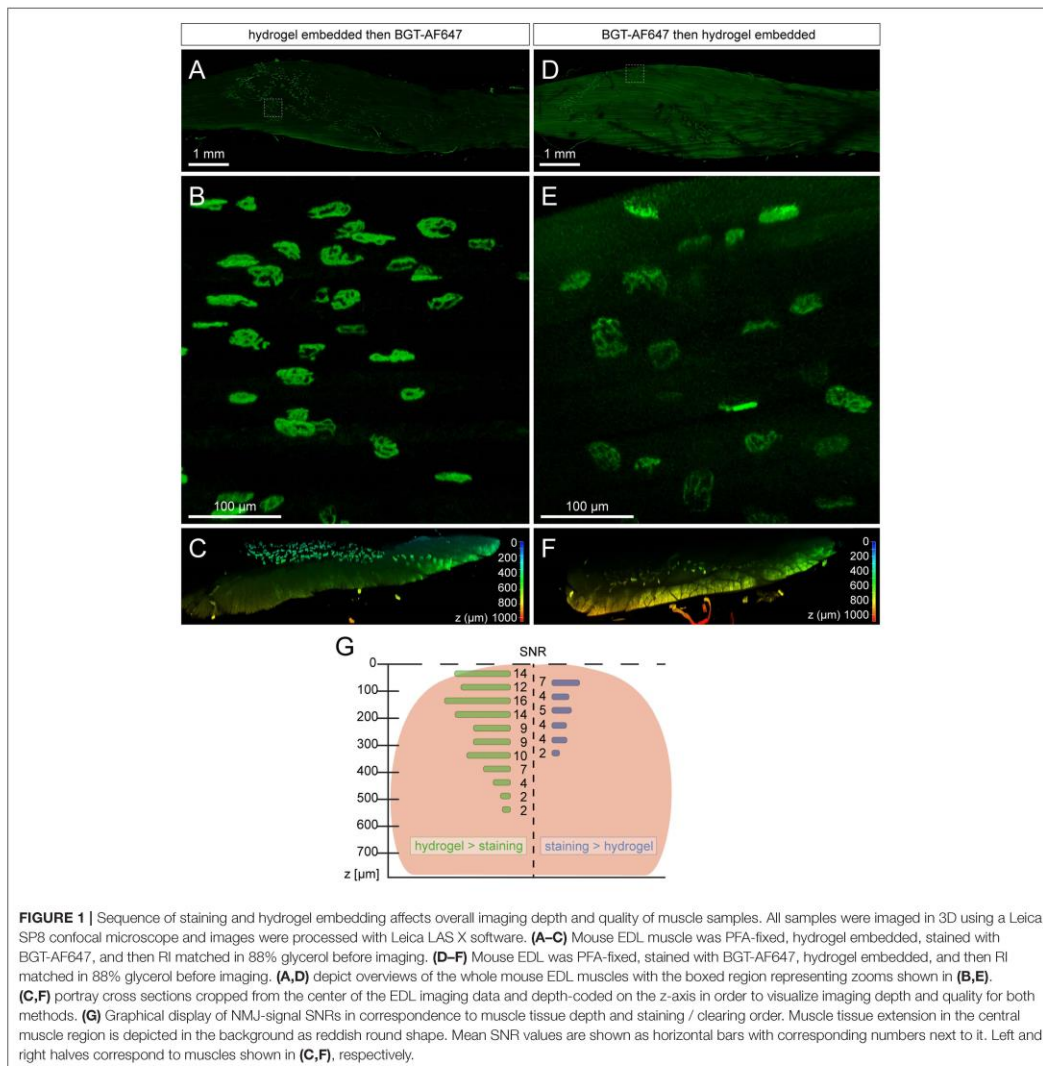
other structures, such as blood vessels. Therefore, it might be assumed that SDS caused either quenching of the fluorophores or that it denatured the AChRs. The latter would, in turn, release BGT-AF647 from the AChR for samples stained before clearing and impede BGT-AF647 from binding altogether for samples stained post-clearing. With this in mind, SDS was excluded from all other experiments due to its role as a potential risk factor for the maintenance of BGT binding sites on NMJs.

With the recent introduction of a new free-of-acrylamide SDS based tissue clearing protocol (Xu et al., 2017), the necessity of the embedded hydrogel and its effect on tissue needed to be explored. In theory, the embedded hydrogel not only homogenizes the RI throughout the sample but also increases the porosity of it; resulting in better penetration and uniformity of staining (Chung and Deisseroth, 2013; Chung et al., 2013). To test the effects of the hydrogel, samples were PFA fixed and either embedded in hydrogel, then stained with BGT-AF647 or vice versa. Both being compared in Figure 1, we found that staining samples after hydrogel embedding led to a better SNR (Figure 1G, Supplementary Figure 2) and increased the overall imaging depth of the sample (Figure 1G, Supplementary Figure 2). This confirmed the need of embedding samples with hydrogel and resulted in the final protocol termed MYOCLEAR. This method represents a passive hydrogel-based clearing method for the visualization of NMJs in fixed mouse muscles and is summarized in Figure 2.

Muscle Fibers, Nuclei, and NMJs Can Be Visualized by Virtue of Green/Red Autofluorescence and Spectral Unmixing of Near-Infrared Fluorescence Signals

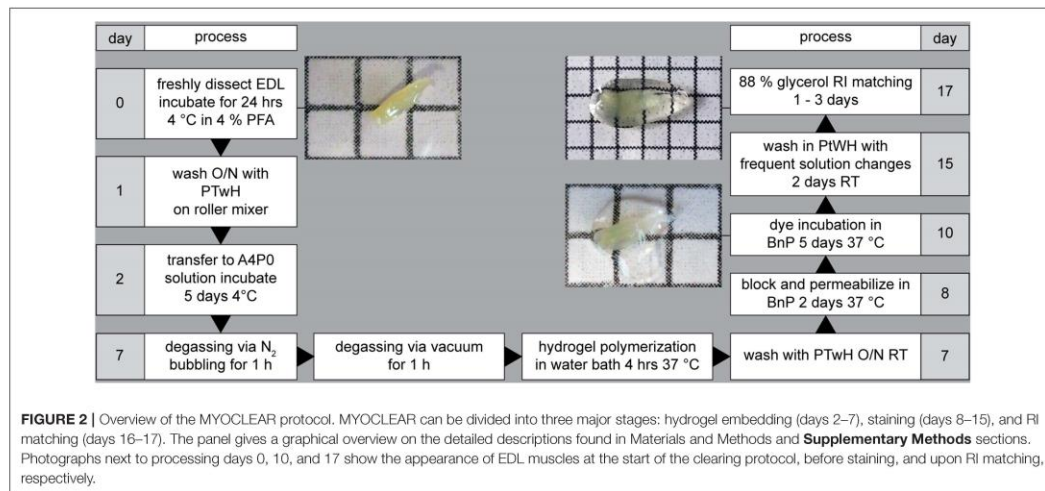
Number and position of myonuclei can serve as relevant parameters in muscle research. Specifically, detection of centronucleated fibers in diseased and regenerating muscle or analyzing the presence of fundamental subsynaptic nuclei at NMJs would need determination of these parameters. Thus, we sought to use Draq5, a near-infrared nuclear dye, in combination with a red-fluorescent BGT-AlexaFluor555 conjugate on MYOCLEAR-treated EDL muscles. As shown in red in Figures 3A,B, nuclei were well-stained and visible in the Draq5 channel. Conversely, NMJs, indicated by arrowheads in Figure 3B, were barely visible due to massive, PFA-induced autofluorescence (both shown in green). Consequently, this made the quality of these results inadequate for analysis. Furthermore, the intense level of autofluorescence was also observed in the 500–550 nm wavelength range when samples were stained with BGT-AlexaFluor488, data not shown.

To mitigate the autofluorescence-induced limitation observed in short-wavelength fluorescence channels, we utilized two slightly spectrally separated near-infrared dyes, BGT-AF647 (maxima of excitation and emission, 650 and 665 nm, respectively) and Draq5 (maxima of excitation and emission, 646 and 681 nm, respectively). Muscles were PFA fixed, hydrogel embedded, co-stained with the dyes mentioned above, incubated in 88% glycerol, and then imaged using a 633 nm wavelength excitation laser for both. Each dye was acquired separately and



their emission detection windows adjusted to 643–679 nm and 685–778 nm for BGT-AF647 and DraQ5, respectively. **Figure 3C** depicts a maximum-z projection of an EDL-whole mount scanned over a thickness of 1.2 mm. In addition, **Figure 3D** and **Supplementary Video S1** show a zoom view of the boxed region and a rotation of the data projection, respectively. Nuclei and NMJs could be clearly distinguished. An additional spectral un-mixing step (see chapter Fiber number and image analysis, figure preparation, and statistics) was then added for more

accurate segmentation results. **Figures 3E,F** show depth-coded side views of BGT-AF647 and DraQ5, respectively, and reveal a good signal penetration for both over a depth range of about 1 mm. **Figure 3F** displays some elongated structures, which likely represent blood vessels traversing the muscle. To assess the compatibility of MYOCLEAR with muscle types other than EDL, we applied the protocol to adult mouse diaphragm. Confocal analysis revealed that the procedure was good to achieve complete penetration of diaphragm muscle in z (**Figures 4A–D**).



The insert in **Figure 4A** shows that NMJs were well-preserved in these samples. The apparent fragmentation in the large overview in **Figure 4A** is due to nuclei partially covering many synapses.

Whole Mount Analysis Detects Local Heterogeneity of NMJ Fragmentation Index in mdx Muscle

Wildtype skeletal muscle, as tested so far, is characterized by extremely homogeneous tissue composition. Conversely, diseased muscles might exhibit large amounts of fibrosis, fatty tissue, immune cell aggregates, or other changes that can affect the optical characteristics of muscle tissue and their transparency after clearing. Thus, we looked at muscles from wildtype and dystrophic mdx mice. The latter are characterized by extensive fibrosis (Piñol-Jurado et al., 2018) and fragmented NMJs (Lyons and Slater, 1991; Röder et al., 2012). We found that applying MYOCLEAR to wildtype and mdx muscles resulted in data of comparable quality. As expected, NMJ structure was clearly different between the two; with wildtype NMJs displaying coherent pretzel-like structures and mdx NMJs demonstrating fragmented morphology. Next, whole mount imaging data was acquired for some wildtype and mdx mouse EDLs that were processed with MYOCLEAR and stained with BGT-AF647. The numbers of visible NMJs were then quantified by hand using the multi-point tool in ImageJ. Representative muscles are depicted in **Figures 5A,B** which illustrates the ability of this protocol to detect hundreds of NMJs. In quantitative terms, 1082.3 ± 29.5 and 1019.5 ± 14.8 (each mean \pm SD) NMJs were counted in wildtype and mdx muscles, respectively. **Figures 5A,B'** show representative high-power images of a few NMJs from each of the corresponding muscles. These panels demonstrate the normal, pretzel-like structure of NMJs in wildtype (**Figure 5A'**) as compared to the fragmented appearance

in the mdx muscle (**Figure 5B'**). An important advantage of whole mounts should be that heterogeneity of objects or effects of treatments within the entire organ can be better observed than in individual tissue sections. To assess this point, key morphological parameters of NMJs from different ROIs of both, wildtype and mdx muscles were determined and compared. Therefore, a subset of criteria recently introduced by Jones et al. was applied (Jones et al., 2016). In detail, area, fragmentation index, perimeter, and bounding rectangle diagonal of NMJs from five different ROIs (**Figures 5C–F**) per muscle were determined. NMJ areas, perimeters, and bounding rectangle diagonals were similar between all ROIs of a given muscle and also apparently not different between wildtype and mdx. Conversely, NMJ fragmentation index was higher in mdx than in wildtype and, furthermore, varied considerably within a given mdx muscle.

VACHT Antibody Staining Confirms Integrity of NMJ Presynaptic Apparatus Upon MYOCLEAR

BGT-AF647 and lectin staining data suggested that the NMJ ECM and postsynaptic apparatus remained intact during MYOCLEAR processing. To address presynaptic integrity and the amenability of the clearing protocol for immunofluorescence staining, we first processed EDL muscles with the MYOCLEAR protocol and then stained nuclei and the presynaptic NMJ marker protein vAChT using Draq5 and anti-vAChT antibody, respectively. As depicted in **Figure 6A**, the obtained antibody staining was concentrated in the NMJ regions, although considerable noisy signals were also observed outside the synaptic regions. Yet, NMJ presynapses showed normal coherent appearance, demonstrating that the clearing procedure did not affect this part either. The general integrity of the major muscle compartment was also confirmed by immunostaining with a

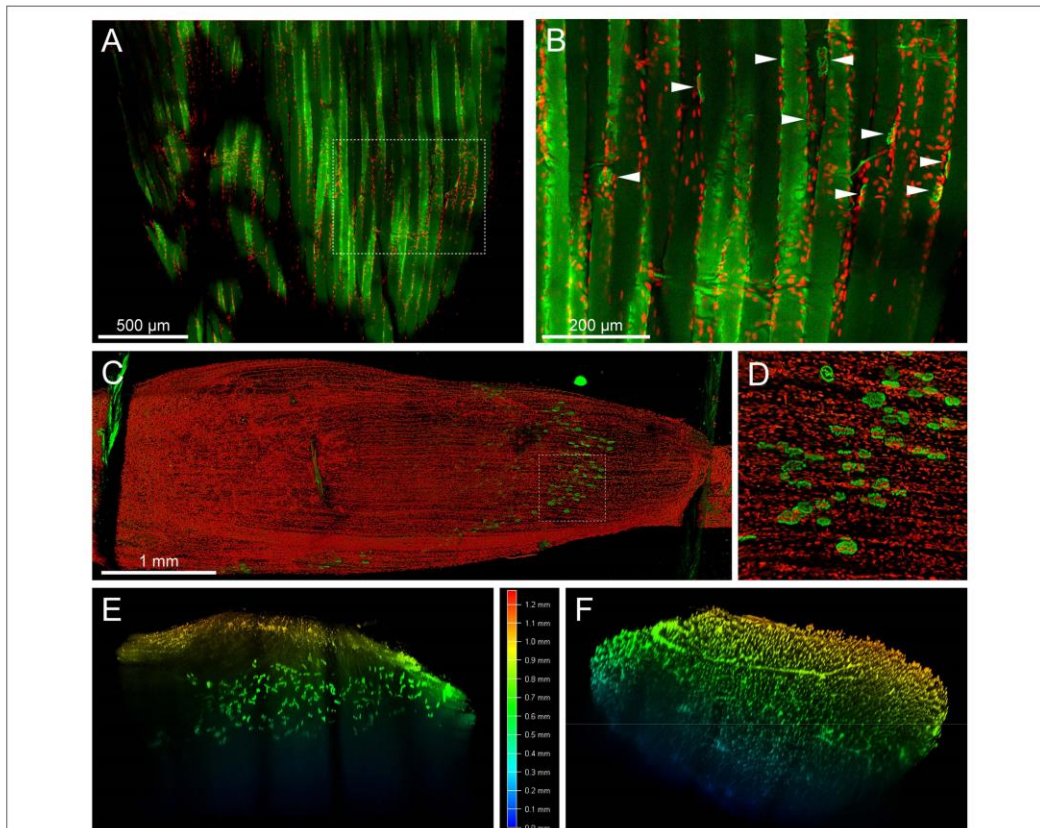


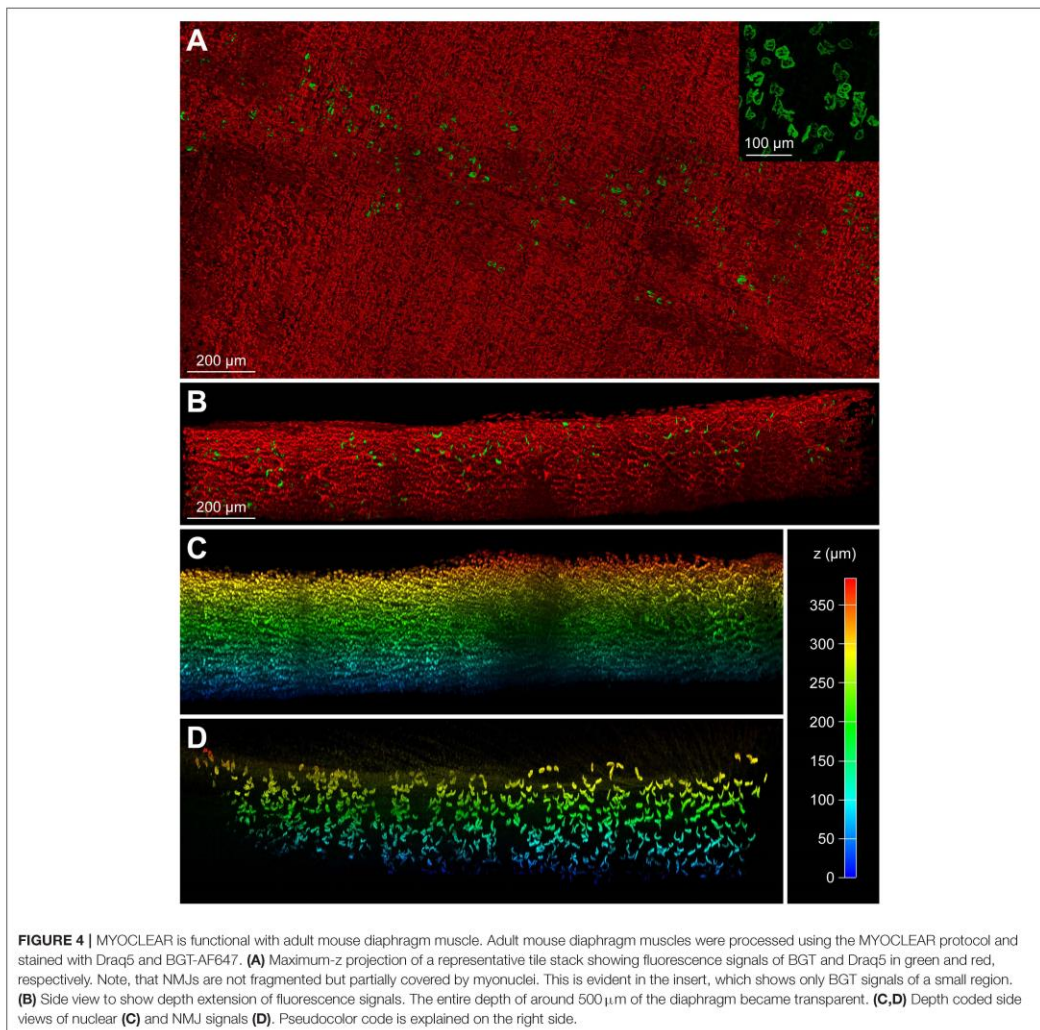
FIGURE 3 | MYOCLEAR enables imaging of muscle fibers, myonuclei, and NMJs by using red autofluorescence and spectral unmixing of far-red wavelengths dyes. **(A,B)** Mouse EDL was processed via the MYOCLEAR protocol and stained with BGT-AF555 and Draq5. **(A)** depicts a confocal section of the EDL, with **(B)** representing a zoom of the boxed region. Strong autofluorescence of the tissue in the AF555 channel (green) resulted in a poor SNR for NMJ detection (some NMJs are highlighted in **B**, arrowheads). In contrast, the near-infrared dye Draq5 displayed crisp and clear nuclei. **(C–F)** Mouse EDL muscle was processed via the MYOCLEAR protocol and stained with BGT-AF647 and Draq5. In order to overcome the auto-fluorescence shown in this figure, the emission windows for each dye were adjusted according to their peak values and acquired separately using the same 633-nm excitation laser on a SP8 confocal microscope. The images were processed using Leica LAS X software and spectrally un-mixed in ImageJ. **(C)** Maximum-z projection of the whole EDL before applying spectral un-mixing. Draq5, red; BGT-AF647, green. Green autofluorescence of the thread keeping the muscle in place for imaging is visible at the proximal and distal ends of the muscle. **(D)** Zoom view of the boxed region in **(A)**. **(E,F)** Z-axis depth coding for signals of BGT-AF647 **(E)** and Draq5 **(F)** shown as cross sections after spectral un-mixing.

few additional antibodies. Nicely, dystrophin outlined muscle fibers and was also enriched in the NMJ regions as expected (**Figure 6B**). Further labeling with collagen I antibody showed the distribution of large blood vessels, capillaries, and fascia cells (**Figure 6C**). Finally, immunostaining of troponin I retrieved the regular pattern of sarcomeric striations (**Figure 6D**).

DISCUSSION

Although previous attempts of optically clearing whole skeletal muscles using hydrogel-based, CLARITY-derived protocols

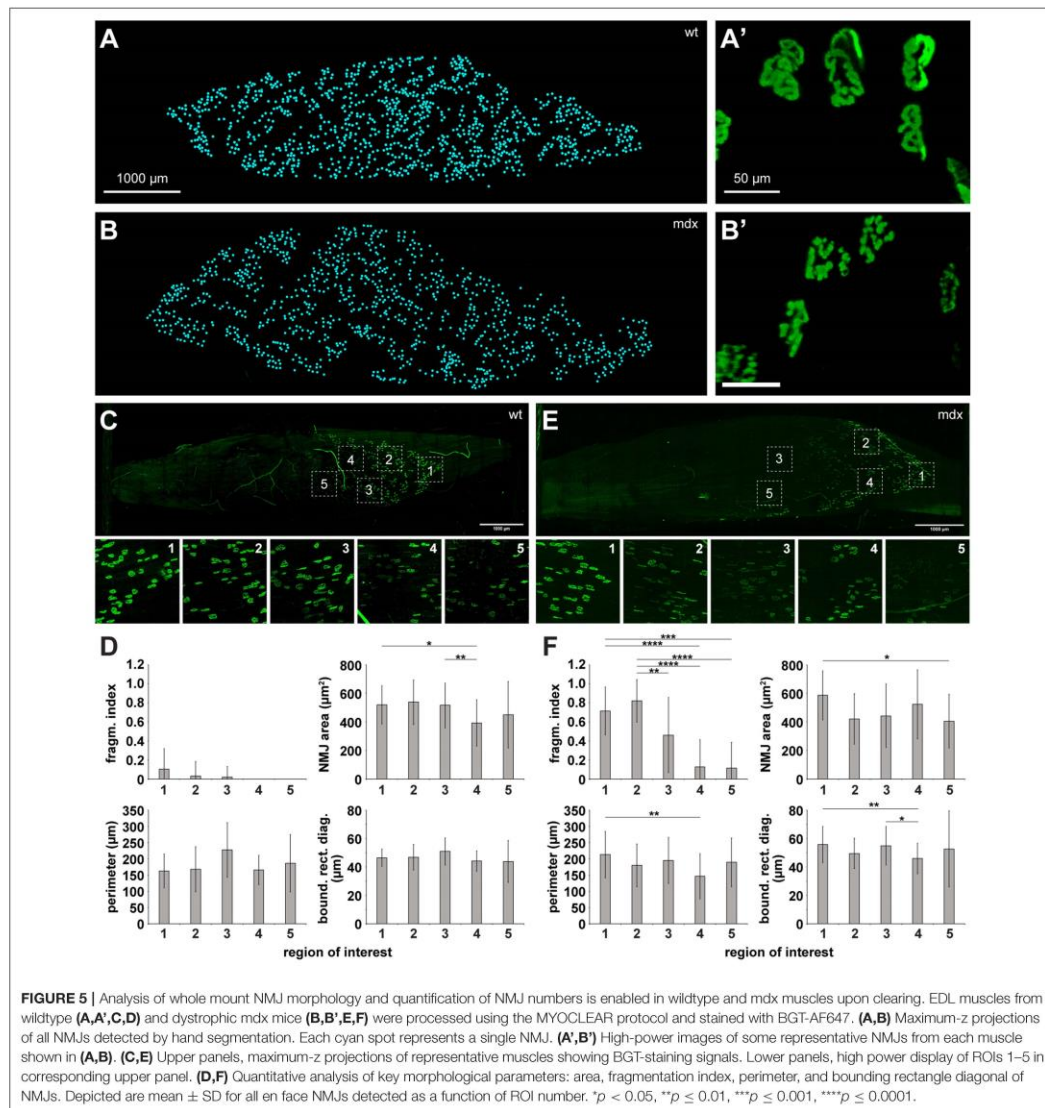
yielded sufficient muscle tissue transparency, they led to a quantitative loss of BGT fluorescence. This was true for both, active (Milgroom and Ralston, 2016) and passive CLARITY protocols (Zhang et al., 2018). The interpretation in these studies was that hydrogel cross-linking coupled with PFA fixation prevented access of the toxin to AChRs. Conversely, we present a hydrogel and PFA based skeletal muscle clearing protocol that nicely retains BGT-based NMJ staining and exhibits a good light penetration of approximately 1,000 μm in mouse EDL muscle. This suggests, that SDS rather than hydrogel or PFA led to the loss of BGT staining. For simplicity, this method was termed MYOCLEAR. It allows for the analysis of whole mount NMJ



counts in correlation to myonuclei analysis and is also compatible with diaphragm, as well as with other dyes, including lectins and antibodies. Given that the protocol is based on an initial PFA fixation step, it should be compatible with easy handling and material exchange.

Permutation of the protocol settings revealed that staining and image quality were superior if BGT labeling occurred after PFA fixation and hydrogel embedding. Since both methods (i.e., staining before or after hydrogel embedding) received ample washing steps, it is safe to assume the hydrogel either supports BGT-AF647 in a way that it can reach its target more accurately or

aids in washing out unspecific BGT-AF647 signals. The present protocol presents strong autofluorescence in the blue to red fluorescence wavelength range, which is most likely due to PFA-fixation induced chromophore formation (Baschong et al., 2001). In the near infrared range, though, the autofluorescence issue was not present and thus AlexaFluo647 and Draq5 dyes worked well. Although the autofluorescence obtained in the green and red fluorescence channels might be considered a limitation of the MYOCLEAR protocol, it can also be rather useful for tracking individual muscle fibers over their whole length. Additionally, it can be used to assess pathophysiologically relevant features,



including centro-nucleated regions, fiber atrophy, fiber splitting, the occurrence of poly-innervation, and other general structural information.

Given that most standard available fluorescence microscopy systems exhibit excitation lasers typically up to 633 nm wavelength, the use of near infrared dyes compatible with MYOCLEAR is somewhat limited. To permit at least two different structures to be simultaneously marked, we used the

slightly wavelength-shifted dyes AlexaFluor647 and Draq5 in combination with spectral unmixing (Zimmermann et al., 2002). Using hand segmentation of BGT-AF647 stained and cleared EDL wholemounts, slightly more than one thousand NMJs were identified in each muscle. According to literature, the amount of muscle fibers in an adult mouse EDL ranges from 758 to 1,147 (White et al., 2010; Bloemberg and Quadrilatero, 2012). To confirm this, we performed fiber counts from our own

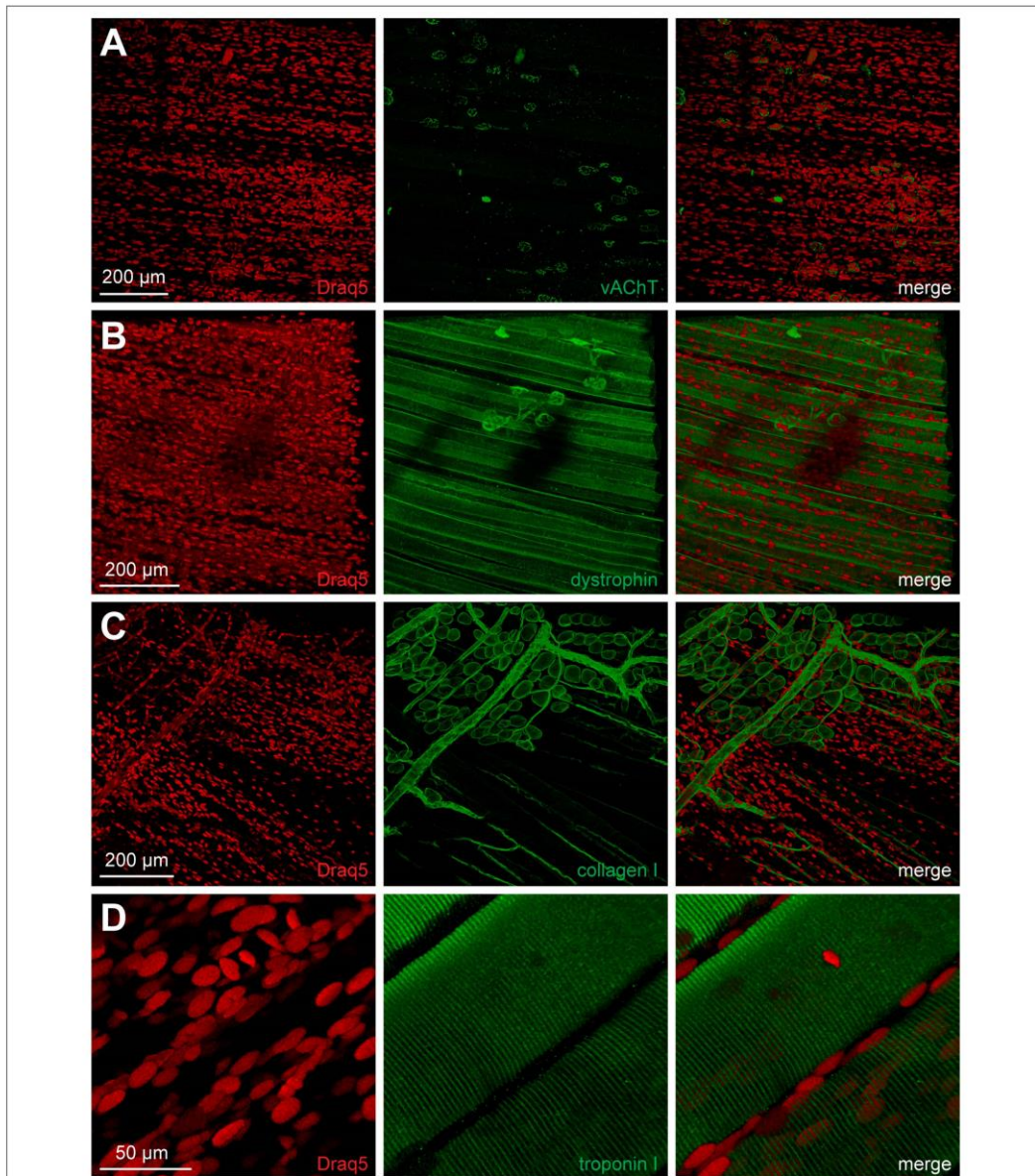


FIGURE 6 | Integrity of NMJ presynapse and other muscle structures is maintained upon clearing. Adult mouse EDL muscles were processed using the MYOCLEAR protocol and co-stained with DraQ5 and antibodies against either NMJ presynapse (**A**, vAChT), sarcolemma (**B**, dystrophin), ECM (**C**, collagen I), or sarcomere (**D**, troponin I). Images show maximum-z projections of confocal z-stacks with an interplane interval of 2 μm and depths from muscle surface of 466, 665, 104, and 214 μm for (**A–D**), respectively.

animals by analyzing cross sections of contralateral muscles. This revealed fiber numbers of $1,052 \pm 42$ (mean \pm SD) per EDL muscle. Thus, taking into account that each muscle fiber in adult muscle is innervated by one single NMJ (Krause, 1863), this finding supports that the total number of NMJs obtained in our cleared muscles represents most, if not all, of the NMJs in the tissue. However, it must be stated that NMJs beyond a depth of about 700 to 800 μm from the surface were hardly above background and would render automated segmentation, volumetric, or in-depth morphological analyses of these synapses impossible. If such information is needed, it would be necessary to image muscles from both sides and eliminate the overlapping NMJs.

MYOCLEAR was found to retain morphological integrity of presynapse, synaptic cleft, and postsynapse. In many experimental paradigms, considerable regional heterogeneity of critical morphological parameters of the neuromuscular apparatus might be expected, such as for NMJ degeneration/regeneration in dystrophic mouse models (Haddix et al., 2018), terminal sprouting upon neurotoxin application (Wright et al., 2007; Duregotti et al., 2015), or in aging muscle (Valdez et al., 2010). Therefore, a more holistic picture of observed changes in the whole mount might yield relevant new insights. For wildtype and mdx EDL muscles, we addressed the principal applicability of our samples to study a subset of morphological criteria as recently proposed by Jones et al. (2016). This revealed differences with respect to the amplitude and regional heterogeneity of NMJ fragmentation index between wildtype and mdx, suggesting that whole mount analysis might serve as a valuable tool for future investigations of neuromuscular disorders. Certainly, immunofluorescence procedures will be a relevant asset to perform more in-depth analyses in this context. Thus, it was evaluated, whether the present clearing protocol is compatible with antibody staining. Indeed, immunostaining with all tested antibodies against presynapse (vAChT), sarcomere (troponin I), sarcolemma (dystrophin), and extracellular matrix (collagen I) yielded the expected staining patterns, although depth penetration still needs to be optimized. Apart from vAChT, which was visible beyond 500 μm deep in the tissue, the other markers were visible only for about 200–300 μm of depth. It will be necessary to examine if additional techniques for dye distribution, such as stochastic electrotransport or similar procedures (Kim et al., 2015; Nehrhoff et al., 2016) might solve the issue of penetration. Also, the limitation of MYOCLEAR to near-infrared dyes requests evaluation of further dye combinations that would be compatible with AF647 and DraQ5. We tested secondary antibodies coupled to PE-Cy7, but were not successful due to low secondary antibody specificity.

REFERENCES

Baschong, W., Suetterlin, R., and Laeng, R. H. (2001). Control of Autofluorescence of Archival Formaldehyde-fixed, Paraffin-embedded Tissue in Confocal Laser Scanning Microscopy (CLSM). *J. Histochem. Cytochem.* 49, 1565–1571. doi: 10.1177/002215540104901210

In summary, future work will have to deal with skeletal muscle clearing protocols that are compatible with a wider spectral range to incorporate more than just two dyes in one sample as well as with reaching a higher depth penetration of antibodies. Furthermore, besides improving the MYOCLEAR protocol, an automated quantitative determination of NMJ numbers and characteristics, such as size and fragmentation, would likely be a major analytical request for cleared muscles. We have started to work on such automated detection algorithms, but they need further improvement before being valid. Though, **Supplementary Video S2** shows a future prospect of advantages of such an approach. It depicts a 3D view of all NMJs detected in the muscle sample shown in **Figure 5C**. Yellow-coded NMJs were detected by auto segmentation, blue NMJs were detected by hand. It is evident that three-dimensional information gives a much more plastic view on the synapse band in this muscle.

ETHICS STATEMENT

This study was carried out in accordance with the recommendations of EC directive 2010/63. The protocol was approved by the Regierungspräsidium Karlsruhe.

AUTHOR CONTRIBUTIONS

MW, MRi, TS, SH, and MRe performed the experiments and analyzed data. MW, MT, NG, MH, and RR planned experiments, contributed material, and wrote the paper.

FUNDING

RR is funded by DFG grant RU923/8-2. This work was funded by the German Federal Ministry of Research (BMBF) as part of the Innovation Partnership M²Aind, project M²OGA (03FH8I021A) within the framework Starke Fachhochschulen—Impuls für die Region (FH-Impuls). MW and MRi are fellows of the graduate training group TASCdT funded by the Ministerium für Wissenschaft, Forschung und Kunst Baden-Württemberg. SH is a fellow of the Albert-und-Anneliese-Konanz Stiftung.

ACKNOWLEDGMENTS

We are grateful to the animal facility for animal care.

SUPPLEMENTARY MATERIAL

The Supplementary Material for this article can be found online at: <https://www.frontiersin.org/articles/10.3389/fncel.2019.00049/full#supplementary-material>

Bloemberg, D., and Quadrilatero, J. (2012). Rapid determination of myosin heavy chain expression in rat, mouse, and human skeletal muscle using multicolor immunofluorescence analysis. *PLoS ONE* 7:e35273. doi: 10.1371/journal.pone.0035273

Carnio, S., LoVerso, F., Baraibar, M. A., Longa, E., Khan, M. M., Maffei, M., et al. (2014). Autophagy impairment in muscle induces neuromuscular

- junction degeneration and precocious aging. *Cell Rep.* 8, 1509–1521. doi: 10.1016/j.celrep.2014.07.061
- Chen, W., Yu, T., Chen, B., Qi, Y., Zhang, P., Zhu, D., et al. (2016). *In vivo* injection of α -bungarotoxin to improve the efficiency of motor endplate labeling. *Brain Behav.* 6:e00468. doi: 10.1002/brb3.468
- Chung, K., and Deisseroth, K. (2013). CLARITY for mapping the nervous system. *Nat. Methods* 10, 508–513. doi: 10.1038/nmeth.2481
- Chung, K., Wallace, J., Kim, S.-Y., Kalyanasundaram, S., Andalman, A. S., Davidson, T. J., et al. (2013). Structural and molecular interrogation of intact biological systems. *Nature* 497, 332–337. doi: 10.1038/nature12107
- Dobrowolny, G., Martini, M., Scicchitano, B. M., Romanello, V., Boncompagni, S., Nicoletti, C., et al. (2018). Muscle expression of *SOD1 G93A* triggers the dismantlement of neuromuscular junction via PKC-theta. *Antioxid. Redox Signal.* 28, 1105–1119. doi: 10.1089/ars.2017.7054
- Du, H., Hou, P., Zhang, W., and Li, Q. (2018). Advances in CLARITY-based tissue clearing and imaging. *Exp. Ther. Med.* 16, 1567–1576. doi: 10.3892/etm.2018.6374
- Duregotti, E., Zanetti, G., Scorzeo, M., Megighian, A., Montecucco, C., Pirazzini, M., et al. (2015). Snake and spider toxins induce a rapid recovery of function of botulinum neurotoxin paralysed neuromuscular junction. *Toxins* 7, 5322–5336. doi: 10.3390/toxins7124887
- Gorio, A., Carmignoto, G., Finesso, M., Polato, P., and Nunzi, M. G. (1983). Muscle reinnervation—II. Sprouting, synapse formation and repression. *Neuroscience* 8, 403–416.
- Greenbaum, A., Chan, K. Y., Dobрева, T., Brown, D., Balani, D. H., Boyce, R., et al. (2017). Bone CLARITY: clearing, imaging, and computational analysis of osteoprogenitors within intact bone marrow. *Sci. Transl. Med.* 9:eaa6518. doi: 10.1126/scitranslmed.aah6518
- Haddix, S. G., Lee, Y. L., Kornegay, J. N., and Thompson, W. J. (2018). Cycles of myofiber degeneration and regeneration lead to remodeling of the neuromuscular junction in two mammalian models of Duchenne muscular dystrophy. *PLoS ONE* 13:e0205926. doi: 10.1371/journal.pone.0205926
- Jones, R. A., Reich, C. D., Dissanayake, K. N., Kristmundsdottir, F., Findlater, G. S., Ribchester, R. R., et al. (2016). NMJ-morph reveals principal components of synaptic morphology influencing structure–function relationships at the neuromuscular junction. *Open Biol.* 6:160240. doi: 10.1098/rsob.160240
- Khan, M. M., Lustrino, D., Silveira, W. A., Wild, E., Straka, T., Issop, Y., et al. (2016). Sympathetic innervation controls homeostasis of neuromuscular junctions in health and disease. *Proc. Natl. Acad. Sci. U.S.A.* 113, 746–750. doi: 10.1073/pnas.1524272113
- Kim, S.-Y., Cho, J. H., Murray, E., Bakh, N., Choi, H., Ohn, K., et al. (2015). Stochastic electrotransport selectively enhances the transport of highly electromobile molecules. *Proc. Natl. Acad. Sci. U.S.A.* 112, E6274–E6283. doi: 10.1073/pnas.1510133112
- Kleffel, S., Lee, N., Lezcano, C., Wilson, B. J., Sobolewski, K., Saab, K. R., et al. (2016). ABCB5-targeted chemoresistance reversal inhibits merkel cell carcinoma growth. *J. Invest. Dermatol.* 136, 838–846. doi: 10.1016/j.jid.2015.12.038
- Krause, W. (1863). Über die endigung der muskelnerven. Zweiter artikel. *Zeitschrift. Rat. Med.* 20, 1–18.
- Lee, H., Park, J.-H., Seo, I., Park, S.-H., and Kim, S. (2014). Improved application of the electrophoretic tissue clearing technology, CLARITY, to intact solid organs including brain, pancreas, liver, kidney, lung, and intestine. *BMC Dev. Biol.* 14:48. doi: 10.1186/s12861-014-0048-3
- Lee, Y. L., Thompson, W. J., and Harlow, M. L. (2017). Schwann cells participate in synapse elimination at the developing neuromuscular junction. *Curr. Opin. Neurobiol.* 47, 176–181. doi: 10.1016/j.conb.2017.10.010
- Lu, J., and Lichtman, J. W. (2007). Imaging the neuromuscular junction over the past centuries. *Sheng Li Xue Bao* 59, 683–696.
- Lyons, P. R., and Slater, C. R. (1991). Structure and function of the neuromuscular junction in young adult mdx mice. *J. Neurocytol.* 20, 969–981.
- Milgroom, A., and Ralston, E. (2016). Clearing skeletal muscle with CLARITY for light microscopy imaging. *Cell Biol. Int.* 40, 478–483. doi: 10.1002/cbin.10578
- Nehrhoff, I., Bocancea, D., Vaquero, J., Vaquero, J. J., Ripoll, J., Desco, M., et al. (2016). 3D imaging in CUBIC-cleared mouse heart tissue: going deeper. *Biomed. Opt. Express.* 7, 3716–3720. doi: 10.1364/BOE.7.003716
- Piñol-Jurado, P., Suárez-Calvet, X., Fernández-Simón, E., Gallardo, E., de la Oliva, N., Martínez-Muriana, A., et al. (2018). Nintedanib decreases muscle fibrosis and improves muscle function in a murine model of dystrophinopathy. *Cell Death Dis.* 9:776. doi: 10.1038/s41419-018-0792-6
- Renier, N., Wu, Z., Simon, D. J., Yang, J., Ariel, P., and Tessier-Lavigne, M. (2014). iDISCO: a simple, rapid method to immunolabel large tissue samples for volume imaging. *Cell* 159, 896–910. doi: 10.1016/j.cell.2014.10.010
- Röder, I. V., Strack, S., Reischl, M., Dahley, O., Khan, M. M., Kassel, O., et al. (2012). Participation of myosin Va and Pka type I in the regeneration of neuromuscular junctions. *PLoS ONE* 7:e40860. doi: 10.1371/journal.pone.0040860
- Rudolf, R., Khan, M. M., Labeit, S., and Deschenes, M. R. (2014). Degeneration of neuromuscular junction in age and dystrophy. *Front. Aging. Neurosci.* 6:99. doi: 10.3389/fnagi.2014.00099
- Tomer, R., Ye, L., Hsueh, B., and Deisseroth, K. (2014). Advanced CLARITY for rapid and high-resolution imaging of intact tissues. *Nat. Protoc.* 9, 1682–1697. doi: 10.1038/nprot.2014.123
- Valdez, G., Tapia, J. C., Kang, H., Clemenson, G. D., Gage, F. H., Lichtman, J. W., et al. (2010). Attenuation of age-related changes in mouse neuromuscular synapses by caloric restriction and exercise. *Proc. Natl. Acad. Sci. U.S.A.* 107, 14863–14868. doi: 10.1073/pnas.100220107
- Wang, Z., Zhang, J., Fan, G., Zhao, H., Wang, X., Zhang, J., et al. (2018). Imaging transparent intact cardiac tissue with single-cell resolution. *Biomed. Opt. Express.* 9:423. doi: 10.1364/BOE.9.000423
- White, R. B., Bierinx, A.-S., Gnocchi, V. F., and Zammit, P. S. (2010). Dynamics of muscle fibre growth during postnatal mouse development. *BMC Dev. Biol.* 10:21. doi: 10.1186/1471-213X-10-21
- Wright, M. C., Cho, W.-J., and Son, Y.-J. (2007). Distinct patterns of motor nerve terminal sprouting induced by ciliary neurotrophic factor vs. Botulinum toxin. *J. Comp. Neurol.* 504, 1–16. doi: 10.1002/cne.21439
- Wu, H., Barik, A., Lu, Y., Shen, C., Bowman, A., Li, L., et al. (2015). Slit2 as a β -catenin/Cttnb1-dependent retrograde signal for presynaptic differentiation. *Elife* 4:e07266. doi: 10.7554/eLife.07266
- Xu, N., Tamadon, A., Liu, Y., Ma, T., Leak, R. K., Chen, J., et al. (2017). Fast free-of-acrylamide clearing tissue (FACT)—an optimized new protocol for rapid, high-resolution imaging of three-dimensional brain tissue. *Sci. Rep.* 7:9895. doi: 10.1038/s41598-017-10204-5
- Yang, B., Treweek, J. B. B., Kulkarni, R. P. P., Deverman, B. E. E., Chen, C.-K., Lubbeck, E., et al. (2014). Single-cell phenotyping within transparent intact tissue through whole-body clearing. *Cell* 158, 945–958. doi: 10.1016/j.cell.2014.07.017
- Zhang, W., Liu, S., Zhang, W., Hu, W., Jiang, M., Tamadon, A., et al. (2018). Skeletal muscle CLARITY: a preliminary study of imaging the three-dimensional architecture of blood vessels and neurons. *Cell J.* 20, 132–137. doi: 10.22074/cellj.2018.5266
- Zimmermann, T., Rietdorf, J., Girod, A., Georget, V., and Pepperkok, R. (2002). Spectral imaging and linear un-mixing enables improved FRET efficiency with a novel GFP2-YFP FRET pair. *FEBS Lett.* 531, 245–249. doi: 10.1016/s0014-5793(02)03508-1

Conflict of Interest Statement: The authors declare that the research was conducted in the absence of any commercial or financial relationships that could be construed as a potential conflict of interest.

Copyright © 2019 Williams, Rigon, Straka, Hörner, Thiel, Gretz, Hafner, Reischl and Rudolf. This is an open-access article distributed under the terms of the Creative Commons Attribution License (CC BY). The use, distribution or reproduction in other forums is permitted, provided the original author(s) and the copyright owner(s) are credited and that the original publication in this journal is cited, in accordance with accepted academic practice. No use, distribution or reproduction is permitted which does not comply with these terms.

Acknowledgements

Although a PhD project is a highly personal endeavour, its successful completion would not have been possible without the critical help and support of numerous people. I express my gratitude to the Landesgraduiertenförderung programme and Hochschule Mannheim for the funding provided in these years. I am grateful to my research group, led by Prof. Rüdiger Rudolf that I thank for the restless support, contribute and oversight during these years. I thank Prof. N. Gretz, Prof. M Hafner, Prof. K Bieback for their valuable insights and help during the project.

In particular, I will be always grateful to many people who helped me in these years : Tatjana, Max, Sarah, Elena and Julia for sharing the PhD experience, for teaching each other and learning together; Franziska for having guided me in my first critical weeks in a new lab ; Fabiola, Cristina, Daniela, Stefania, Sara, Adriana for their honest friendship and the moral and technical support within the TASCOT group ; Sina, who helped to navigate in the bureaucracy of german university ; Viktoria and Alex for those countless hours spent in the animal house together ; Elina, an anchor in reality and person of unbelievable support; Patrick for all the work and the fun together; Diego for the relentlessness in helping and partying in the same measure.

I thank my family, as with their help I was able to gain the instruments that brought me at the end of this PhD and I thank Maddalena, for the continuous support and love in these years, and with the firm believe we will continue to have each other backs, no matter what.

9. Curriculum vitae

PERSONAL INFORMATION



Matteo Rigon

📍 Neuweilerstrasse 108, 4054 Basel (SWITZERLAND)

☎ +49 16091023869

✉ rigonmatteo1@gmail.com
matteo.rigon@medma.uni-heidleberg.de

💬 [matteo.rigon1 \(Skype\)](https://www.skype.com/user/matteo.rigon1)
www.linkedin.com/in/matteo-rigon-4710991a3 (Linkedin)

Male

📅 Date of birth 29/06/1990

🇮🇹 Nationality Italian

WORK EXPERIENCE

- Sep 2016-present PhD student in the cooperative research training group “Tissue Analytics for Stem Cell-based Diagnostics and Therapy”.
Heidelberg University (Medical Faculty of Mannheim) in collaboration with Mannheim University of Applied Sciences, Paul-Wittsackstr. 10, 68163 Mannheim (GERMANY) and Center of Medical Research, University Hospital Mannheim, Theodor-Kutzer-Ufer 1-3, 68167 Mannheim (GERMANY)
- Mar 2015-Jul 2016 Master degree traineeship (12 months) at Istituto di Ricerca Pediatrica (IRP) Fondazione Città della Speranza, Stem Cell and Regenerative Medicine laboratory.
IRP, via della Ricerca Scientifica 2, 35127 Padova (ITALY) – Lab Reg Med 7 floor south
- Jun 2014-Dec 2014 Bachelor degree traineeship (6 months) at Vallisneri Biology Department (University of Padua), MOLBINFO laboratory.
Dipartimento di Biologia Vallisneri, via U. Bassi 58b, 35131 Padova (ITALY)

EDUCATION AND TRAINING

- 2016-2020(expected) PhD in **Translational Medicine**
Universität Heidelberg
Thesis: "Stem Cell-Induced Regeneration of Skeletal Muscle"
- 2013-2016 Master of Science in **Industrial Biotechnology**
Università degli Studi di Padova
Thesis: "Induced Pluripotent Stem Cells from Amniotic Fluid Cells Towards Muscle Commitment: Characterization and Protocol Evaluation"
- 2009-2013 Bachelor degree in **Biotechnology**
Università degli Studi di Padova
Thesis: "Protein Homology Modelling. Viral Hemagglutinin Models and Structure Production and Comparison"

PUBLICATIONS

- **Rigon M**, Bieback K, Gretz N, Hafner M, Rudolf R (2020) "Effects of ASC application on NMJ regeneration upon glycerol-induced muscle damage" Front. Mol. Neurosc. <https://doi.org/10.3389/fnmol.2020.00107>
- Rodella A, Pozzobon M, **Rigon M**, Franchin C, Arrigoni G, Simonato M, Ghinelli E, Vedovelli L (2019) Topical application of lyophilized and powdered human amniotic membrane promotes diabetic ulcer healing. Wound Medicine, 27:1. doi: 10.1016/j.wndm.2019.100171
- Williams MPI, **Rigon M**, Straka T, Hörner SJ, Thiel M, Gretz N, Hafner M, Reischl M and Rudolf R (2019) A Novel Optical Tissue Clearing Protocol for Mouse Skeletal Muscle to Visualize Endplates in Their Tissue Context. Front. Cell. Neurosci. 13:49. doi: 10.3389/fncel.2019.00049

PERSONAL SKILLS

| | | | | | |
|-------------------|---------------|---------|--------------------|-------------------|---------|
| Mother tongue | Italian | | | | |
| Other language(s) | UNDERSTANDING | | SPEAKING | | WRITING |
| | Listening | Reading | Spoken interaction | Spoken production | |
| English | C1 | C1 | C1 | C1 | C1 |

Communication skills

- good communication skills to other professionals, acquired with constant training by scientific presentation at Mannheim University of Applied Sciences (in English) (2016-2019).
- good communication skills to the public, acquired as member of the Native Science network (in Italian and English) (2019) and as collaborator for career orienting and scientific knowledge divulgation at A. Cornaro Scientific High School, Padova (in Italian and English) (2014-2016).

- Organisational / managerial skills
- I schedule my work in order to accomplish the goals set in a short time, although maintaining a certain degree of flexibility in order to face possible changes in the work practice or in the deadlines.
 - I am willing to assume responsibility position and to schedule other colleagues work (always with their agreement and behaving considering the working group hierarchy).
 - I always make myself available for training students or other colleagues or to help collaborators, according to mine and their work schedule.

- Job-related skills
- Optical microscopy (phase contrast and fluorescence).
 - Confocal microscopy (also Digital Lightsheet technology) to generate both 2D and 3D data.
 - Tissue clearing (solvent-based and refracting index matching based, as CLARITY and MYOCLEAR); tissue decellularization (detergent-enzymatic method).
 - Certified to work in an animal house in the European Union and Switzerland (FELASA-B).
 - Immunofluorescence and immunohistochemical staining (cells and tissues); sample preparation (dissection, freezing and processing at the cryostat).
 - Molecular biology: DNA and RNA extraction, isolation and quantification (Nanodrop); PCR (quantitative and semi quantitative with LightCycler, using SYBR Green method); electrophoresis assay.
 - Cellular biology: culture, expansion, storing of stem cells (ES or iPS), muscle progenitor cells (human and murine), human amniotic fluid cells; human amniotic fluid cells isolation and selection (paramagnetic microbeads method, for c-kit+ cells); MTS vitality assay.
 - Bioinformatics: effective use of molecular biology databases and tools (like BLAST), UCSF Chimera software, protein homology modelling (automatic).

Digital competence

- ImageJ /FIJI version: very good (image manipulation, data analysis)
- Leica Application Suite X: very good (as program for confocal microscopy and for image post-processing)
- Aperio Imagescope: good
- Huygens: sufficient
- Imaris: sufficient
- Microsoft Office (Word, Excel, PowerPoint): very good
- Photoshop: good
- Prism Graphpad: good
- Operative system (Windows): very good
- Certified SAS (9.1) user

Hobbies and interests

- I am an avid science-fiction reader.
- I have a great interest in science communication to the public. At the moment I am involved in the “Native Scientist” initiative for science divulgation to pupils (for more information, <https://www.nativescientist.com/>)
- Martial arts practitioner.

References**Prof. Dr. Rer. Nat. Rüdiger Rudolf**

Interdisciplinary Center for Neuroscience, Heidelberg University
r.rudolf@hs-mannheim.de

Prof. Dr. Med. Norbert Gretz

Medical Research Center, Medical Faculty Mannheim, Heidelberg University
norbert.gretz@medma.uni-heidelberg.de

Prof. Dr. Rer. Nat. Mathias Hafner

Institute of Molecular and Cellular Biotechnology, Mannheim University of Applied Sciences
m.hafner@hs-mannheim.de

Abbreviations

| | |
|-------|--|
| ACh | Acetylcholine |
| AChR | Nicotinic acetylcholine receptor |
| ASCs | Adipose-derived mesenchymal stem cells |
| BGT | Bungarotoxin |
| BSA | Bovine serum albumin |
| ECM | Extracellular matrix |
| EDL | Extensor digitorum longus |
| FAP | Fibro-adipogenic progenitor |
| eMHC | Embryonic myosin heavy chain |
| EYFP | Endogenous yellow fluorescent protein |
| HE | Hematoxylin-eosin |
| IL-1 | Interleukin 1 |
| IL-6 | Interleukin 6 |
| Lrp4 | Low-density lipoprotein receptor-related protein 4 |
| mIgG | Mouse immunoglobulin type G |
| MMP | Metalloproteinase |
| MYO3 | Myosin 3 |
| MuSK | Muscle specific kinase |
| NMJ | Neuromuscular junction |
| PBS | Phosphate-buffered saline |
| PFA | Paraformaldehyde |
| VACHT | Vesicular acetylcholine transporter |
| TA | Tibialis anterior |

| | |
|---------------|-----------------------------|
| TDE | Thiodiethanol |
| TNF- α | Tumor necrosis factor alpha |
| TSCs | Terminal Schwann cells |